Physical Mechanisms of Control of Gliding in Flying Snakes

Farid Jafari

Dissertation submitted to the faculty of the
Virginia Polytechnic Institute and State University
in partial fulfillment of the requirements for the degree of

Doctor of Philosophy
in

Engineering Mechanics

John J. Socha, chair
Nicole Abaid
Shane D. Ross
Pavlos P. Vlachos
Craig A. Woolsey

August 12, 2016
Blacksburg, VA

Keywords: Flying snakes, glide, stability, control, and aerodynamics

Physical Mechanisms of Control of Gliding in Flying Snakes

Farid Jafari

ABSTRACT

Flying snakes possess a sophisticated gliding ability with a unique aerial behavior, in which they flatten their body to make a roughly triangular cross-sectional shape to produce lift and gain horizontal acceleration. Also, the snakes assume an S-like posture and start to undulate by sending traveling waves down the body. The present study aims to answer how the snakes are able to control their glide trajectory and remain stable without any specialized flight surfaces. Undulation is the most prominent behavior of flying snakes and is likely to influence their dynamics and stability. To examine the effects of undulation, a number of theoretical models were used. First, only the longitudinal dynamics were considered with simple two-dimensional models, in which the snake was approximated as a number of connected airfoils. Previously measured force coefficients were used to model aerodynamic forces, and undulation was considered as periodic changes in the mass and area of the airfoils. The model was shown to be passively unstable, but it could be stabilized with a restoring pitching moment. Next, a three-dimensional model was developed, with the snake modeled as a chain of airfoils connected through revolute joints, and undulation was considered as periodic changes in the joint angles. It was shown that undulation, when added to a linearization-based closed-loop control, could increase the size of the basin of stability. Our theoretical results suggested that the snakes need some extent of closed-loop control in spite of the clear contribution of undulation to the stability of glide. Next, we considered the effects of aerodynamic interactions between the fore and the aft body on the aerodynamic performance of flying snakes. Two-dimensional anatomically accurate airfoils were used in a water tunnel. Lift and drag forces were measured by load cells, and the flow field data were obtained using digital particle image velocimetry. The results confirmed strong dependence of the aerodynamic performance on the tandem arrangement. Flow fields around the airfoils were obtained to show how the tandem arrangement modified the separated flow and the wake; therefore altering the pressure field and resulting in changes in the lift and drag.

Physical Mechanisms of Control of Gliding in Flying Snakes

Farid Jafari

GENERAL AUDIENCE ABSTRACT

Flying snakes are a group of snake species that are found primarily in lowland tropical forests of south and southeast Asia. These snakes possess a sophisticated gliding ability, with an aerial behavior which is fundamentally different from any other biological or man-made flyer. As flying snakes lack conventional wings or any other specialized flight surfaces, they use their entire body as a morphing 'wing' to produce lift and gain forward acceleration. While airborne, the snakes assume an undulating S-like posture, in which traveling waves move down the body. The role of this highly dynamic aerial behavior in the gliding of snakes is not known. In this study, we hypothesized that body undulation is likely to influence the dynamics and stability of snakes, because it continually redistributes mass and aerodynamic forces along the body. To study the dynamics of snake flight, we developed a number of theoretical models, starting from simple two-dimensional models, and then proceeding to more realistic three-dimensional models. Undulation was considered as periodic changes in the shape of the model. The models were shown to be passively unstable, but they could be stabilized with some control. Under certain conditions, it was shown that undulation could stabilize the trajectory without any control. Overall, our theoretical results suggested that the snakes need some extent of control in spite of the clear contribution of undulation to the stability of glide. We also considered the effects of aerodynamic interactions between the fore and the aft body on the aerodynamic performance of flying snakes. With two anatomically accurate airfoils placed in a water tunnel, the forces were measured by load cells, and the flow around the airfoils were captured by high-speed cameras. The results confirmed that the aerodynamic forces on the tandem airfoils would change when the airfoils are moved with respect to each other. Overall, the results of this study elucidate the underlying physical principles used by flying snakes in their unconventional mode of aerial locomotion. Therefore, these results can help to engineering novel biologically inspired vehicles.

ACKNOWLEDGEMENTS

The experimental part of this study could never be accomplished without the unstinting help of my dear friends Dr. Sevak Tahmasian, Dr. Ayoub Yari, Dr. Mohammad Mostafavi, and Mr. Khaled Adjerid, to whom I will always be grateful. Also, I would like to thank Dr. Christopher Williams and other members of DREAMS lab at Virginia Tech who made the snake model with 3D printing.

I would like to thank my dissertation committee for their support and helpful advice. I am especially indebted to my advisor Dr. Jake Socha for his generous support and invaluable guidance. I learned much more than science from him and my respect for him is beyond words.

My greatest appreciation is due to my wife, who never stopped encouraging me during all of these years. Without her, this work would never be accomplished. I dedicate my dissertation to my wife and to my son who are my life's delights.

TABLE OF CONTENTS

LIST OF FIGURES

Chapter 1. Introduction

Chapter 2. A theoretical analysis of pitch stability during gliding in flying snakes

LIST OF TABLES

Chapter 2. A theoretical analysis of pitch stability during gliding in flying snakes

Chapter 4. Experimental study of the aerodynamics of snake-like airfoils in tandem configuration

Chapter 1. Introduction

1. Motivation

Gliding, defined as the ability to control an aerial descent, has evolved in many vertebrate and invertebrate animals (Dudley et al., 2007). Almost every gliding taxon has solved the physical problem of how to generate sufficient aerodynamic forces in the same way: they use symmetrically paired wings projected from the body and held in a generally static posture (Biewener, 2003, Alexander, 2003). Bilateral symmetry is present also in the design of engineered flyers ranging from micro-air vehicles to airplanes to multi-rotor helicopters (Hoffmann et al., 2007, Lupashin et al., 2010). This design, through asymmetric deployment of aerodynamic surfaces about different body axes (Dudley, 2002), provides the ability to alter flight speed, trajectory, and body orientation, which is required to meet performance objectives such as efficiency and control for straight flight, maneuvering, and landing. For most animal gliders, flight control is augmented by the ability to selectively apply forces to counteract rotations, usually by altering wing characteristics (such as camber) or by shifting the position of appendages.

However, the Asian arboreal snakes of the genus *Chrysopelea* have found a much less expected solution for aerial locomotion (Socha, 2002). With a cylindrical body, the snakes lack conventional wings and appendages and have no specialized anatomy to produce flight forces used to oppose the gravity and to control the trajectory. Despite a design that would appear disadvantageous for flight, the flying snakes possess a sophisticated ability to glide: they jump from trees, flatten the body and undulate in the air in a complex 3D pattern. The glide performance of the snakes is comparable to that of other gliders (Scholey, 1986, Socha and LaBarbera, 2005, McGuire, 1998). The snakes are able to cover significant horizontal distance with a shallow glide angle (as little as 13° from the horizon) toward the end of the glide. One of the species, *C. paradisi*, is even capable of active maneuvers (Socha, 2002, Socha and LaBarbera, 2005, Socha et al., 2010). In contrast, some non-flying snakes are known to tumble when dropped from a height (Heyer and Pongsapipatana, 1970), and no other species can glide, demonstrating that the physical or physiological mechanisms of control used by *Chrysopelea* are not present in all snakes.

The flying snakes do not appear anatomically exceptional or unique, but their flight is fundamentally different from any other biological or man-made flyer. Upon becoming airborne, the snake first splays its ribs to the side, flattening out in the dorsoventral axis and creating a 'wing' with an unconventional cross-sectional shape. The snakes glide by using this morphing wing that continuously reconfigures throughout flight, which is accomplished by sending high-amplitude traveling waves posteriorly down the body, producing an aerial undulation. This combination of body morphing and undulation produces a glider with symmetries drastically different from all other biological or engineered flyers. In particular, (i) undulatory motion entails significant out-of-plane translation of different parts of the body, a feature not observed in other gliders, and (ii) because of undulation, the snake's body posture is bilaterally asymmetric at any moment in time, yet its rib splaying creates an airfoil with fore–aft symmetry.

In summary, flying snakes exhibit a combination of peculiar behaviors that are counterintuitive to our conventional understanding of flight. Despite our growing knowledge about the kinematics and aerodynamics of flying snakes, it remains a mystery how they produce stable forward gliding or how it is capable of active maneuvering in the absence of obvious control surfaces. An important step toward solving this problem is to understand the snake's stability characteristics in the pitch, roll and yaw directions. This project aims to use originally developed theoretical and experimental models to provide the first detailed physical investigation of how the snake produces controlled stable gliding. More precisely, we attempt to answer the question: how do postural reconfigurations of an undulating glider affect its aerial performance, and to what extent is this accomplished through active or passive control mechanisms? This work could serve as a basis for future studies that explore the evolutionary and ecological origins of snake gliding flight. Moreover, understanding the aerodynamics and mechanics of flying snakes will allow exploiting the underlying principles in order to engineer novel bio-inspired aerial vehicles.

2. Background

Flying snakes are a group of five species of colubrid snakes found primarily in lowland tropical forests of south and southeast Asia. In body size, they are not particularly large, with a length on the order of one meter and body mass from a few to a few hundred grams. The three species that

have been examined thus far (*Chrysopelea ornata*, *C. paradisi* and *C. pelias*) display a range of aerial performances, with *C. paradisi* being the superior glider (Socha and LaBarbera, 2005).

Although only the basic kinematic features of glide trajectories of flying snakes are examined in a few recent studies, they are among the small group of animals certain aspects of whose gliding behavior have been precisely quantified (flying squirrels (Bahlman et al., 2013, Bishop, 2006), flying lizards (McGuire and Dudley, 2005), colugos (Byrnes et al., 2011), and flying snakes (Socha and LaBarbera, 2005, Socha et al., 2005, Socha et al., 2010)). The performance of other gliders has been characterized largely based on takeoff and landing locations (Jackson, 2000, Vernes, 2001, Young et al., 2002, Scholey, 1986, Scheibe and Robins, 1998, Ando and Shiraishi, 1993, Heyer and Pongsapipatana, 1970). The studies on snakes have documented that they jump from trees using the takeoff sequence as shown in Fig. 1. The snake drops its fore body from a horizontal substrate such as a branch and assumes a J-shaped loop with the head facing forward. While the back of the body is gripping the branch, the snake accelerates its fore-body upward and away from the branch, which will be released when the snake reaches the apex of its jump.

Concurrently, the snake dorsoventrally reconfigures its whole body shape, doubling the width with the cross-section being flattened on the bottom and triangular on the top. After take-off, the snake passes through a ballistic dive phase, in which the glide angle (the angle of the glide path relative to horizontal) is steep (~50°-70°, depending on species) and on the order of 2 m of height is lost. This is followed by a shallowing glide phase in which the glide angle decreases due to lift generation and the glide behavior of the snake develops fully. By the start of this phase, the snake has started to undulate laterally in an S-like shape, sending traveling waves posteriorly down the body. During the shallowing phase, the snake maintains a staggered configuration, with the anterior body oriented roughly level to the ground traveling at a speed of 8-11 m/s (Fig. 2). Finally, the snake lands on the ground or vegetation without injury (Socha, 2002, Socha et al., 2005, Socha and LaBarbera, 2005, Socha, 2006, Socha, 2011, Socha et al., 2010).

Any flyer's abilities essentially depend on its aerodynamic performance. The aerodynamic basis of flight in birds, bats and insects has been extensively studied, and the steady and unsteady effects, 2D and 3D dynamics, wake patterns and fluid–structure interactions have been largely revealed (Lehmann, 2004, Wang, 2005, Tobalske, 2007, Hedenström and Spedding,

2008, Song et al., 2008, Usherwood and Lehmann, 2008, Lehmann, 2009, Johansson et al., 2010). In comparison, the aerodynamics of animals that can only glide has received far less attention (Emerson and Koehl, 1990, McCay, 2001, Bishop, 2007, Alexander et al., 2010, Park and Choi, 2010, Bahlman et al., 2013) despite the relative simplicity of 'static' gliders wings and their large morphological and taxonomic diversity (Dudley et al., 2007, Dudley and Yanoviak, 2011). Anyway, steady state aerodynamic behavior of a 2D airfoil with the snake's body cross-sectional shape has been examined in some recent experimental and computational modeling studies (Miklasz et al., 2010, Krishnan et al., 2014, Holden et al., 2014). It has been shown that the snake-like airfoil can maintain high lift at angles of attack as large as 35°, with lift coefficients reaching as high as 1.9. Moreover, high lift and lift-to-drag ratios can be maintained over a large range of angles of attack, helping to explain how the snake begins to generate significant lift even during the steep ballistic dive portion of the trajectory (Fig. 3).

Because of the staggered S-shaped configuration of the gliding snake, aerodynamic interactions between the fore and aft body are likely to take place. Specifically, the vortices formed upstream are intercepted by the downstream cross-sections. It has been shown that such interactions, which have been previously observed in flapping wings (Akhtar et al., 2007, Lehmann, 2008, Wang and Russell, 2007, Maybury and Lehmann, 2004, Warkentin and DeLaurier, 2007, Weimerskirch et al., 2001), often result in reduced energy cost (Weimerskirch et al., 2001, Lehmann, 2009, Rival et al., 2011a) (but see (Usherwood et al., 2011)), while they possibly cause a reduction in overall lift (Usherwood and Lehmann, 2008, Rival et al., 2011b). There exist a few studies (Scharpf and Mueller, 1992, Michelsen and Mueller, 1987, Husain et al., 2005) on the static tandem airfoils in flows with moderate Reynolds numbers ($Re = 8.5\times10^4 - 2.25\times10^5$), but only a simplified preliminary study (Miklasz et al., 2010) used snake-like airfoils and $Re = 15000$. It was suggested that the tandem arrangement of two airfoils could cause significant changes in the lift and drag coefficients of the downstream airfoil relative to a solitary airfoil at the same angle of attack (Fig. 4). Also, Holden (unpublished data) examined geometrically accurate airfoils placed in tandem at several combinations of gap, stagger, and angle of attack. The results, summarized in Fig. 5, show the normalized change in the combined lift-to-drag ratio of the tandem model with respect to two single models having the same angles of attack.

3. The present work

Among a diversity of flying snake's arboreal behaviors that may potentially be employed in the snake's control system, undulation and staggered configuration are the most important. Undulation manifests itself in the snake's flight dynamics by continually redistributing body mass and aerodynamic forces, and the staggered configuration enables the snake to exploit the upstream-downstream aerodynamic interactions toward controlling its trajectory. To address the question of how these traits are integrated in the snake's control system, this work takes three general approaches, which are briefly introduced below. Each of the next chapters reports these approaches in detail.

Objective 1: Determining the role of undulation in pitch stability during straight glide.

Undulation is arguably the most prominent arboreal behavior of flying snakes. Because of undulation, body mass and aerodynamic forces are continually redistributed which means that the center of mass (CoM) and the center of pressure (CoP) move with respect to each other. Since the relative position of CoM and CoP plays the most important role in the rotational dynamics and stability characteristics of an object moving through a fluid, it is anticipated that undulation profoundly influences the snake's glide trajectory. This speculation is also supported by the results of (Socha and LaBarbera, 2005) stating that relative undulation amplitude is correlated with the snake's airspeed and acceleration. Therefore, any attempt to understand the control system of flying snakes should start with determining the effects of undulation on the dynamics of glide. The first objective encompasses the initiative step toward this goal by considering the motion of snake in 2D and focusing on stability in the pitch direction. In particular, the hypothesis that undulation contributes to pitch stability is examined. 2D theoretical models are used to approximate the dynamics of flying snakes.

Objective 2: Developing a dynamical framework for the motion of snake in 3D and determining its basic stability characteristics.

In spite of the substantial information that simplified 2D analysis of flying snakes provides about

the fundamentals of their control system, in order to fully understand the locomotion and design of snakes, it is crucial to provide an analytical and computational framework, which encapsulates their entire 3D motions. This becomes more important by recalling that the snake has only an elongate body and its postural motions to produce flight forces and maintain stability, and the kinematics that produce the required forces can be revealed only by a 3D model capable of duplicating snake's postural reconfigurations. Furthermore, this dynamical framework, allows us to explore theoretically possible but biologically unrealized motions, and to exploit the underlying principles to engineer biologically inspired robotic analogues to snakes.

An intuitive way to model the snakes is using a chain of n rigid links connected by revolute or spherical joints (n-chain) to obtain an articulated snake-like system. This model has been widely used to study and reproduce the terrestrial motion of snakes (see e.g. Hirose and Morishima, 1990, Prautsch and Mita, 1999, Maladen et al., 2011, Dowling, 1999, Saito et al., 2002, Mori and Hirose, 2002, Chernousko, 2005, Enner et al., 2012). Here, we use this model for the first time to consider the motion of snakes through air. The principles of snake flight can be uncovered by understanding how the n-chain is reoriented by changes in its shape. In other words, we are interested in the coupling between the shape dynamics and the overall rotation and translation of the n-chain. We hypothesize that undulation, which is a cyclic motion in the shape space of the n-chain, is required for the flight stability. In relation to this hypothesis, we determine the minimum number of links required for stable flight.

Objective 3: Determining how the staggered configuration modifies the aerodynamic performance of flying snakes.

Flying snakes assume an S-shape and undergo a sequence of undulatory motions while airborne. These motions also include a cyclic vertical translation of the aft body. Consequently, a complex interaction between the fore and the aft body takes place where vortices formed upstream are intercepted by the downstream cross-sections. In a simplified approach, this interaction can be approximated by a two-dimensional staggered airfoil configuration, as shown in Fig. 4A. By varying the gap and stagger spacing between the two airfoils as well as the angles of attack, it is possible to reproduce a wide range of conditions representative of the snake's flight configurations. Holden et al. who used anatomically accurate physical models to characterize the

aerodynamic performance of a single snake-like 2D airfoil (Holden et al., 2014), also measured lift and drag forces on two such airfoils placed in tandem at a few combinations of gap, stagger, and angles of attack. The yet unpublished results confirmed strong dependence of the lift and drag forces on the arrangement (Fig. 5), which provides the possibility for the snake to exploit these aerodynamic interactions to control the glide trajectory.

Consistent with the goal of this project to study the physical mechanisms of control in flying snakes, we try to determine the effects of tandem arrangement on the overall aerodynamic performance. The portions of the parameter space, including the arrangements that are close to snake kinematics, have to be explored. We hypothesize that the underlying vortex-blade interaction is responsible for the vortex-induced lift augmentation and drag reduction. Particle Image velocimetry (PIV) is used to visualize the flow around the airfoils and verify the hypothesis. More broadly, this study determines the physical limits on the aerodynamics of the tandem snake airfoils.

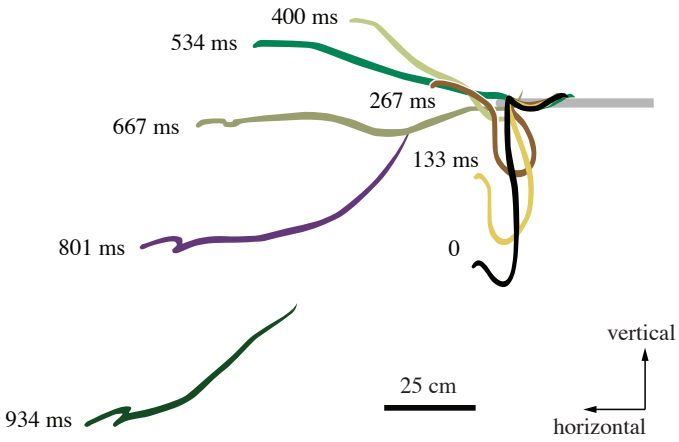

Fig. 1: Side view of takeoff in *C. paradisi*, adapted from (Socha, 2006).

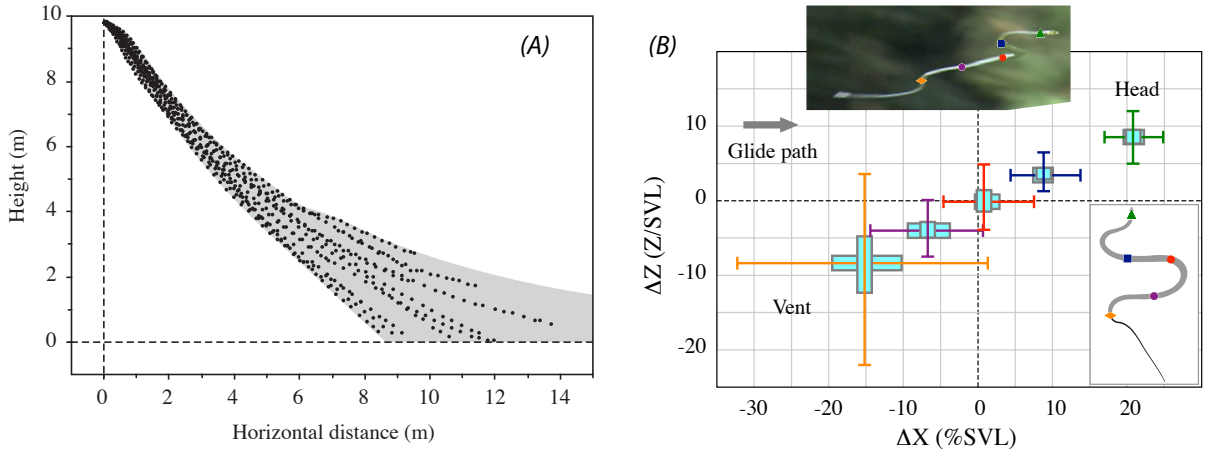

Fig. 2: Trajectory kinematics of *C. paradisi*. (A) Compilation of 14 glide trajectories, adapted from (Socha et al., 2005). (B) Summary of the body posture normalized by the snout-vent length, adapted from (Socha et al., 2010).

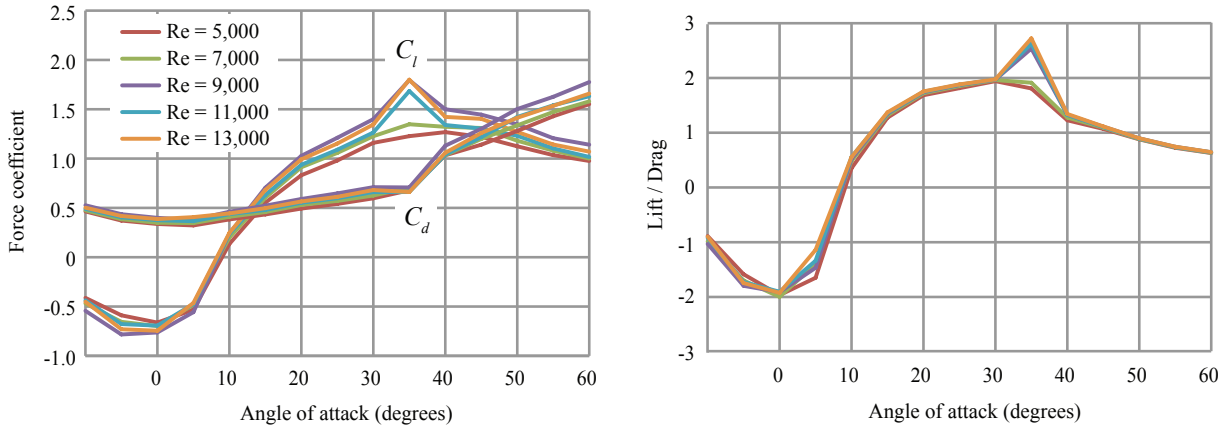

Fig. 3: Steady-state lift and drag coefficients and the lift-to-drag ratio measured for a straight airfoil having the same cross-sectional shape as the flattened snake, adapted from (Holden et al., 2014).

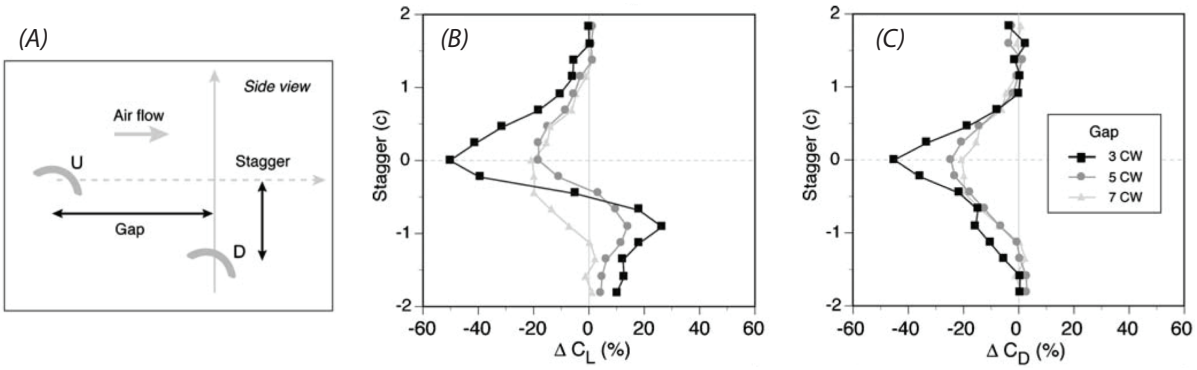

Fig. 4: (A) Two airfoils having the same angle of attack of α=25° are arranged in the staggered configuration. 'U' and 'D' indicate upstream and downstream, respectively. The aerodynamic interactions between the airfoils result in significant changes in the (B) lift and (C) drag coefficients of the downstream airfoil, relative to a single airfoil at the same angle of attack. The figures are adapted from (Miklasz et al., 2010).

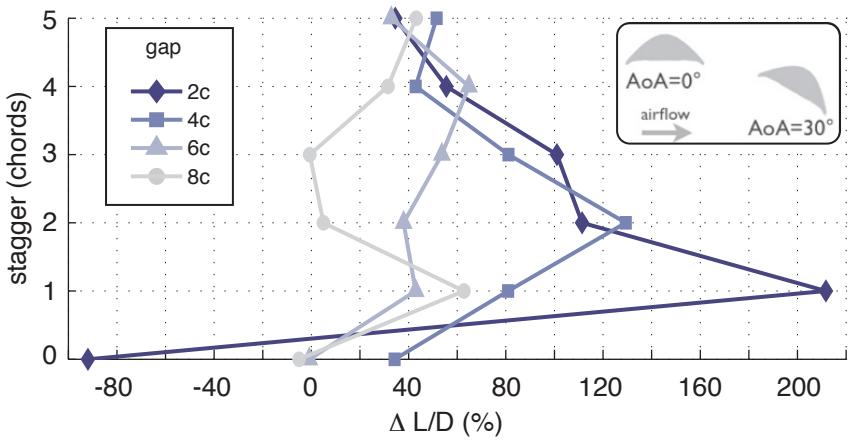

Fig. 5: For the depicted combination of angles of attack, striking changes in the lift-to-drag ratio could be achieved by choicely changing the gap and stagger as small as one chord length (Holden, unpublished data).

References

AKHTAR, I., MITTAL, R., LAUDER, G. V. & DRUCKER, E. 2007. Hydrodynamics of a biologically inspired tandem flapping foil configuration. *Theoretical and Computational Fluid Dynamics,* 21**,** 155-170.

ALEXANDER, D. E., GONG, E., MARTIN, L. D., BURNHAM, D. A. & FALK, A. R. 2010. Model tests of gliding with different hindwing configurations in the four-winged dromaeosaurid Microraptor gui. *Proceedings of the National Academy of Sciences,* 107**,** 2972-2976.

ALEXANDER, R. M. 2003. *Principles of animal locomotion*, Princeton University Press.

ANDO, M. & SHIRAISHI, S. 1993. Gliding flight in the Japanese giant flying squirrel *Petaurista leucogenys*. *Journal of the Mammalogical Society of Japan,* 18**,** 19-32.

BAHLMAN, J. W., SWARTZ, S. M., RISKIN, D. K. & BREUER, K. S. 2013. Glide performance and aerodynamics of non-equilibrium glides in northern flying squirrels (*Glaucomys sabrinus*). *Journal of The Royal Society Interface,* 10**,** 20120794.

BIEWENER, A. A. 2003. *Animal locomotion*, Oxford University Press.

BISHOP, K. L. 2006. The relationship between 3-D kinematics and gliding performance in the southern flying squirrel, *Glaucomys volans*. *Journal of Experimental Biology,* 209**,** 689-701.

BISHOP, K. L. 2007. Aerodynamic force generation, performance and control of body orientation during gliding in sugar gliders (*Petaurus breviceps*). *Journal of Experimental Biology,* 210**,** 2593-2606.

BYRNES, G., LIBBY, T., LIM, N. T.-L. & SPENCE, A. J. 2011. Gliding saves time but not energy in Malayan colugos. *Journal of Experimental Biology,* 214**,** 2690-2696.

CHERNOUSKO, F. L. 2005. Modelling of snake-like locomotion. *Applied Mathematics and Computation,* 164**,** 415-434.

DOWLING, K. Limbless locomotion: learning to crawl. Robotics and Automation, 1999. Proceedings. 1999 IEEE International Conference on, 1999. IEEE, 3001-3006.

DUDLEY, R. 2002. Mechanisms and implications of animal flight maneuverability. *Integrative and Comparative Biology,* 42**,** 135-140.

DUDLEY, R., BYRNES, G., YANOVIAK, S. P., BORRELL, B., BROWN, R. M. & MCGUIRE, J. A. 2007. Gliding and the functional origins of flight: biomechanical novelty or necessity? *Annual Review of Ecology, Evolution, and Systematics***,** 179-201.

DUDLEY, R. & YANOVIAK, S. P. 2011. Animal aloft: the origins of aerial behavior and flight. *Integrative and Comparative Biology,* 51**,** 926-936.

EMERSON, S. B. & KOEHL, M. 1990. The interaction of behavioral and morphological change in the evolution of a novel locomotor type:" flying" frogs. *Evolution***,** 1931-1946.

ENNER, F., ROLLINSON, D. & CHOSET, H. Simplified motion modeling for snake robots. Robotics and Automation (ICRA), 2012 IEEE International Conference on, 2012. IEEE, 4216-4221.

HEDENSTRÖM, A. & SPEDDING, G. 2008. Beyond robins: aerodynamic analyses of animal flight. *Journal of The Royal Society Interface,* 5**,** 595-601.

HEYER, W. R. & PONGSAPIPATANA, S. 1970. Gliding speeds of *Ptychozoon lionatum* (Reptilia: Gekkonidae) and *Chrysopelea ornata* (Reptilia: Colubridae). *Herpetologica***,** 317-319.

HIROSE, S. & MORISHIMA, A. 1990. Design and control of a mobile robot with an articulated body. *The International Journal of Robotics Research,* 9**,** 99-114.

HOFFMANN, G. M., HUANG, H., WASLANDER, S. L. & TOMLIN, C. J. Quadrotor helicopter flight dynamics and control: Theory and experiment. Proc. of the AIAA Guidance, Navigation, and Control Conference, 2007.

HOLDEN, D., SOCHA, J. J., CARDWELL, N. D. & VLACHOS, P. P. 2014. Aerodynamics of the flying snake *Chrysopelea paradisi*: how a bluff body cross-sectional shape contributes to gliding performance. *Journal of Experimental Biology,* 217**,** 382-394.

HUSAIN, Z., ABDULLAH, M. & YAP, T. 2005. Two-dimensional analysis of tandem/staggered airfoils using computational fluid dynamics. *International Journal of Mechanical Engineering Education,* 33**,** 195-207.

JACKSON, S. M. 2000. Glide angle in the genus *Petaurus* and a review of gliding in mammals. *Mammal Review,* 30**,** 9-30.

JOHANSSON, L. C., WOLF, M. & HEDENSTRÖM, A. 2010. A quantitative comparison of bird and bat wakes. *Journal of The Royal Society Interface,* 7**,** 61-66.

KRISHNAN, A., SOCHA, J. J., VLACHOS, P. P. & BARBA, L. 2014. Lift and wakes of flying snakes. *Physics of Fluids (1994-present),* 26**,** 031901.

LEHMANN, F.-O. 2004. The mechanisms of lift enhancement in insect flight. *Naturwissenschaften,* 91**,** 101-122.

LEHMANN, F.-O. 2008. When wings touch wakes: understanding locomotor force control by wake–wing interference in insect wings. *Journal of Experimental Biology,* 211**,** 224-233.

LEHMANN, F.-O. 2009. Wing–wake interaction reduces power consumption in insect tandem wings. *Experiments in Fluids,* 46**,** 765-775.

LUPASHIN, S., SCHOLLIG, A., SHERBACK, M. & D'ANDREA, R. A simple learning strategy for high-speed quadrocopter multi-flips. Robotics and Automation (ICRA), 2010 IEEE International Conference on, 2010. IEEE, 1642-1648.

MALADEN, R. D., DING, Y., UMBANHOWAR, P. B. & GOLDMAN, D. I. 2011. Undulatory swimming in sand: experimental and simulation studies of a robotic sandfish. *The International Journal of Robotics Research,* 30**,** 793-805.

MAYBURY, W. J. & LEHMANN, F.-O. 2004. The fluid dynamics of flight control by kinematic phase lag variation between two robotic insect wings. *Journal of Experimental Biology,* 207**,** 4707-4726.

MCCAY, M. G. 2001. Aerodynamic stability and maneuverability of the gliding frog *Polypedates dennysi*. *Journal of Experimental Biology,* 204**,** 2817-2826.

MCGUIRE, J. A. 1998. Phylogenetic systematics, scaling relationships, and the evolution of gliding performance in flying lizards (genus *Draco*).

MCGUIRE, J. A. & DUDLEY, R. 2005. The cost of living large: comparative gliding performance in flying lizards (Agamidae: *Draco*). *The American Naturalist,* 166**,** 93-106.

MICHELSEN, W. & MUELLER, T. Low Reynolds number airfoil performance subjected to wake interference from an upstream airfoil. AIAA Conference Paper, 1987. 87-2351.

MIKLASZ, K., LABARBERA, M., CHEN, X. & SOCHA, J. 2010. Effects of body cross-sectional shape on flying snake aerodynamics. *Experimental Mechanics,* 50**,** 1335-1348.

MORI, M. & HIROSE, S. Three-dimensional serpentine motion and lateral rolling by active cord mechanism ACM-R3. Intelligent Robots and Systems, 2002. IEEE/RSJ International Conference on, 2002. IEEE, 829-834.

PARK, H. & CHOI, H. 2010. Aerodynamic characteristics of flying fish in gliding flight. *Journal of Experimental Biology,* 213**,** 3269-3279.

PRAUTSCH, P. & MITA, T. Control and analysis of the gait of snake robots. Control Applications, 1999. Proceedings of the 1999 IEEE International Conference on, 1999. IEEE, 502-507.

RIVAL, D., HASS, G. & TROPEA, C. 2011a. Recovery of energy from leading-and trailing-edge vortices in tandem-airfoil configurations. *Journal of Aircraft,* 48**,** 203-211.

RIVAL, D., SCHÖNWEITZ, D. & TROPEA, C. 2011b. Vortex interaction of tandem pitching and plunging plates: a two-dimensional model of hovering dragonfly-like flight. *Bioinspiration & Biomimetics,* 6**,** 016008.

SAITO, M., FUKAYA, M. & IWASAKI, T. 2002. Modeling, analysis, and synthesis of serpentine locomotion with a multilink robotic snake. *IEEE Control Systems Magazine,* 22**,** 64-81.

SCHARPF, D. F. & MUELLER, T. J. 1992. Experimental study of a low Reynolds number tandem airfoil configuration. *Journal of Aircraft,* 29**,** 231-236.

SCHEIBE, J. S. & ROBINS, J. H. 1998. Morphological and performance attributes of gliding mammals. *Ecology and evolutionary biology of tree squirrels,* 6**,** 131-144.

SCHOLEY, K. 1986. The climbing and gliding locomotion of the giant red flying squirrel *Petaurista petaurista* (Sciuridae). *Biona Report,* 5**,** 187-204.

SOCHA, J. J. 2002. Kinematics: Gliding flight in the paradise tree snake. *Nature,* 418**,** 603-604.

SOCHA, J. J. 2006. Becoming airborne without legs: the kinematics of take-off in a flying snake, *Chrysopelea paradisi*. *Journal of Experimental Biology,* 209**,** 3358-3369.

SOCHA, J. J. 2011. Gliding flight in Chrysopelea: turning a snake into a wing. *Integrative and Comparative Biology,* 51**,** 969-982.

SOCHA, J. J. & LABARBERA, M. 2005. Effects of size and behavior on aerial performance of two species of flying snakes (*Chrysopelea*). *Journal of Experimental Biology,* 208**,** 1835-1847.

SOCHA, J. J., MIKLASZ, K., JAFARI, F. & VLACHOS, P. P. 2010. Non-equilibrium trajectory dynamics and the kinematics of gliding in a flying snake. *Bioinspiration & Biomimetics,* 5**,** 045002.

SOCHA, J. J., O'DEMPSEY, T. & LABARBERA, M. 2005. A 3-D kinematic analysis of gliding in a flying snake, *Chrysopelea paradisi*. *Journal of Experimental Biology,* 208**,** 1817-1833.

SONG, A., TIAN, X., ISRAELI, E., GALVAO, R., BISHOP, K., SWARTZ, S. & BREUER, K. 2008. Aeromechanics of membrane wings with implications for animal flight. *AIAA journal,* 46**,** 2096-2106.

TOBALSKE, B. W. 2007. Biomechanics of bird flight. *Journal of Experimental Biology,* 210**,** 3135-3146.

USHERWOOD, J. R. & LEHMANN, F.-O. 2008. Phasing of dragonfly wings can improve aerodynamic efficiency by removing swirl. *Journal of The Royal Society Interface,* 5**,** 1303-1307.

USHERWOOD, J. R., STAVROU, M., LOWE, J. C., ROSKILLY, K. & WILSON, A. M. 2011. Flying in a flock comes at a cost in pigeons. *Nature,* 474**,** 494-497.

VERNES, K. 2001. Gliding performance of the northern flying squirrel (*Glaucomys sabrinus*) in mature mixed forest of eastern Canada. *Journal of Mammalogy,* 82**,** 1026-1033.

WANG, Z. J. 2005. Dissecting insect flight. *Annual Review of Fluid Mechanics,* 37**,** 183-210.

WANG, Z. J. & RUSSELL, D. 2007. Effect of forewing and hindwing interactions on aerodynamic forces and power in hovering dragonfly flight. *Physical Review Letters,* 99**,** 148101.

WARKENTIN, J. & DELAURIER, J. 2007. Experimental aerodynamic study of tandem flapping membrane wings. *Journal of Aircraft,* 44**,** 1653-1661.

WEIMERSKIRCH, H., MARTIN, J., CLERQUIN, Y., ALEXANDRE, P. & JIRASKOVA, S. 2001. Energy saving in flight formation. *Nature,* 413**,** 697-698.

YOUNG, B. A., LEE, C. E. & DALEY, K. M. 2002. On a flap and a foot: aerial locomotion in the "flying" gecko, *Ptychozoon kuhli*. *Journal of Herpetology,* 36**,** 412-418.

Chapter 2. A theoretical analysis of pitch stability during gliding in flying snakes

Abstract

Flying snakes use their entire body as a continuously morphing 'wing' to produce lift and shallow their glide trajectory. Their dominant behavior during gliding is aerial undulation, in which lateral waves are sent posteriorly down the body. This highly dynamic behavior, which is unique among animal gliders, should have substantial effects on the flight dynamics and stability of the snakes, resulting from the continuous redistribution of mass and aerodynamic forces. In this study, we develop two-dimensional theoretical models to assess the stability characteristics of snakes in the pitch direction. Previously measured force coefficients are used to simulate aerodynamic forces acting on the models, and undulation is simulated by varying mass. Model 1 is a simple three-airfoil representation of the snake's body that possesses a passively stable equilibrium solution, whose basin of stability contains initial conditions observed in experimental gliding trajectories. Model 2 is more sophisticated, with more degrees of freedom allowing for postural changes to better represent the snake's real kinematics; in addition, a restoring moment is added to simulate potential active control. The application of static and dynamic stability criteria show that Model 2 is passively unstable, but can be stabilized with the restoring moment. Overall, these models suggest that undulation does not contribute to stability in pitch, and that flying snakes require a closed-loop control system formed around a passively stable dynamical framework.

1. Introduction

All flyers require the ability to alter flight speed, trajectory, and body orientation to meet performance objectives such as efficiency and control for straight flight, maneuvering, and landing. Flight control is usually accomplished through asymmetric deployment of aerodynamic surfaces about different body axes (Dudley, 2002). From aircraft to animals that have evolved the ability to fly, the use of symmetrically paired wings is an almost universal feature. Elevators, wing flaps, spoilers and a horizontal tail are used in aircraft as control devices, but flying and

gliding animals must use their wings, tail, and other morphological features both to generate aerodynamic forces and to control the trajectory (Alexander, 2003, Biewener, 2003).

For most animal gliders, flight control is augmented by the ability to selectively apply forces to counteract rotations, usually by altering wing characteristics (such as camber) or by shifting the position of appendages. However, flying snakes of the genus *Chrysopelea* lack conventional wings and appendages, and possess no specialized anatomy for control. Despite a design that would appear disadvantageous for flight, the glide performance of flying snakes is comparable to that of other gliders (Scholey, 1986, McGuire, 1998, Socha et al., 2005), with one species that is even capable of aerial maneuvers (Socha, 2002, Socha et al., 2005, Socha et al., 2010). In contrast, some non-flying snakes are known to tumble when dropped from a height (Heyer and Pongsapipatana, 1970), and no other species can glide, demonstrating that the physical or physiological mechanisms of control used by *Chrysopelea* are not present in all snakes. However, the specific mechanisms that enable *Chrysopelea* snakes to remain stable while gliding, or to turn on command, are unknown.

Recent studies have helped to elucidate the basic kinematic features of glide trajectories of flying snakes (Socha, 2002, Socha et al., 2005, Socha and LaBarbera, 2005, Socha et al., 2010, Socha, 2011). After a jumping take-off, the snake passes through a ballistic dive phase, in which the glide angle (the angle of the glide path relative to horizontal) is steep (~50-70°, depending on species) and on the order of 2 m of height is lost. This is followed by a shallowing glide phase in which the glide angle decreases due to lift generation and the glide behavior of the snake develops fully. By the start of this phase, the snake has dorsoventrally flattened its whole body and undulates laterally in an S-like shape, sending traveling waves posteriorly down the body (Fig. 1D). During the shallowing phase, the snake maintains a staggered configuration, with the anterior body oriented roughly level to the ground and the overall body angled upward in the range of 25° from the glide path (Fig. 1C). Recent experimental and computational modeling studies show that the snake's body cross-sectional shape can maintain high lift at angles of attack as large as 35°, with lift coefficients reaching as high as 1.9 (Fig. 1E) (Miklasz et al., 2010, Holden et al., 2014, Krishnan et al., 2014). Moreover, high lift and lift-to-drag ratios can be maintained over a large range of angles of attack (Fig. 1F), helping to explain how the snake begins to generate significant aerodynamic forces even during the steep ballistic dive portion of the trajectory.

Despite our growing understanding of the kinematics and aerodynamics of flying snakes, their ability to maintain flight control remains a mystery. How does an undulating glider produce stable gliding in the absence of obvious control surfaces? An important step toward solving this problem is to understand the snake's stability characteristics in the pitch, roll and yaw directions. The simplest hypothesis is that a flying snake is passively stable in all directions; at the other extreme, the snake requires active control to counteract rotations about all axes.

Here, we develop new theoretical models as tools to address the stability characteristics of flying snakes for the first time. As a first-order study of a highly complex system, we chose to simplify the problem by considering the snake as a series of 2D airfoils, and focus only on stability in the pitch direction. We conducted simulations of glide trajectories using the aerodynamic characteristics of the snake's cross-sectional shape, with undulation simulated by periodically varying the mass and area of the airfoils. The models were examined for pitch stability by obtaining the eigenvalues of the linearized system about the steady-state solutions.

Overall, we aim to understand the fundamental control mechanisms that snakes employ during a glide, contributing to our broader goal of discovering the minimum set of parameters necessary to reproduce the glide performance of flying snakes. Such work will lend insight into the morphological and behavioral requirements to evolve gliding in snakes, and can also contribute to design principles for future flying snake-inspired air or water vehicles. For example, this work could serve as the basis for a staggered-wing micro-air vehicle that operates in the same Reynolds number regime as the real snake. This vehicle would draw inspiration from the undulating movement of the snake's body, allowing the staggered foils to change their relative spacing in order to achieve a desired aerodynamic performance.

2. Methods

Several approaches have been used to assess flight stability of animal flyers. One of the most common methods is to examine the static stability criterion (Etkin, 2012, McCormick, 1995). When a system experiences a small perturbation from equilibrium, this criterion determines if the acting forces would restore the system back to the equilibrium state. In recent years, the static stability criterion has been used to analyze animal flyers, including the testing of physical models in wind tunnels to understand flying frogs (McCay, 2001) and theoretical analyses of how the pitching moment about the center of mass (CoM) changes with angle of

attack in birds (Thomas and Taylor, 2001). Other studies have examined dynamic stability using kinematics of the moving animal, as has been used to assess insects (Taylor and Thomas, 2003) and flying squirrels (Bishop, 2006). Computational or robotic models have been used to analyze the passive dynamic stability of hovering fruit flies (Gao et al., 2011) and hawkmoths (Cheng et al., 2011).

Most such studies involve the simplifying assumption of bilateral symmetry (but see (Gao et al., 2011)), which allows the motions in the longitudinal direction to be decoupled from those in the lateral direction. This enables pitch stability to be considered as a simple one-dimensional problem. McCay (2001) and Thomas and Taylor (2001) additionally considered equilibrium gliding and determined whether disturbances from equilibrium would be passively counteracted.

However, neither of these assumptions can be employed to simplify the problem of gliding in snakes. First, the S-like posture of the snake endows it with a complete lack of bilateral symmetry, which means that the longitudinal and lateral dynamics cannot be decoupled. Second, due to the snake's dynamic undulating motion, whose effect acts like a periodic inertial force, it is unlikely that flying snakes glide in equilibrium. In fact, most recorded glide trajectories consist of transient motion, and equilibrium gliding has rarely been observed (Socha, 2002, Socha et al., 2005, Socha and LaBarbera, 2005, Socha et al., 2010). The undulatory motion must periodically change the locations of the center of pressure (CoP) and center of mass (CoM) via redistribution of area and mass, which leads to the hypothesis that the stability characteristics of the snakes are influenced by undulation. Overall, these characteristics suggest that understanding how flying snakes glide requires analyses of both static and dynamic stability.

In this study, we examined the dynamics and stability of gliding flight in snakes by developing two theoretical models, beginning with a simple model and progressing to a more complex and realistic model. As a first-order modeling approach, we ignored the effects of coupling between the longitudinal and lateral dynamics. This can also be viewed as a specific case of a straight glide with negligible roll, for which the longitudinal dynamics are independent from lateral motions.

How justifiable is this approach given real snake glide dynamics? The existing kinematic data are insufficient to appraise the decoupling of longitudinal and laterally dynamics, but lateral motions are indeed negligible under certain conditions. For a straight glide, sideslip and yaw are negligible, and if we also assume that roll is not pronounced, the coupling effects are further

diminished. According to Fig. 1A, which shows the rotation angles of the body relative to an inertial frame estimated from experimental data (Socha et al., 2010) for approximately two undulation periods, the assumption of small roll motion is reasonable, at least during late-phase gliding in *C. paradisi*. The angles in Fig. 1A are defined as the consecutive rotation angles that transform the inertial frame into the principal axes of inertia of the snake body as a whole; these were calculated from the moments of inertia in the x-y-z coordinates, which were estimated by assuming that the snake consisted of four line segments of equal masses determined by the 3D coordinates of five landmarks (Fig. 1C). Fig. 1A shows that for the majority of the time, deviations in roll are less than 10°. Small roll angle could also be inferred from Fig. 1B, where the relative displacements of different landmarks on the body are shown in the vertical and lateral directions.

2.1. Modeling of forces

We considered gravity and the aerodynamic forces of lift and drag in our two models. To calculate aerodynamic forces, we used lift and drag coefficients (C_l and C_d, respectively) from an experimental study of the 2D cross-sectional shape of C. paradisi, which assumed steady-state lift and drag (Holden et al., 2014). These coefficients (Figs. 1E, 1F) represent values over a range of Reynolds numbers that have been reported for C. paradisi (Socha et al., 2005). Based on an average glide speed of 8.9±1.4 m/s (Socha et al., 2005) and a characteristic length of 2.2 cm (chord length; (Miklasz et al., 2010)), we chose C_l and C_d values corresponding to Re = 11000.

The use of steady-state aerodynamic force coefficients to model undulating snakes is not ideal, but these coefficients are a reasonable approximation to use in our first-order modeling. As explained in detail by Holden et al. (2014), the speed of the snake's forward motion in gliding is much greater than the motions of undulation, which suggests that the freestream velocity should dominate the local airflow patterns over the body. This suggests that it is reasonable to use these force coefficients in a first study. Future modeling should incorporate unsteady and tandem aerodynamic effects on the snake, when such results become available.

2.2. Model 1

In the first model, we considered the snake as three evenly spaced airfoils (Fig. 2). These airfoils represent sections of the snake's body whose long axis (span) is roughly perpendicular to the direction of motion. The distance d between the airfoils (Fig. 2A) can be characterized as half of the undulation wavelength (Fig. 2B). We restrict the airfoils to remain coplanar. The previously measured kinematics of body movements (Socha et al., 2010) justifies this restriction, showing that total displacements of several landmarks on the snake's body, perpendicular to the 'mean' body orientation, are about 10% of the snout-vent length (Fig. 1C). Because no data are available about the local angles of attack along the snake body, as a reasonable first approximation we assumed that the airfoil orientation could be differentiated from the pitch angle θ by the same constant angle φ for all of the airfoils (Fig. 2A). The angle φ represents the angle between the chord line of each airfoil and the line that defines the whole-body orientation (i.e., the 3-foil system). Further, we assumed that mass and pressure are uniformly distributed along the "wings". The basic assumption for the aerodynamics of this model is that the main contribution to producing force comes from those parts of the body that are perpendicular to the air flow, and that the curved portions contribute negligible force.

To simulate undulation, we allowed the masses and, proportionally, areas of the segments to vary as the following functions of time:

$$\begin{cases} m_1(t) = m_a + \Delta m \cos \omega t \\ m_2(t) = m_{tot} - 2m_a \\ m_3(t) = m_a - \Delta m \cos \omega t \end{cases} \tag{1}$$

where ω is the frequency of undulation and m_{tot} is the total mass of the snake, with $m_1(t) + m_2(t) + m_3(t) = m_{tot}$. The constraint $\Delta m < m_a$ applies to Eq. (1).

The equations of motion of Model 1, whose kinematics are shown in Fig. 2C, are written as:

$$\begin{aligned} & m_{tot}\left(\ddot{x}\mathbf{i} + \ddot{z}\mathbf{j}\right) - 2\Delta m d \cos \omega t \left[\left(\ddot{\theta}\sin\theta + \dot{\theta}^2 \cos\theta\right)\mathbf{i} + \left(-\ddot{\theta}\cos\theta + \dot{\theta}^2 \sin\theta\right)\mathbf{j}\right] \\ & = \sum \left(F_{lj}\sin\gamma_j - F_{dj}\cos\gamma_j\right)\mathbf{i} + \left(F_{lj}\cos\gamma_j + F_{dj}\sin\gamma_j - m_j g\right)\mathbf{j} \end{aligned} \tag{2}$$

$$2\left[\frac{m_a}{m_{tot}} - \left(\frac{\Delta m}{m_{tot}}\right)^2 \cos 2\omega t\right] m_{tot} d^2 \ddot{\theta} = \sum d_j \left(F_{lj}\cos\left(\theta + \gamma_j\right) + F_{dj}\sin\left(\theta + \gamma_j\right)\right) \tag{3}$$

where g is the gravitational acceleration, d_j is the position of airfoils relative to CoM along the longitudinal axis of the body, and γ_j is the glide angle of each airfoil. See Appendix A1 for the detailed derivation of these equations. The lift and drag forces were calculated as:

$$\begin{cases} F_{lj} = \rho_{air} C_{lj} v_j^2 S_{aj} / 2 \\ F_{dj} = \rho_{air} C_{dj} v_j^2 S_{aj} / 2 \end{cases} \tag{4}$$

where C_{lj} and C_{dj} are the force coefficients, and S_{aj} is the area of each airfoil.

Eqs. (2) and (3), together, determine the trajectory of the model when released from any initial position. In the simulations, we set φ equal to the value given in Table 2 (see section 2.6 for details).

To study the steady-state behavior of Model 1, we first observe that the equations of motion are nonautonomous, i.e. they explicitly depend on time. Although nonautonomous systems are not usually expected to have equilibrium solutions, we note that with $\dot{\theta} = 0$, the airfoils have the same velocity and experience the same angle of attack (see Appendix A1). By substituting Eq. (4) into the right hand side of Eq. (3), it can be readily shown that, in this case, CoP coincides with CoM; therefore, the net moment about CoM vanishes and Eq. (3) is identically satisfied. Also, Eq. (2) reduces to:

$$m_{tot}\left(\ddot{x}\mathbf{i} + \ddot{z}\mathbf{j}\right) = \left(F_l \sin\gamma - F_d \cos\gamma\right)\mathbf{i} + \left(F_l \cos\gamma + F_d \sin\gamma - m_{tot} g\right)\mathbf{j} \tag{5}$$

where F_l and F_d are the net lift and drag forces acting on the model and are not explicitly time-dependent.

Eq. (5) is equivalent to the equations of motion for a fixed-shape glider, resulting in definite values for equilibrium speed and glide angle. The stability of the equilibrium solution depends on the initial conditions from which the trajectory starts; therefore, the equilibrium is locally stable. Additionally, it is passively stable because stability is inherent in the model's behavior without using closed-loop feedback control.

2.3. Model 2

Model 2 was developed based on the idea that the snake maintains a staggered configuration in mid-air, but different parts of the body move relative to one another. In this 2D model, illustrated

in Fig. 3, two airfoils are connected through a rigid link by means of multiple springs and dampers. The airfoils and the long axis of the middle link are restricted to remain collinear, but they are free to move with respect to each other under the action of gravity, aerodynamic forces, and the springs and dampers. The effect of the springs and dampers is shown in Fig. 3A by the forces $\mathbf{f}_1$ and $\mathbf{f}_2$, which have magnitudes:

$$\begin{cases} f_1 = k\left(r_1 - l\right) + b\dot{r}_1 \\ f_2 = k\left(r_2 - l\right) + b\dot{r}_2 \end{cases} \tag{6}$$

where l is half of the length of the middle link and the free length of the connecting springs.

Fig. 3B depicts a top view of Model 2. Compared to Model 1, the middle link is added in this model to represent the role of the parts of the body of the snake that are almost parallel to the direction of motion (Fig. 3C), which provides rotational inertia. Based on the assumption that aerodynamic forces are mainly produced by segments that are perpendicular to the flow, we ignored the aerodynamic contribution from this streamwise middle link. Another modification in Model 2 is that only two airfoils are used, in contrast to three airfoils in Model 1. Because the middle airfoil in Model 1 had no role in the equations of motion, it was removed in Model 2 for the sake of abstraction. The two remaining airfoils were sufficient to produce external forces and moments; therefore, the dynamics of the snake could be adequately approximated by Model 2.

Two more assumptions are present in the construction of Model 2, which are are also used in Model 1: (i) the airfoils are constrained to move only along the orientation of the middle link, and (ii) the airfoils have the same angle of attack. Similar to Model 1, the effects of undulation were modeled by allowing the mass of the airfoils to change sinusoidally, such that the total mass of the system remains constant:

$$\begin{cases} m_1\left(t\right) = m_{a1} + \Delta m \cos\left(\omega t + \sigma\right) \\ m_2\left(t\right) = m_{a2} - \Delta m \cos\left(\omega t + \sigma\right) \end{cases} \tag{7}$$

where σ is some phase angle and is considered to account for the phase within the undulation cycle at the starting point. Application of Eq. (7) is subject to the restriction that $\Delta m < m_{a1}, m_{a1}$. The mass of the middle link m_i is held fixed. We further assume that the areas of the airfoils are proportional to their masses.

In the previous section, Model 1 was shown to possess locally stable equilibrium solutions, because its structure allowed a uniform distribution of aerodynamic forces. However, in Model 2,

presence of the middle link, which does not produce any aerodynamic forces, makes it impossible that such a solution be obtained. Therefore, active control is required in Model 2 to stabilize the trajectories. We used a restoring moment in Model 2 to represent the overall effect of control movements. Based on kinematic observations showing that the snake's body remains roughly level with the ground in mid-glide (Socha et al., 2010), a linearized form was considered for the restoring moment, which would maintain the pitch angle θ close to zero. Similar to expressions that have been commonly used to stabilize models of flying animals (see e.g. (Cheng et al., 2011)), we let:

$$M_u = K_u\theta + B_u\dot{\theta} \tag{8}$$

It is important to note that the proportionality term $K_u\theta$ might not be sufficient for control, because it could overcompensate to disturbances and lead to divergent oscillations. Therefore, a damping term $B_u\dot{\theta}$ was also included to dissipate the unwanted pitching motion.

2.4. Equations of motion for Model 2

Before deriving the equations of motion, a few definitions are presented for convenience of notation. We select $\mathbf{x} = \begin{bmatrix} x & z & \theta & r_1 & r_2 \end{bmatrix}^T$ (see Fig. 3A) as the vector of generalized coordinates of the system. Among these variables, x and z define the position of the model as a whole in the plane of motion and are called the position variables, while r_1, r_2 and θ determine the relative position of model segments and are called the configuration variables. Additionally, we define the state vector as:

$$\mathbf{y} = \begin{bmatrix} \theta & r_1 & r_2 & \dot{x} & \dot{z} & \dot{\theta} & \dot{r}_1 & \dot{r}_2 \end{bmatrix}^T \tag{9}$$

The reason for excluding the position variables from the state vector is that, unlike state variables, they will not settle to periodic motions, and prevent obtaining a periodic steady-state solutions (see section 2.6 for more details).

The equations of motion are derived using a Lagrangian formulation, and are written in the following matrix form:

$$\mathbf{M}(\mathbf{x},t)\ddot{\mathbf{x}} + \mathbf{c}(\mathbf{x},\dot{\mathbf{x}},t) + \mathbf{g}(\mathbf{x},t) = \mathbf{q}(\mathbf{x},\dot{\mathbf{x}},t) + \mathbf{f}(\mathbf{x},\dot{\mathbf{x}})\sin(\omega t + \sigma) \tag{10}$$

where $\mathbf{M}(\mathbf{x},t)$ is the mass matrix, $\mathbf{c}(\mathbf{x},\dot{\mathbf{x}},t)$ is a vector containing the centrifugal, Coriolis and damping terms, $\mathbf{g}(\mathbf{x},t)$ contains the gravitational and elastic terms, and $\mathbf{q}(\mathbf{x},\dot{\mathbf{x}},t)$ is the vector of generalized force. Also, $\mathbf{f}(\mathbf{x},\dot{\mathbf{x}})$ is a forcing term produced by the transport of mass between the airfoils, whose harmonic behavior is shown in Eq. (10).

Upon integration of Eq. (10) from any initial condition, the glide trajectory of the model can be determined. A detailed derivation of Eq. (10) including explicit formulae for the terms is provided in Appendix A1.

2.5. Determination of parameters for Model 2

It can be seen from Fig. 3 and Eqs. (6-8) that Model 2 involves multiple parameters, including the inertial parameters m_{a1}, m_{a2}, Δm, m_i and I_i; biomechanical parameters k and b; geometric parameters l, σ and φ; and control parameters K_u and B_u. Among these, determining K_u and B_u required fitting the model to observed glide trajectories of snakes, by formulating it as an optimization problem (see below). This approach has been commonly used when control system parameters are dealt with; for example, Cheng et al. (2011) determine the characteristic coefficients of the feedback control system of a hawkmoth model using a similar approach. Because direct measurement of other parameters from live specimens of flying snakes was not possible for this study, we chose to use a data fitting procedure to find model parameters by requiring that the resulting model would reproduce the observed glide trajectories as close as possible.

We chose to use glide trajectory data from a previous study (Socha et al., 2010), using a representative snake 42.0 g in mass and 74.0 cm in snout-vent (SVL) length. Based on another study (Socha et al., 2005) and following Miklasz et al. (2010), we estimated that this snake created an airfoil with a chord of 2.2 cm by flattening its body.

To simplify the formulation, the following nondimensionalized inertial parameters were used in the process:

$$\begin{cases} \eta_1 = m_{a1}/m_{tot} \\ \eta_2 = m_{a2}/m_{tot} \\ \xi = \Delta m/m_{tot} \end{cases}, \ \mu = \frac{I_i}{m_i l^2/3} \tag{11}$$

Eq. (7) could then be rewritten as:

$$\begin{cases} m_1 = \left[\eta_1 + \xi\cos(\omega t + \sigma)\right] m_{tot} \\ m_2 = \left[\eta_2 - \xi\cos(\omega t + \sigma)\right] m_{tot} \end{cases} \tag{12}$$

We thus obtain the mass and moment of inertia of the middle link as:

$$m_i = (1 - \eta_1 - \eta_2) m_{tot} \tag{13a}$$

$$I_i = \mu(1 - \eta_1 - \eta_2)\frac{1}{3} m_{tot} l^2 \tag{13b}$$

Using the assumption that the projected areas of the airfoils are proportional to their masses, we could also find the airfoil area S_a from Eq. (12):

$$S_{aj} = \frac{m_j}{m_{tot}} l_{SV} c \ , \ j = 1,2 \tag{14}$$

where l_{SV} and c are SVL and airfoil chord, respectively. S_a is used along with the aerodynamic coefficients to calculate the lift and drag forces.

Finally, the error between the recorded trajectory and the theoretical trajectory obtained by integration of Eq. (10) is defined in the least squares sense as:

$$e = \int_{t_1}^{t_2} \left[\left(x_r(t) - x_m(t)\right)^2 + \left(z_r(t) - z_m(t)\right)^2 \right] dt \tag{15}$$

where the subscripts r and m denote the recorded and model trajectories, respectively. The model parameters are the solution to an optimization problem in which the error in Eq. (15) is considered as the objective function to be minimized.

It is important to note that the discretized form of Eq. (15) was used here, because the measured data existed at a series of discrete time steps. We used the initial conditions based on the previous trajectory data (Table 1). We chose initial values of x, z and θ from the measured data, whereas the initial values of $\dot{x}$, $\dot{z}$ and $\dot{\theta}$ were calculated using a finite difference formula. Because no measured data existed for r_1 and r_2, we simply integrated these variables from rest ($r_1 = r_2 = l$ and $\dot{r}_1 = \dot{r}_2 = 0$).

2.6. Stability analysis

To analyze the stability characteristics of a system in the sense of dynamic stability, we first need to determine its steady-state response. Model 2, as described by Eq. (10), is nonautonomous and periodically forced with the frequency of undulation. Hence, the steady-state response of Model 2 is periodic in state space and has the same frequency. As a side note, it should now be clear that in order to be able to obtain periodic solutions, we had to define the state vector as in Eq. (9), because the trajectory in the x-z plane is not periodic. We can assess the stability of the periodic solution by applying the Floquet theory (Nayfeh and Balachandran, 2004), which is described below.

Due to the complexity of the equations of motion of Model 2, analytical solutions were not attempted; instead, we employed a finite difference method to determine the solution to Eq. (10). First, a sufficiently small step size was selected to construct a dense set of time steps spanning one period of undulation. Then, a central difference formula was used to approximate the time derivative of the state vector at the midpoint of each interval. By imposing the periodicity condition, a set of algebraic equations was obtained in terms of discrete states at the steps, sufficient to solve for discrete states, determining the periodic solution (Nayfeh and Balachandran, 2004). This periodic solution is called $\mathbf{y}_0(t)$, and we denote its period by τ.

To examine the dynamic stability of $\mathbf{y}_0(t)$, Eq. (10) is first rewritten in the following state space form:

$$\dot{\mathbf{y}} = \dot{\mathbf{y}}(\mathbf{y}, t; p) \tag{16}$$

where p could be any parameter. A disturbance $\tilde{\mathbf{y}}(t)$ is superimposed on $\mathbf{y}_0(t)$, so that:

$$\mathbf{y}(t) = \mathbf{y}_0(t) + \tilde{\mathbf{y}}(t) \tag{17}$$

Next, Eq. (17) is substituted into Eq. (16), a Taylor series expansion is used about $\mathbf{y}_0(t)$, and linear terms in the disturbance are retained. It follows that:

$$\dot{\tilde{\mathbf{y}}} = \left.\frac{\partial \dot{\mathbf{y}}}{\partial \mathbf{y}}\right|_{\mathbf{y}_0} \tilde{\mathbf{y}} = \mathbf{A}(t; p)\tilde{\mathbf{y}} \tag{18}$$

where $\mathbf{A}(t;p)$ is the Jacobian matrix. The linearly independent solutions of Eq. (18) are collected in a matrix form as below:

$$\tilde{\mathbf{Y}}(t) = \left[\tilde{\mathbf{y}}_1(t) \ \tilde{\mathbf{y}}_2(t) \ \cdots \ \tilde{\mathbf{y}}_8(t) \right] \tag{19}$$

$\tilde{\mathbf{Y}}(t)$ is the fundamental matrix solution and satisfies the differential equation:

$$\dot{\tilde{\mathbf{Y}}}(t) = \mathbf{A}(t;p)\tilde{\mathbf{Y}}(t) \tag{20}$$

When integrated from the initial condition $\tilde{\mathbf{Y}}(0) = \mathbf{I}$, the fundamental matrix solution evaluated at the period τ is called the monodromy matrix; i.e.,

$$\Phi = \tilde{\mathbf{Y}}(\tau) \tag{21}$$

The eigenvalues of the monodromy matrix, Φ, are called Floquet multipliers. The Floquet theory states that stability of $\mathbf{y}_0(t)$ is determined by the following condition: if all of the Floquet multipliers are within the unit circle in the complex plane, the periodic solution is stable (Nayfeh and Balachandran, 2004).

The effect of parameter p on the stability of $\mathbf{y}_0(t)$ can be determined by examining whether changes in the value of p cause a Floquet multiplier to enter or exit the unit circle. For the case of Model 2, parameters of interest are K_u and B_u, and Δm (or equivalently ζ, which is a measure of undulating amplitude and could be used to determine the effect of undulation on the pitch stability of the model). A previous study of flying snake kinematics (Socha and LaBarbera, 2005) found no correlation between undulation frequency and any glide performance variable. Therefore, we do not consider this parameter here. Among the parameters of interest, the amplitude of undulation, ζ, requires further elaboration, because the forcing term $\mathbf{f}(\mathbf{x},\dot{\mathbf{x}})$ is proportional to it; see Eq. (S21). As this parameter goes to zero, the steady-state response continuously transforms from a periodic to an equilibrium solution, for which the Floquet theory can no longer be applied. In this case, the eigenvalues associated with the linearized equations of motion have to be obtained; for an equilibrium solution to be dynamically stable, all of these eigenvalues must have negative real parts (Nayfeh and Balachandran, 2004).

Here, for an equilibrium solution of Model 2 with $\zeta = 0$ (i.e., without undulation), we instead applied the static stability criterion, which determines the ability of a system to produce a

restoring effect after receiving a disturbance, and is a necessary condition for dynamic stability. In planar motion, the analysis of static stability in the pitch direction reduces to determining the slope with which pitching moment, M_c, varies with angle of attack, α_b. If the slope is negative, i.e.,

$$\frac{\partial M_c}{\partial \alpha_b} < 0 \tag{22}$$

this means that a disturbance from equilibrium passively induces an opposing pitching moment, and the system is statically stable (Taylor and Thomas, 2002). This criterion was applied to Model 2 without undulation as follows:

We kept the pitch angle θ constant, integrated Eq. (10) with respect to other generalized coordinates, giving sufficient time to let them reach steady state. Then, the reference angle of attack was found as:

$$\alpha_b = \theta - \tan^{-1}\left(\dot{z}/\dot{x}\right) \tag{23}$$

Also, the pitching moment was obtained as:

$$M_c = \left(r_1 - r_c\right)\left(F_{l1}\cos\beta_1 + F_{d1}\sin\beta_1\right) - \left(r_2 + r_c\right)\left(F_{l2}\cos\beta_2 + F_{d2}\sin\beta_2\right) - K_u\theta \tag{24}$$

with $\beta_j, j = 1,2$ defined in Eq. (S15), and r_c being the position of CoM with respect to the center of the middle link, calculated as:

$$r_c = \left(m_1 r_1 - m_2 r_2\right)/m_{tot} \tag{25}$$

By repeating the above procedure while changing the pitch angle, a curve is constructed displaying the relation between the pitching moment and angle of attack. The stability criterion of Eq. (22) was applied to this curve. For comparison, this criterion was also applied to the model with undulation. For this case, the reference angle of attack and the pitching moment had to be averaged over one period of undulation. Finally, we varied K_u to examine the effect of the control term on the static stability properties of the system.

2.7. Simulations

We used custom-written programs in MATLAB (version 2010a) to integrate the equations of motion (using ode functions), to solve the parameter-fitting problem (formulated as an optimization problem and solved using the fmincon function) and to perform the subsequent

simulations. The sequential quadratic programming algorithm was employed to solve the optimization problem and to find the unknown model parameters within a definite range determined by lower and upper bounds. These bounds were imposed on the solution to ensure a biomechanically realistic solution. The optimization process resulted in several local minima of the error function, among which we selected the solution associated with the least error value.

We carried out several simulations with the developed models, using initial conditions that are summarized in Table 1. In addition, we used $m_a = m_{tot}/4$ and $\Delta m = m_{tot}/4$ for Model 1. The fitted parameters for Model 2 are given in Table 2 along with the lower and upper bounds against which they were obtained. For consistency, the value of φ obtained for Model 2 was used for both models in all simulations.

3. Results

3.1. Trajectory simulations

To investigate how the developed theoretical models predict the transition from the ballistic phase to the shallowing phase, the trajectories and corresponding glide angles starting from $(\dot{x}_0\,,\dot{z}_0) = (1.7\,,0)$ m/s were compared to the experimental trajectories in Socha et al. (2005) (Figs. 4A and 4B). Because no data exist on the initial pitch angle of the snake, we assumed reasonable values for the simulations. Fig 4A shows that Model 1 with $\theta_0 = -10°$ produced a trajectory that followed the experimental data; it also shows that the trajectories predicted by Model 1 do not change monotonically with θ_0. When the initial pitch angle is decreased from zero to $\theta_0 = -10°$, the distance traveled increased by about 20%; but if θ_0 is further decreased to $\theta_0 = -30°$, the traveled distance is less than halved. Fig. 4B shows that no shallowing phase exists for Model 1 with $\theta_0 = -30°$, but the glide angle tends to an equilibrium value of about 70°. It can be also observed that the trajectory of Model 1 with $\theta_0 = 0°$, reaches equilibrium in less than 1.5 s, while the experimental glide angle continues to decrease even after 2 s. On the other hand, the trajectories predicted by Model 2 change monotonically with θ_0, and do not seem to

reach equilibrium by the end of the simulation time; however, they underperform in horizontal distance travelled relative to both Model 1 and the experimental data.

The reason for the non-monotonic behavior of Model 1 may be readily explained if we recall the following equation for the equilibrium glide angle:

$$\tan\gamma = \frac{C_d}{C_l} = f(\alpha) \tag{26}$$

where α is the angle of attack, and $f(\alpha)$ is a nonmonotonic function (see Fig. 1F).

The vertical and horizontal components of the velocity are also plotted in Figs. 4C and 4D, respectively. As with the other performance metrics, it is clear that the simulated velocities do not closely match the experimental velocities. The velocities predicted by Model 2 have relatively similar trends to those of real snakes, for which the vertical velocity starts to increase in magnitude for roughly one second, after which sufficient airspeed is achieved and lift is generated to provide a positive vertical acceleration. Moreover, the horizontal velocity shows a positive acceleration during the whole time, although the acceleration starts to diminish after 1.5 s. However, the simulated velocities are considerably smaller in magnitude than the experimental data; whereas the largest vertical speed of snakes is ~6 m/s, the simulated vertical speeds reach a maximum of ~4.5 m/s. (Fig. 4C). The velocity magnitude deficit is particularly obvious in the horizontal component of the velocities, which leads to the steep shallowing trajectories of Model 2 (Fig. 4D). The same discrepancies exist in the results of Model 1, in addition to the aberrant behavior of the vertical speed with $\theta_0 = 0°$, where positive acceleration is never attained.

Fig. 5 compares the recorded trajectory and pitch angle of a flying snake to the simulated ones obtained by integrating equations of motion of Model 2 from the same initial conditions. The experimental trajectory of the CoM, shown in Fig. 5A, was calculated based on the 3D kinematic data of five landmarks on the snake body, recorded from the mid-to-end portion of the glide (Socha et al., 2010). The experimental pitch angle, which was originally calculated using the same kinematic data, is repeated from Fig. 1A. It can be seen that the simulated trajectory closely follows the recorded data; the maximum position difference between model and observed results was 13 cm over a total distance of more than 12 m traveled, resulting in a relative difference of 1.0%. On the other hand, the simulated pitch angle deviates largely from the recorded data. In particular, it seems that a phase shift exists between the two time series, although they exhibit the same dominant frequency, which is equal to the frequency of

undulation. In addition, the amplitude of oscillations of the experimental pitch angle is roughly twice that of the simulated one.

3.2. Stability analysis

Model 1 was shown to have an equilibrium solution, although its equations of motion were nonautonomous. A trial-and-error investigation of the initial conditions revealed that the equilibrium of Model 1 is locally passively stable. The blue region in Fig. 6A shows the basin of stability of the equilibrium in the $\theta_0 - \dot{\theta}_0$ plane, with the initial velocities set as the same as those of the experimental trajectories (see Fig. 4). It is clear that many of the snake-related initial conditions lie within the basin of stability of equilibrium. The trajectories that start from the initial conditions in blue go to the equilibrium state, whereas the initial conditions in red result in non-gliding trajectories similar to those of a pure projectile (Fig. 6B).

To explore the stability properties of Model 2, the static stability criterion was first applied. As stated previously, this criterion provides a necessary condition only for stability of equilibrium solutions of a system. However, the steady-state response of Model 2 is periodic unless Δm is nullified; in other words, undulation effects had to be eliminated from the model for the stability criterion to be properly applied. Here, for the sake of comparison, we also examined the model with undulation by averaging its steady-state response over one period and applying the criterion to the averaged response. Finally, the effect of the controlling term K_u on stability of the model was examined by varying it from zero to its fitted value (Table 2).

The results of the above analysis are given in Fig. 7A. It is clear from the positive slope of the $M_c - \alpha_b$ curves with $K_u = 0$ that the model is unstable when no restoring moment acts on it. However, in all other cases, the slopes of the curves are negative, indicating that the restoring moment is capable of stabilizing the pitch dynamics, at least in the static sense. It is also important to note that undulation somewhat affects the $M_c - \alpha_b$ curves; it slightly changes the slopes near the equilibrium point at $\alpha_b \approx 26°$, and adds an unstable equilibrium point to the curve with $K_u = 0.02$ Nm/rad. However, it does not change the qualitative behavior of the curves near the stabilized equilibrium; therefore, the static stability analysis predicts that pitching stability cannot be achieved in Model 2 with $K_u = 0$ just by switching undulation on or off.

The dynamic stability analysis of the periodic motions of Model 2 was also carried out using the Floquet theory. Figs. 7B-7D show all of the Floquet multipliers associated with six periodic solutions (each one resulting in 8 Floquet multipliers) obtained by gradually changing a parameter of the model. The parameters of interest were the undulating amplitude index ζ and the control indices K_u and B_u. We examined the effects of these parameters by varying them in the ranges $0.1\zeta^{opt} < \zeta < \zeta^{opt}$, $0.2K_u^{opt} < K_u < K_u^{opt}$, and $0.3B_u^{opt} < B_u < B_u^{opt}$, one at a time. All other parameters of the model were kept fixed at their fitted values (Table 2). When varying ζ, we used $K_u = 0.2K_u^{opt}$ instead of $K_u = K_u^{opt}$; this choice was made to test if undulation could compensate when the control parameter was too small to provide stability on its own.

Fig. 7B shows that one of the Floquet multipliers enters the unit circle through +1 by increasing the undulation amplitude with $\zeta > 0.1\zeta^{opt}$, but the same multipliers later exits the unit circle through +1 when the undulation amplitude is further increased with $\zeta > 0.9\zeta^{opt}$. This means that undulation with amplitude bigger than a threshold could in fact compensate for the insufficient control parameter, but when the undulation amplitude increases beyond another threshold, it makes the model unstable again. Figs. 7C and 7D show the effect of the control indices on the stability characteristics of the periodic motions. In Fig. 7C, one of the Floquet multipliers enters the unit circle through +1 with $K_u > 0.2K_u^{opt}$ and, in Fig. 7D, one of the Floquet multipliers enters the unit circle through -1 with $B_u > 0.3B_u^{opt}$. This means that both control terms are required for a stable motion; also, there exist threshold values for these terms below which stability cannot be achieved.

4. Discussion

4.1. Stability analysis of the models

To investigate the theoretical stability characteristics of a flying snake during a glide trajectory, we developed two dynamical models. Model 1 was a simple representation of the staggered configuration of a gliding snake's body. Our analysis shows that the nonautonomous equations of motion of Model 1, indeed, had an equilibrium solution, which was locally

passively stable. This counterintuitive result was an inherent feature of the model's structure, in which the uniform distribution of mass and pressure over the airfoils would cause the CoP and CoM to coincide and, therefore, the pitch equation to be identically satisfied. More interestingly, many of the take-off conditions of flying snakes correspond to the initial conditions within the basin of stability of the equilibrium solution of Model 1. However, the structure of Model 1 requires that all parts of the virtual body contribute equally to producing aerodynamic forces, which is not possible in real gliding snakes due to variation of angle of attack and sweep angle along the body. Model 2 was developed to provide a more sophisticated representation of flying snake's behavior in mid-air. The airfoils were allowed to move with respect to each other; additionally, to account for potential control movements, a restoring moment was included to keep the pitch angle close to zero. This model was unstable in the pitch direction, but could be stabilized with the restoring moment.

An essential feature of snake gliding behavior that was incorporated into the models was undulation. *A priori*, undulation should affect the dynamics of flying snakes through at least three mechanisms: (i) continual changes in areas of the upstream and downstream airfoils, which in turn alters the aerodynamic forces; (ii) continual redistribution of body mass, which changes the position of the CoM; (iii) inertial couplings between the translational and rotational motions (see Eq. (S21)). There are other possible effects of undulation; for instance, it may cause 3D unsteady aerodynamic interactions that are not observed in static measurements, and it has been postulated that it enables stability in the rolling direction (Socha and LaBarbara, 2005), but this was not modeled here. These mechanisms motivated the hypothesis of this study that undulation contributes to stability in the pitch direction, which was tested by applying the Floquet theory to Model 2. As shown by Fig. 7B, undulation with an amplitude properly adjusted between two limits can provide stability in the absence of sufficient control. However, the periodic solution was found to be unstable with $K_u < 0.2K_u^{opt}$ or with $B_u < 0.3B_u^{opt}$ regardless of the influences from undulation. This shows that undulation has a limited capability for providing stability.

The results of Model 2 suggest that flying snakes require active control to perform stable glides. Although the actual control mechanisms that provide stability are not yet known, here we describe some possibilities. The asymmetric effect of pitch velocity on the airspeeds and angles of attack experienced by the upstream and downstream airfoils could be exploited to produce the restoring moment. This might be accomplished (see Fig. 3A) either by actively modifying r_1 and

r_2, or by actively oscillating the airfoils out of the model plane (i.e. the plane defined by the line connecting the airfoils). Both of these mechanisms would change the magnitude and direction of the airfoils' velocities and could be used as means of control. Another potential mechanism could take advantage of the dynamic changes of the aerodynamic load distribution along the snake body. This is in part supported by the results of preliminary tandem model manipulations, which suggest that changing the horizontal gap and vertical stagger affects the lift and drag forces on both airfoils (Miklasz et al., 2010). In some configurations of the tandem models, the lift and drag coefficients of the downstream airfoil are about half of those of the upstream airfoil, but the force coefficients approached those of a solitary airfoil when moved apart by multiple chord lengths. Thus, a 'nose-down' pitching moment could be produced in Model 2 by moving the downstream airfoil farther downstream (increasing r_2), while a 'nose-up' pitching moment requires the opposite movement. Although damping could also be obtained with a similar strategy, it should be recognized that some amount of damping is inherent in the dynamics of Model 2, which originates from the asymmetric effect of pitching velocity on the velocities of the upstream and downstream airfoils. This gives rise to a force asymmetry and a counteracting moment is thereby produced.

Recalling that the flying snakes produce lift using their entire body as a morphing wing, it becomes clear that one functional consequence of the S-shape is that it creates 'upstream' and 'downstream' airfoils. In fact, Miklasz et al. (2010) found that an enhancement in overall lift-to-drag ratio might be achieved with certain configurations. Thus, forming the staggered S-shape may enable such aerodynamic interactions. Moreover, it is well known that no aircraft could be made with a single positively cambered wing, because it would be unstable in the pitching direction (Etkin, 2012). In practice, such wings may be used only in conjunction with an auxiliary surface that provides a nose-up moment when the wing is at zero lift. This may explain another possible function of the aerial snake's S-shape.

4.2. Implications about gliding snakes

The seemingly contradictory results of our two models, when viewed together, render a deeper insight of how the control system of flying snakes works. Model 1 indicates that there exists a passively stable equilibrium state to which the trajectories converge, provided that they

start from proper initial conditions within the basin of stability. Therefore, flying snakes would be able to glide without need for closed-loop feedback control if they could reconfigure their body according to the kinematics of Model 1. However, closed-loop feedback control is likely necessary, resulting from several idealizations in Model 1: (i) the couplings between the longitudinal and lateral motions have been neglected, (ii) mass and aerodynamic forces were distributed uniformly over the body area and, (iii) segments of the body are rigidly coherent. These criteria can never be met by an animal glider. Nonetheless, the ideally passively stable trajectory predicted by Model 1 provides an underlying 'dynamical skeleton' for closed-loop control to work with. A similar framework has been developed for walking in bipeds, which was believed to require active control. However, passively stable gaits have been found in theory, and these have been used to develop passive biped walkers (e.g. (Garcia et al., 1998, Collins et al., 2005)).

The results of Model 2 provide the basis for predictions of how a snake's sensory system should provide feedback on body position and orientation while airborne. The success of Model 2 in predicting stable glide trajectories with a restoring moment proportional to the pitch angle, along with the observation that flying snakes tend to remain level with the ground during gliding, supports the idea that the snakes use pitch angle as a feedback variable in a closed-loop control system. Indeed, both the vestibular and/or visual systems are viable candidates for providing the primary sensory information needed for such control. Boistel et al. (2011) observed that dimensions of the vestibular system in species of squamates capable of descent in the air were different from those in species with only a climbing or terrestrial lifestyle, and suggested that these modifications might be related to the maintenance of stability. Interestingly, the vision of flying snakes has been implicated as being particularly acute compared to that of other snake species (Socha and Sidor, 2005), which may suggest a role in providing visual input to the animal's control system.

This does not exclude the possibility of other measures of position and orientation being utilized as feedback signals; for example, proprioception and pressure distribution information from the skin could provide sensory information. Non-flying snakes are known to possess mechanoreceptors that include rapidly adapting receptors and slowly adapting receptors (Proske, 1969). However, rapidly adaptive receptors have high mechanical thresholds and restricted receptive fields. If flying snakes use skin pressure for feedback, they would require fast

responses to small changes in air pressure. Assuming an ability to sense differences in flow speed on the dm/s scale, this would require mechanoreceptors with a sensitivity on the order of 10^{-2} Pa.

4.3. Gliding trajectories

The theoretical models of this study were based on experimental data from the developed stage of the glide. Our simulations of gliding trajectories (Fig. 4) were conducted with the assumption that the models represented the behavior of flying snakes both in the ballistic dive and shallowing phases. However, the initial ballistic dive involves postural configurations whose effects have not been quantitatively studied. Starting with a straight body, during this phase the snake forms the S-shape and pitches downward (Socha, 2002), bringing itself to the staggered configuration shown in Fig. 1C. Therefore, it is likely that the aerodynamic forces acting on the snake are different in the ballistic dive phase. This might explain why both models predicted trajectories with speeds whose magnitudes are much less those achieved by gliding snakes (Figs. 4C and 4D). Furthermore, Model 2 predicted trajectories that became closer to the measured data when the initial pitch angle was changed from 0° to -30° (Figs. 4A and 4B). By decreasing the initial pitch angle, the model would benefit from smaller angles of attack in the ballistic phase to decrease drag and to obtain greater glide speed by the beginning of the shallowing phase; greater speed would result in greater lift production. Because the restoring moment would increase the glide angle by making the pitch angle tend to zero, smaller initial angles of attack should produce trajectories that are more realistic.

4.4. Conclusion

This study presents two new first-order dynamical models developed to understand the gliding performance of flying snakes, in particular, the stability of the snake about the pitch axis. Model 1, which was a simple two-dimensional representation of the airborne snake as three rigidly attached airfoils, resulted in equilibrium glide trajectories that were locally passively stable. However, with relaxation of the rigidity assumption and other essential features of the gliding snake incorporated into Model 2, the passive stability was lost. It was then shown

that the trajectories of Model 2 could be stabilized with a simple control mechanism using the pitch angle and pitch velocity as feedback. Although the modeling in this study was motivated as an attempt to understand how flying snakes glide, these results may be broadly applicable to a wide array of staggered, multi-winged flyers, at least within the low Reynolds number regime used by the snakes. Our initial first-order modeling also suggests that flying snakes require active control for stable gliding, but caution is warranted in over-extending these results to real gliding flight. Verification of the theoretical models using physical experiments is needed, and a full exploration of the parameter space should be conducted to probe the limits of the system. Furthermore, the biomechanical properties of the snake's body, as well as body orientation angles and muscle activity during gliding, must be measured to understand its control parameters. If experimentally justified, Model 2 would become a powerful tool to study the dynamics of flying snakes, and can be used to examine those aspects of gliding that are difficult, if not impossible, to study experimentally.

Table 1: Initial conditions used for simulations resulting in Figs. 4-6

Variable	Fig. 4	Fig. 5	Fig. 6A
x (m)	0	0	0
z (m)	10	0	10
θ (deg)	-30, -10, 0	-8.85	-30 to 60
r_1 (m)	l	l	
r_2 (m)	l	l	
$\dot{x}$ (m/s)	1.7	6.91	1.7
$\dot{z}$ (m/s)	0	-5.06	0
$\dot{\theta}$ (deg/s)	0	-25.6	-120 to 120
$\dot{r}_1$ (m/s)	0	0	
$\dot{r}_2$ (m/s)	0	0	

Table 2: The model parameters fitted to experimental data along with the lower and upper bounds used in the optimization process

Parameter	Fitted Value	Lower Bound	Upper Bound
η_1	0.379	0.2	0.4
η_2	0.380	0.2	0.4
ζ	0.319	0.25	0.35
l/c	2.981	1	4
μ	0.495	0	2
k (N/m)	0.198	0	2
b (Ns/m)	0.199	0	2
K_u (Nm/rad)	0.119	0	2
B_u (Nms/rad)	0.099	0	2
φ (deg)	-5.39	-30	30
σ (deg)	3.92	-180	180

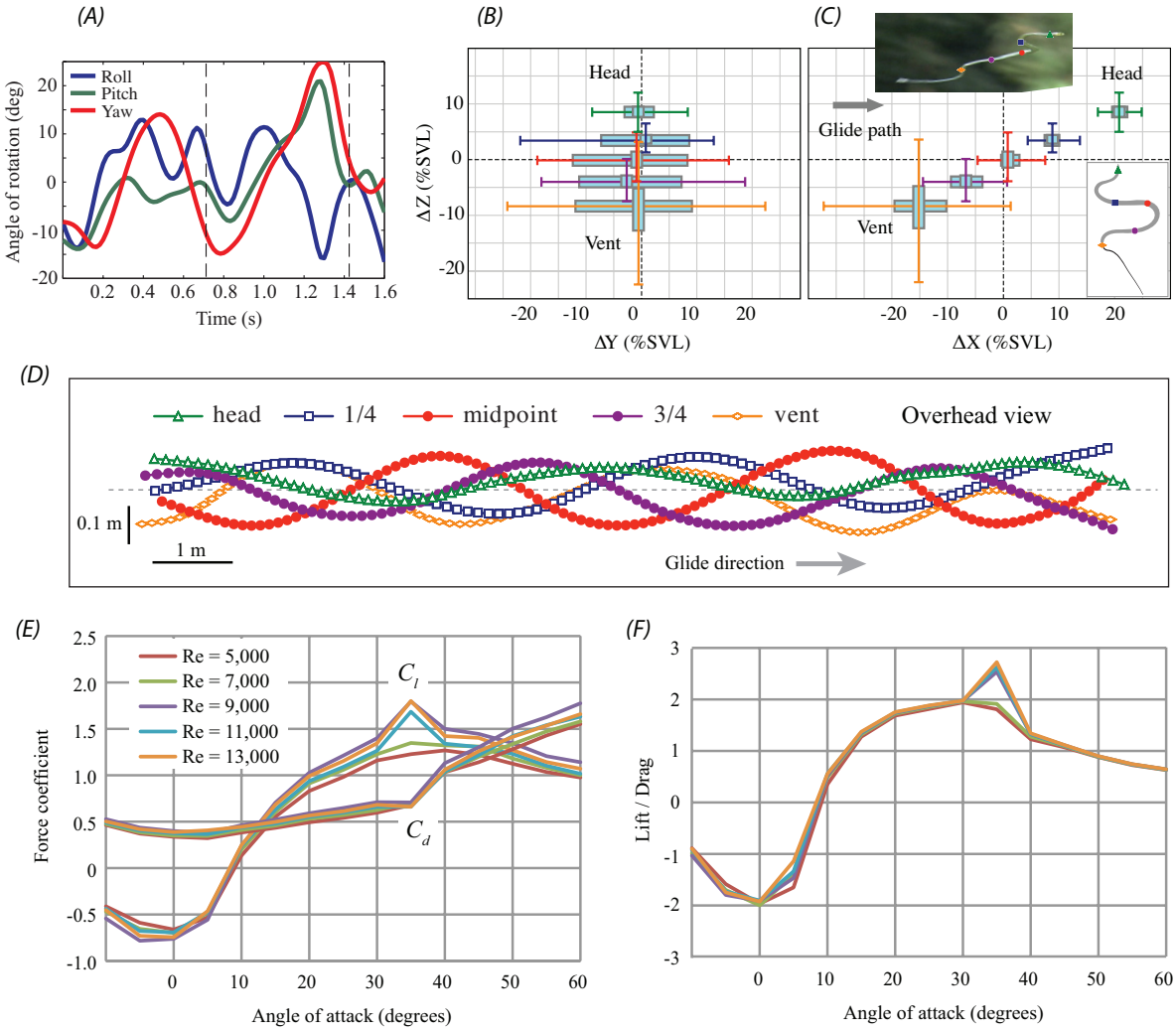

Fig. 1: Kinematic (A-D) and aerodynamic (E-F) data that was used in this study. (A) Observed rotation angles between an inertial frame and the principal axes of inertia of the snake show that the snake undergoes relatively small roll and pitch angles during gliding. (B) Summary of body posture of *C. paradisi*, in the trajectory reference frame and normalized by SVL from the front view, indicate that the snakes undergo small roll displacement. (C) The side view shows the staggered configuration of flying snakes during glide. These data are composed of the 3D position of five landmarks relative to the CoM of the snake body. (D) The sinusoidal movement of all five landmarks is shown in the overhead view of a trajectory, where the Y-axis is expanded relative to the X-axis to better reveal side-to-side movements. The kinematic data in B-D are from late-phase gliding trajectories of eight glide trials performed by two *C. paradisi* snakes (Socha et al, 2010). The box plots indicate the mean, and first and third quartiles, with whiskers representing 10% and 90% percentiles. (E) Steady-state lift and drag coefficients measured for a straight airfoil having the same cross-sectional shape as the flattened snake; and (F) lift-to-drag ratio for the same configuration. The aerodynamic data (E-F) are adapted from (Holden et al., 2014).

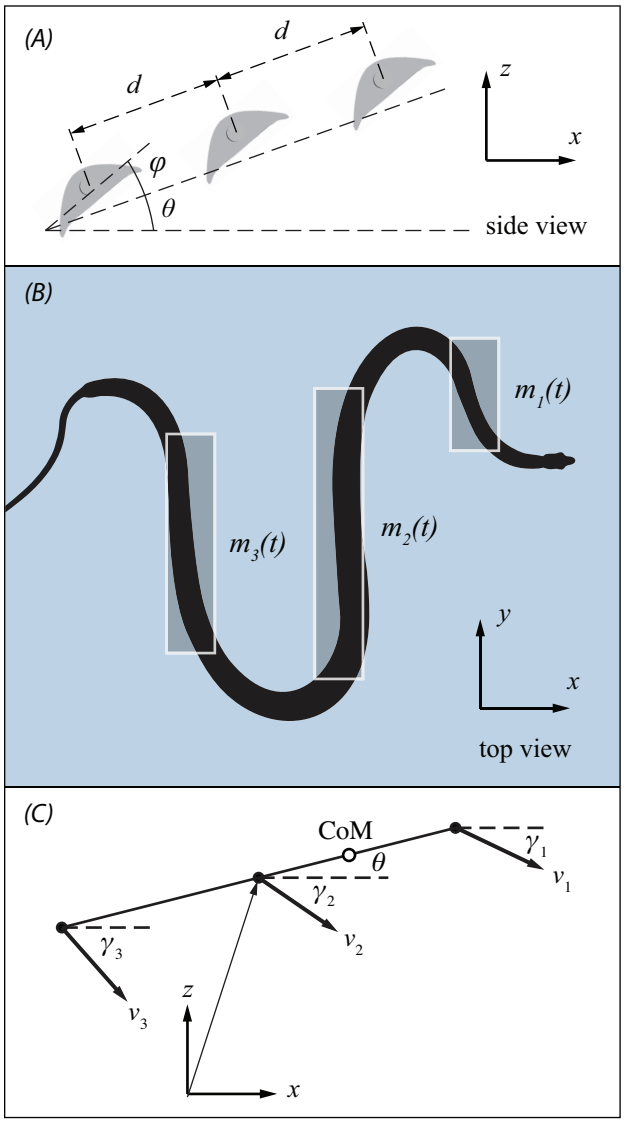

Fig. 2: (A) 2D structure of Model 1, which is composed of three coplanar airfoils; the distance between the airfoils is constant. (B) Correspondence between the airfoils and parts of the undulating snake body that are perpendicular to the airflow. (C) Kinematics of the model showing the asymmetric effect of pitch velocity on the velocity of airfoils. Resulting from this asymmetry, each airfoil experiences a different glide angle γ_j. The middle airfoil is used as the positional reference point.

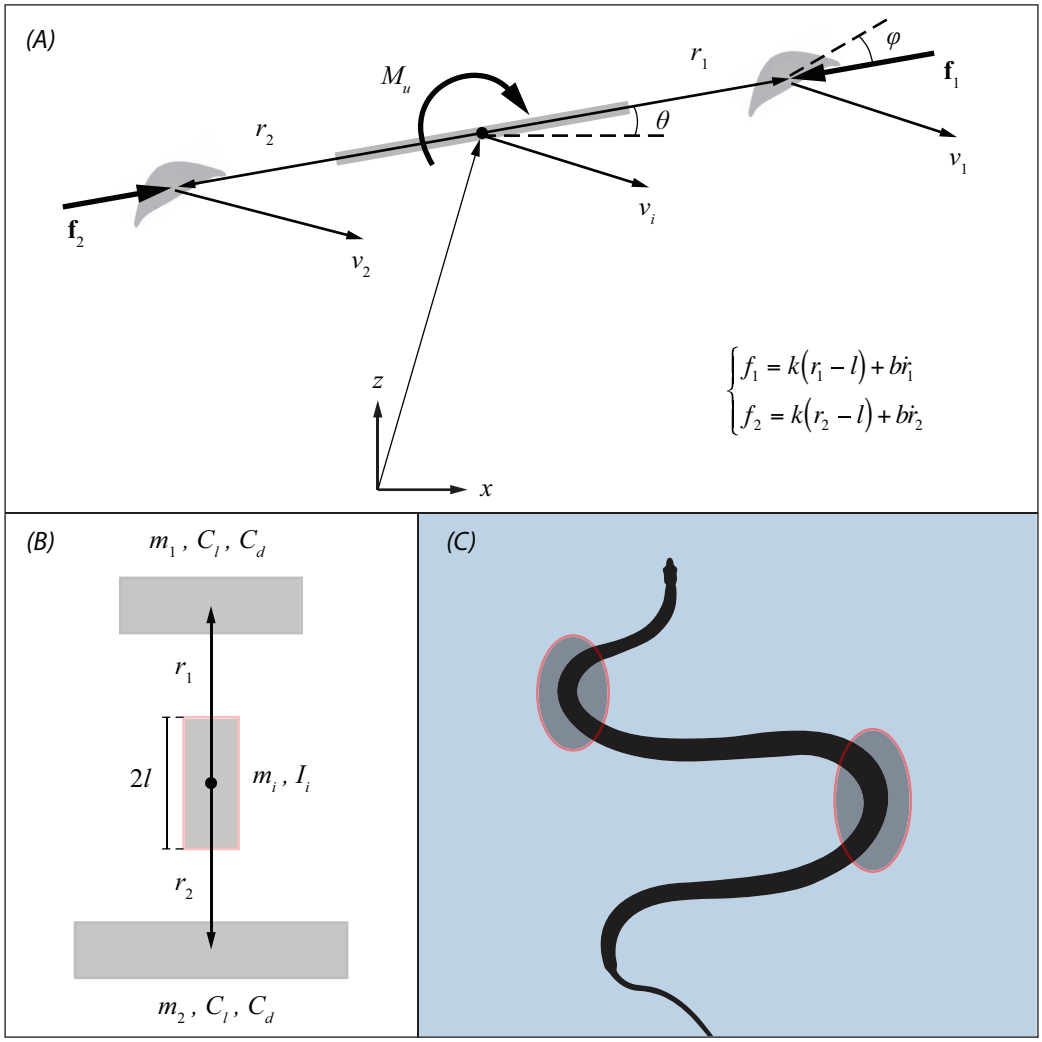

Fig. 3: (A) Model 2 from side view, showing that it is composed of two airfoils connected through a middle link by means of springs and dampers. A restoring moment M_u is used to control the orientation angle θ about zero. The center of the middle link is used as the positional reference point. (B) Overhead view of Model 2. (C) The middle link is included in the model to represent the encircled parts of the snake body. These parts are assumed to not contribute to aerodynamics forces, but do provide rotational inertia.

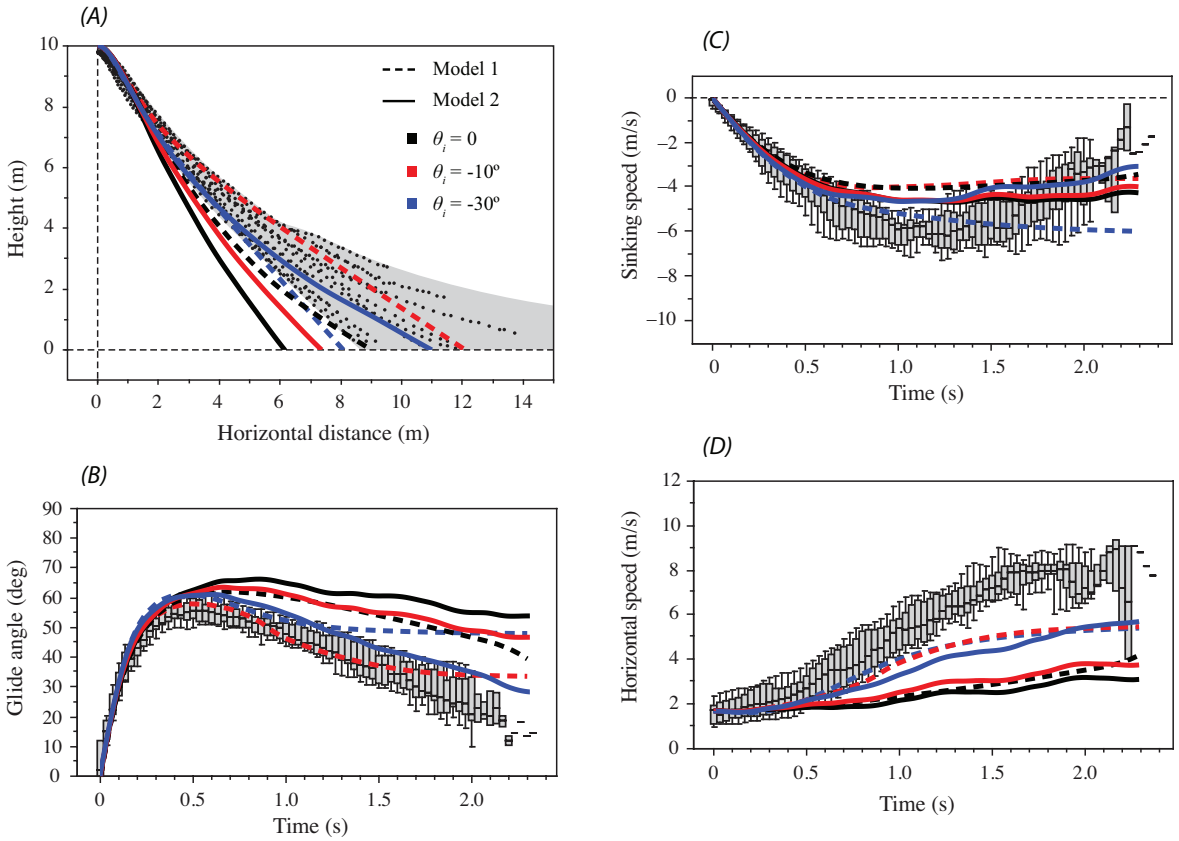

Fig. 4: Comparison of the simulations with an assemblage of experimental data, from Socha et al. (2005). (A) Trajectories and (B) associated glide angles produced by the theoretical models. The trajectories given by Model 1 (dashed lines) reach equilibrium earlier than real snakes, as can be seen in the glide angle data. In contrast, Model 2 (solid lines) produced trajectories that resemble experimental data, but underperform in terms of glide ratio. (C) and (D) show vertical and horizontal components of the velocity, respectively. Whereas both models are incapable of reaching velocities as high as seen in the snakes, Model 2 better predicts the trends in the velocities.

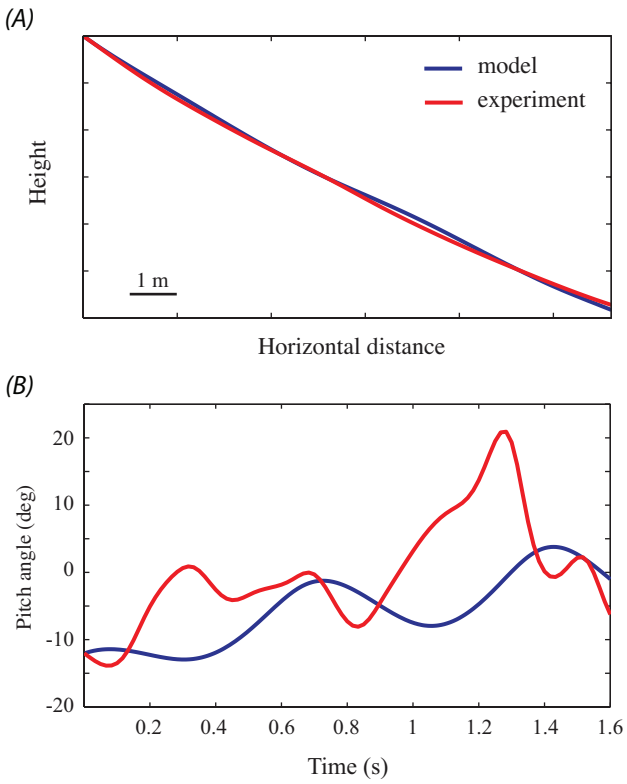

Fig. 5: (A) Model 2 with the fitted parameters successfully reproduced the experimental average trajectory (Socha et al., 2010). Because the data were from the late-phase gliding trajectory, no specific origin was selected for the plot, but only the displacements in the horizontal and vertical directions are shown. (B) The simulated pitch angle deviated from the experimental data. However, the two time series have the same dominant frequency, which is equal to the frequency of undulation.

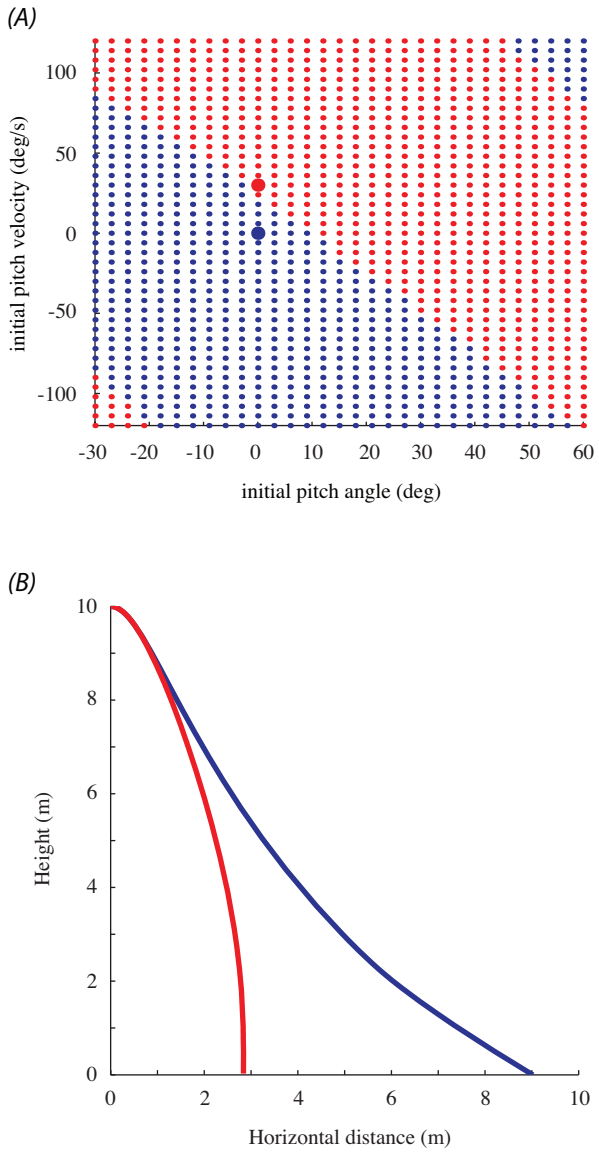

Fig. 6: The equilibrium solution of Model 1 is passively stable, with (A) basin of stability in the $\theta_0 - \dot{\theta}_0$ plane, the initial velocity being $(\dot{x}_0, \dot{z}_0) = (1.7, 0)$ m/s. The trajectories starting from an initial condition within the blue region converge to equilibrium, whereas the initial conditions in red result in trajectories that do not shallow and are similar to those of projectiles. (B) Two representative trajectories starting from the initial conditions singularized in (A).

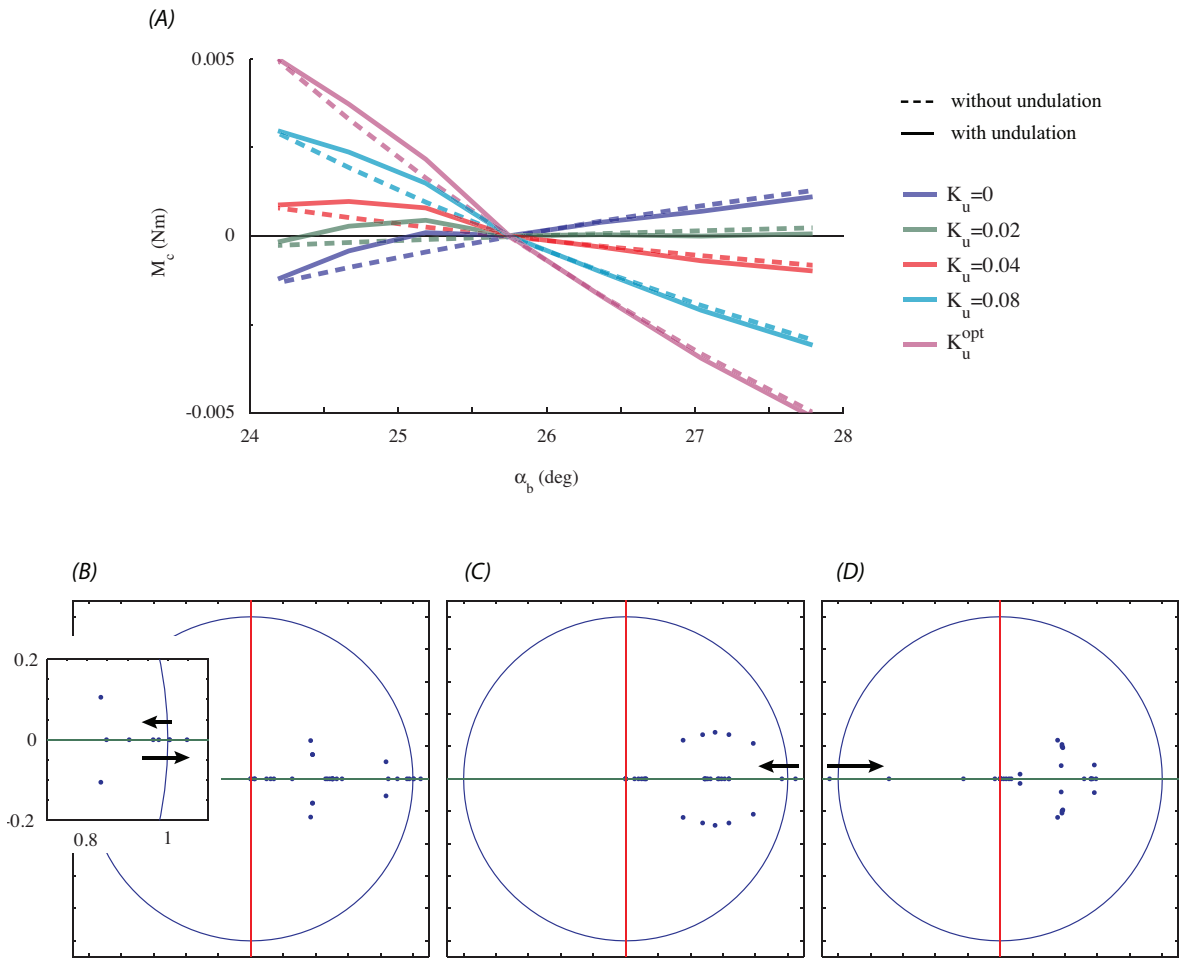

Fig. 7: Results of the static (A) and dynamic (B-D) stability criteria applied to Model 2. (A) Plots of the pitching moment about the CoM, M_c, against the body angle of attack, α_b, with different values of the control parameter K_u. The dashed lines and solid lines correspond to the model with no undulation ($\zeta = 0$) and the model with undulation, respectively. These plots show that the model with $K_u = 0$ is passively unstable, but becomes statically stable with a positive restoring moment. The Floquet multipliers (relative to the unit circle in the complex plane) associated with the periodic motions of Model 2 when (B) $0.1\zeta^{opt} < \zeta < \zeta^{opt}$, (C) $0.2K_u^{opt} < K_u < K_u^{opt}$, and (D) $0.3B_u^{opt} < B_u < B_u^{opt}$. The superscripts denote the fitted values of the parameters (Table 2). The arrow in (B) shows that one of the Floquet multipliers enters the unit circle through +1 with $\zeta > 0.17\zeta^{opt}$, meaning that undulation compensates for a small control and stabilizes the motion (in this case, we set $K_u = 0.2K_u^{opt}$). The arrows in (C) and (D) show that one of the Floquet multipliers enters the unit circle through +1 with $K_u > 0$ and $B_u > 0.1B_u^{opt}$, respectively, meaning that an unstable motion could be stabilized using the restoring moment.

References

ALEXANDER, R. M. 2003. *Principles of animal locomotion*, Princeton University Press.

BIEWENER, A. A. 2003. *Animal locomotion*, Oxford University Press.

BISHOP, K. L. 2006. The relationship between 3-D kinematics and gliding performance in the southern flying squirrel, *Glaucomys volans*. *Journal of Experimental Biology,* 209, 689-701.

BOISTEL, R., HERREL, A., LEBRUN, R., DAGHFOUS, G., TAFFOREAU, P., LOSOS, J. B. & VANHOOYDONCK, B. 2011. Shake rattle and roll: the bony labyrinth and aerial descent in squamates. *Integrative and Comparative Biology,* 51, 957-968.

CHENG, B., DENG, X. & HEDRICK, T. L. 2011. The mechanics and control of pitching manoeuvres in a freely flying hawkmoth (*Manduca sexta*). *Journal of Experimental Biology,* 214, 4092-4106.

COLLINS, S., RUINA, A., TEDRAKE, R. & WISSE, M. 2005. Efficient bipedal robots based on passive-dynamic walkers. *Science,* 307, 1082-1085.

DUDLEY, R. 2002. Mechanisms and implications of animal flight maneuverability. *Integrative and Comparative Biology,* 42, 135-140.

ETKIN, B. 2012. *Dynamics of atmospheric flight*, Courier Dover Publications.

GAO, N., AONO, H. & LIU, H. 2011. Perturbation analysis of 6DoF flight dynamics and passive dynamic stability of hovering fruit fly *Drosophila melanogaster*. *Journal of Theoretical Biology,* 270, 98-111.

GARCIA, M., CHATTERJEE, A., RUINA, A. & COLEMAN, M. 1998. The simplest walking model: stability, complexity, and scaling. *Journal of Biomechanical Engineering,* 120, 281-288.

HEYER, W. R. & PONGSAPIPATANA, S. 1970. Gliding speeds of *Ptychozoon lionatum* (Reptilia: Gekkonidae) and *Chrysopelea ornata* (Reptilia: Colubridae). *Herpetologica*, 317-319.

HOLDEN, D., SOCHA, J. J., CARDWELL, N. D. & VLACHOS, P. P. 2014. Aerodynamics of the flying snake *Chrysopelea paradisi*: how a bluff body cross-sectional shape contributes to gliding performance. *Journal of Experimental Biology,* 217, 382-394.

KRISHNAN, A., SOCHA, J. J., VLACHOS, P. P. & BARBA, L. 2014. Lift and wakes of flying snakes. *Physics of Fluids (1994-present),* 26, 031901.

MCCAY, M. G. 2001. Aerodynamic stability and maneuverability of the gliding frog *Polypedates dennysi*. *Journal of Experimental Biology,* 204, 2817-2826.

MCCORMICK, B. W. 1995. *Aerodynamics, aeronautics, and flight mechanics*, Wiley New York.

MCGUIRE, J. A. 1998. *Phylogenetic systematics, scaling relationships, and the evolution of gliding performance in flying lizards (genus Draco)*. PhD thesis, University of Texas, Austin, TX, USA.

MIKLASZ, K., LABARBERA, M., CHEN, X. & SOCHA, J. 2010. Effects of body cross-sectional shape on flying snake aerodynamics. *Experimental Mechanics,* 50, 1335-1348.

NAYFEH, A. & BALACHANDRAN, B. 2004. *Applied nonlinear dynamics: analytical, computational, and experimental methods non-linear oscillation*. Wiley, New York.

PROSKE, U. 1969. An electrophysiological analysis of cutaneous mechanoreceptors in a snake. *Comparative Biochemistry and Physiology,* 29, 1039-1046.

SCHOLEY, K. 1986. The climbing and gliding locomotion of the giant red flying squirrel *Petaurista petaurista* (Sciuridae). *Biona Report,* 5, 187-204.

SOCHA, J. & SIDOR, C. 2005. *Chrysopelea ornata*, *C. paradisi* (flying snakes): behavior. *Herpetology Review*, 36, 190-1.

SOCHA, J. J. 2002. Kinematics: Gliding flight in the paradise tree snake. *Nature,* 418, 603-604.

SOCHA, J. J. 2011. Gliding flight in Chrysopelea: turning a snake into a wing. *Integrative and Comparative Biology,* 51, 969-982.

SOCHA, J. J. & LABARBERA, M. 2005. Effects of size and behavior on aerial performance of two species of flying snakes (*Chrysopelea*). *Journal of Experimental Biology,* 208, 1835-1847.

SOCHA, J. J., MIKLASZ, K., JAFARI, F. & VLACHOS, P. P. 2010. Non-equilibrium trajectory dynamics and the kinematics of gliding in a flying snake. *Bioinspiration & Biomimetics,* 5, 045002.

SOCHA, J. J., O'DEMPSEY, T. & LABARBERA, M. 2005. A 3-D kinematic analysis of gliding in a flying snake, *Chrysopelea paradisi*. *Journal of Experimental Biology,* 208, 1817-1833.

TAYLOR, G. & THOMAS, A. 2002. Animal flight dynamics II. Longitudinal stability in flapping flight. *Journal of Theoretical Biology,* 214, 351-370.

TAYLOR, G. K. & THOMAS, A. L. 2003. Dynamic flight stability in the desert locust *Schistocerca gregaria*. *Journal of Experimental Biology,* 206, 2803-2829.

THOMAS, A. L. & TAYLOR, G. K. 2001. Animal flight dynamics I. Stability in gliding flight. *Journal of Theoretical Biology,* 212, 399-424.

Chapter 3. Dynamical analysis of undulatory motions in a 3D model of flying snakes

Abstract

Flying snakes of genus *Chrysopelea* possess a highly dynamic gliding behavior, which is dominated by an undulation in the form of lateral waves sent posteriorly down the body. The resulting high-amplitude periodic variations in the distribution of mass and aerodynamic forces have been supposed to contribute to the stability of the snake's gliding trajectory. This is supported by the theory of vibrational control, which employs high-amplitude periodic inputs to produce desireable stable motions in nonlinear systems. However, a previous two-dimensional analysis in the longitudinal plane failed to reveal a significant effect of undulation on the stability of snakes in the pitch direction. In this study, a theoretical model was used to examine the dynamics and stability characteristics of flying snakes in the 3D. The snake was modeled as an articulated chain of airfoils connected through revolute joints. Undulation was considered as a periodic input to the system, either by directly prescribing the joint angles as periodic functions of time, or by assuming periodic torques acting at the joints. The aerodynamic forces were modeled using the blade element theory and the previous force coefficients. The results showed that torque undulation along with linearization-based closed-loop control could increase the size of the basin of stability. The effectiveness of the stabilization provided by the torque undulation was a function of the amplitude and frequency of the input. However, the kinematic undulation was shown to provide open-loop stability for sufficiently large frequencies. The results suggested that the snakes need some extent of closed-loop control in spite of the clear contribution of undulation to the stability of glide. However, as the closed-loop control system needs to work around a passively stable trajectory, it is therefore less demanding.

1. Introduction

Flying snakes have developed a peculiar form of aerial locomotion, which is unique among all flyers. Because the snakes lack any specialized flight anatomy, they have to use their entire body to produce aerodynamic forces both to oppose gravity and to control the trajectory. Upon

becoming airborne, the snakes splay their ribs to the side and create a 'wing' with an unconventional cross-sectional shape. Simultaneously, they assume an S-like shape and send high-amplitude traveling waves posteriorly down the body, producing an aerial undulation (Socha, 2002, Socha, 2006, Socha, 2011, Socha and LaBarbera, 2005, Socha et al., 2010, Socha et al., 2005, Socha et al., 2015). Compared to other biological or engineered flyers that use a pair (sometimes pairs) of bilaterally symmetric wings (Biewener, 2003, Alexander, 2003), snake flight possesses a number of conspicuous characteristics. In particular, (i) snakes glide with a highly dynamic behavior in the form of undulation, as opposed to the generally static posture of other gliders; (ii) the snake's body posture is not bilaterally symmetrical at any moment in time; and (iii) undulatory motion involves significant out-of-plane translation of different parts of the body, a feature not observed in other gliders. As a result of this fundamentally different design, snake flight is expected to entail some unconventional mechanics, which are not explored yet.

Undulation is the most prominent flight behavior of snakes that glide. Its dynamic effects area manifested by the continuous redistribution of body mass and aerodynamic forces. Therefore, undulation must play some functional role related to snake's aerial performance, stability or control. However, despite the growing number of studies on the physical basis of gliding in snakes, the question of why they undulate has not been answered. Jafari et al. (2014) developed 2D theoretical models of snakes to test the hypothesis that undulation contributes to stability in the pitch direction. They concluded that undulation has a limited capacity for providing longitudinal stability. Socha and LaBarbera (2005) used experimental kinematics data to show that undulation was weakly correlated to gliding performance. In particular, they found no relation between performance and undulation frequency, which suggested that frequency is not involved in aerodynamic force production. As a corollary, this also suggests that the quasi-steady forces produced by the animal's forward speed would be sufficient to enable gliding. Holden et al. (2014) made the same argument based on the large advance ratios observed in flying snakes. All in all, the previous studies have not been successful in determining the main function of undulation, which has yet to be understood.

With our current knowledge about flying snakes, the strongest hypothesis about the function of undulation concerns the stability of the airborne snake. This may seem in contradiction to the results of (Jafari et al., 2014); however, it should be noted that in the mentioned study, only the longitudinal dynamics of the snakes were analyzed, and only the

effects of undulation in the pitch direction were considered. It is still possible that undulation contributes to stability in the roll and yaw directions. This hypothesis is supported by the following line of reasoning: To be able to produce control moments, the snake assumes the S-shaped posture, which is bilaterally asymmetric at any moment of time. As a result, unfavorable nonzero moments are produced even in the absence of disturbances. However, the average body posture over one undulation cycle is symmetric. The symmetric averaged posture causes the moments about the fore-aft axis to periodically vary with relatively small magnitudes about zero means. If the average moments were nonzero, this would drive the snake's body to rotate, potentially causing it to spin out of control. By contrast, under certain conditions that depend on the relative timescales of the motions, zero-mean periodic moments would cause the snake to wobble moderately about the upright position without losing control.

Flying snakes are not the only systems exploiting such properties of periodic motions. In fact, there exists a whole branch of the control theory, named vibrational control, which deals with similar exploitations in mechanical systems. A systematic insight into the mechanics of snake flight can be gleaned by the methods that vibrational control offer to produce desirable changes in the dynamic response and properties of nonlinear mechanical systems via high-frequency zero-mean periodic inputs (Meerkov, 1980). Applying periodic inputs in a mechanical system may change the stability properties, natural frequencies, transient response, and equilibria of the system (Thomsen, 2005). The simplest and most well-known example is the Stephenson-Kapitza pendulum (Kapitza, 1951), a simple inverted pendulum with a pivot free to move along the vertical line. By vibrating the pivot vertically with sufficiently high frequency, the unstable upward position of the pendulum can be stabilized without using feedback control.

Employing periodic inputs to control mechanical systems generally gives rise to periodic steady-state motions that are not easy to find and characterize. Nevertheless, for a large class of time-periodic mechanical systems, the averaging theorem provides a powerful tool to predict the existence and determine the stability of periodic solutions (Guckenheimer and Holmes, 2013, Bullo, 2002). Physically speaking, when the inputs oscillate much more rapidly than the natural dynamics of the system, the state of the system can be approximated to remain the same during one input cycle. The averaging theorem averages the dynamics over one input cycle and introduces a time-invariant (or autonomous) system that approximately has the same trajectory and stability characteristics as the original time-periodic system. In vibrational control, the

approach is usually to use the averaging theorem to replace the original time-periodic dynamics with the averaged time-invariant system. Next, the averaged system is designed to possess a desirable stable equilibrium solution, about which the time-periodic system is ensured to have a stable periodic orbit. The required inputs are then found according to the aforementioned design. With this technique, the control is open loop, and the desired motion is achieved without any feedback from the state of the system. It is imperative to note here that the necessary condition for the averaging theorem to be valid is that the frequency of inputs must be larger than a certain amount, which depends on the physical parameters of the system. However, the minimum required frequency cannot be determined from the averaging theorem itself. In practice, a trial and error approach is usually used to select the input frequency that makes the stabilization work (Tahmasian and Woolsey, 2015).

Averaging techniques have found widespread applications in stabilization and control of biomimetic systems incluing robotic fish (Morgansen et al., 2002), flapping wing micro-air vehicles (Tahmasian et al., 2014), and snake robots (Liljebäck et al., 2010). Averaging techniques have also been used to analyze the dynamics of biological systems such as flying insects (Taha et al., 2015).

In this work, we treat flying snakes as nonlinear mechanical systems, with undulation as a zero-mean periodic input. According to vibrational control, it might be possible that a snake undulates to take advantage of the properties of periodic motions and obtain some degree of passive stability. We examine this hypothesis using a theoretical approach by representing the snake as a chain of successively linked airfoils to develop a dynamical framework for the 3D motions. Within this framework, the snake's postural reconfigurations can be approximated by properly changing orientations of the airfoils. Using joint torques as the control inputs makes it possible to adjust the complexity of the model to the control requirements. This formalism enables us to examine the influence of changing the number of links, as well as the amplitude and frequency of the periodic inputs, on the stability characteristics of the model. In this regard, we determine the minimum number of links and the minimum frequency necessary to stabilize the model. Moreover, we test the hypothesis that snakes need to undulate to maintain their flight stability.

This study helps us understand the fundamental control mechanisms that snakes employ during a glide. We determine the minimum functional requirements for the stability of snake

gliding; therefore, our findings could provide insight into the evolutionary transitions that have led to such a unique behavior. Furthermore, by studying the gliding behavior of snakes, it may be possible to learn a novel method of implementing vibrational control in a flying air or water vehicle. Finally, the dynamical framework we develop allows us to explore theoretically possible but biologically unrealized motions, and to exploit the underlying principles to engineer biologically inspired robotic analogues to snakes.

2. Methods

In this study, we model the snakes using a chain of n rigid links connected by revolute or spherical joints (n-chain), producing an articulated snake-like system. This model has been widely used to study and reproduce the 2D terrestrial motion of snakes (e.g., Hirose and Morishima, 1990, Prautsch and Mita, 1999, Maladen et al., 2011, Dowling, 1999, Saito et al., 2002, Mori and Hirose, 2002, Chernousko, 2005, Enner et al., 2012). Here, we modify this model to consider the 3D motion of snakes through air. In this study, we use a theoretical multibody model, which consists of a chain of n airfoils connected by $n-1$ revolute joints. The axes of the joints are assumed to be parallel, so that the shape of the n-chain model remains planar while it translates and rotates in 3D as a whole. Ignoring the out-of-plane motions is in accordance with experimental kinematic data (Socha et al., 2010), which showed that the total displacements of several landmarks on the snake's body, perpendicular to the 'mean' orientation, were small compared to the snout-vent length. This same justification was used in (Jafari et al., 2014) to develop 2D models of flying snakes. We consider our model links to be identical, with uniform mass distribution and the cross-sectional geometry of the snake-like airfoils (Socha, 2011, Holden et al., 2014). The mass and length of each airfoil are adjusted, such that the total mass and length of the model match those of the real snake. To drive the model and control the trajectory, actuators that produce the required torques are considered at each joint (Fig. 1A).

The configuration space of the n-chain in 3D space has a geometric decomposition into the internal shape variables, called the shape space S, and the rotational and translational group motion of the system as a whole, which is the special Euclidean group in 3D, $G = SE(3)$. Elements of G consist of $\vec{r} \in \Re^3$, the position of the 'head' (point O in Fig. 1), and $R \in SO(3)$, the relative orientation matrix of the body-fixed frame *x-y-z* with respect to the inertial

coordinate system *X*-*Y*-*Z*. The shape space $S = S_2^1 \times \cdots \times S_n^1$, whose elements are $\vec{\Theta} = \{\theta_2, \ldots, \theta_n\}$, is the product of $n-1$ circles, with S_i^1 comprising the relative orientation of the i^{th} segment with respect to the first segment, θ_i. The shape variables completely determine the articulated body's shape by describing the relative orientation of the connected links. The configuration of the n-chain can be fully described by an element in the direct product $G \times S$.

This decomposition of the configuration space neatly clarifies the dynamical analysis of the n-chain: to find the stability characteristics of the n-chain, it is sufficient to determine how the model is reoriented in 3D by motions in the shape space, which are associated with postural reconfigurations of the snakes. In particular, undulation is represented by closed cycles in S, whereas flight stability concerns stability of invariant sets (less precisely, steady-state solutions) in G only. Because flying snakes remain stable with the notion that they do not topple or experience excessively high roll and pitch angles, we ignore the translations of the model in its stability analysis and consider the rotational stability only.

2.1. Modeling of forces

To develop the equations of motion, the aerodynamic forces on each of the airfoils must be resolved in terms of its orientation and velocities. A well-established approach to account for the variation of velocities along the wing axis due to its angular velocity is the blade element method (Ellington, 1984). We employed this method by finding the forces acting on thin strips using the local velocities, and summing up these forces to find the net force and moment acting on the airfoil. To calculate the local forces, we followed (Jafari et al., 2014) to ignore any aerodynamic interaction between the airfoils, and to use the steady lift and drag coefficients for the snake airfoil determined by (Holden et al., 2014). These coefficients had to be first adjusted for the sweep angle that the airfoil makes with the airflow (Fig. 2). A simple but useful theory, introduced by Jones (1947), relates the aerodynamic performance of a swept wing to that of a reference configuration where the wing is perpendicular to the airflow. Despite being simple, this theory has been verified to be in satisfactory agreement with experimental results, particularly at high Reynolds numbers ($\text{Re} > 10^5$) and for sweep angles up to 60° (e.g., Boltz et al., 1960). The basic assumption in simple sweep theory is that only the normal component of the airspeed

contributes to producing forces (Schlichting and Truckenbrodt, 1979). As a result, the magnitude of the aerodynamic forces F_λ at the sweep angle λ can be obtained as

$$F_\lambda = F_\perp \cos^2 \lambda \tag{1}$$

In the above equation, $F_\perp$ is the aerodynamic force with the assumption of zero sweep angle.

We used Eq. 1 to find the local normal forces; we also neglected any force components along the airfoil span axis.

2.2. Equations of motion

To specify the orientation of the model in three dimensions, we use the rotation matrix R, which represents the rotation from the inertial frame to the body frame fixed to the first link. We chose to determine the elements of R in terms of the 3-2-1 Euler angles, with the rotation angles χ, ψ and ϕ about *z*-, *y*- and *x*-axes, respectively.

To explicitly write the equations of motion for arbitrary n, we selected the velocities expressed in the body-fixed frame *x*-*y*-*z* (commonly called the quasi-velocities) as the variables, and summed the Newton-Euler equations over all of the segments to obtain the dynamic equations in G. The dynamic equations in S were derived by writing the moment equation about each joint axis. This approach was identical to using Kane's method (Kane and Levinson, 1985). The equations of motion were compiled in the following compact form:

$$M\left(\vec{\Theta}\right)\begin{Bmatrix} \dot{\vec{v}} \\ \dot{\vec{\omega}} \\ \ddot{\vec{\Theta}} \end{Bmatrix} = \vec{f}\left(\phi,\psi,\vec{v},\vec{\omega},\vec{\Theta},\dot{\vec{\Theta}}\right) + \begin{Bmatrix} \mathbf{0} \\ \mathbf{0} \\ \vec{\tau} \end{Bmatrix} \tag{2}$$

where $\vec{v}$ is the velocity of the 'head', and $\vec{\omega}$ is the angular velocity of the body-fixed frame, with both expressed in the *x*-*y*-*z* coordinates. Matrix M contains the inertial terms and is a function of shape variables only, and $\vec{f}$ is the drift vector resulting from the gravity, the aerodynamic forces and the second-order velocity terms. Also, $\vec{\tau}$ represents the input torques exerted at the joints.

To obtain a complete set of equations describing the motion, the dynamic equations were supplemented by the following kinematic relation:

$$\frac{d}{dt}\begin{Bmatrix}\dot{\phi}\\ \dot{\psi}\\ \dot{\chi}\end{Bmatrix} = J(\phi,\psi)\vec{\omega} \tag{3}$$

where J is the Jacobian of the rotation matrix (Baruh, 1999).

2.3. Controlled motion about a fixed point

Standard methods to calculate stability in a multi-dimensional state space require obtaining an invariant set, whose stability can be determined linearly. We started analyzing the n-chain model with the simplest invariant set, a fixed point. Because neither the position vector $\vec{r}$ nor the rotation angle χ appeared in Eqs. (2) and (3), these variables were omitted from the state vector. A fixed point was therefore determined using

$$\begin{cases}\dot{\vec{v}} = \dot{\vec{\omega}} = \mathbf{0}\\ \dot{\phi} = \dot{\psi} = 0\\ \dot{\vec{\Theta}} = \ddot{\vec{\Theta}} = \mathbf{0}\end{cases} \tag{4a}$$

To ensure an upright configuration, Eq. (4a) was augmented with the following conditions:

$$\phi_e = 0 \ , \ \psi_e = 0 \tag{4b}$$

where the subscripts indicate equilibrium values.

To control the roll and pitch angles, the model requires at least two inputs, which must be supplied by the joint torques. Therefore, the simplest chain had to incorporate three links. After substituting Eqs. (4a) and (4b) into Eqs. (2) and (3), we solved for $\vec{v}_e$, $\vec{\omega}_e$, $\vec{\Theta}_e$, and $\vec{\tau}_e$, in which the subscript denotes the values at the fixed point solution, $\vec{x}_e$. Next, we linearized the nonlinear equations of motion about the fixed point to obtain the local state-space time-invariant form. We then used the linear quadratic regulator (LQR), a well-known feedback control scheme, to stabilize the fixed point solution (Sontag, 1998). As a result, the joint torques were determined as:

$$\vec{\tau} = \vec{\tau}_e - K\left(\vec{x} - \vec{x}_e\right) \tag{5}$$

with $\vec{x}$ being the system state, and K some constant gain matrix determined by the LQR. Although the stabilization rendered by Eq. (5) was obtained for the locally linearized system, it

tended to work within a fair neighborhood of the fixed point due to the robustness of the LQR.

The above procedure was repeated for a 4-link model. The extra degree of freedom made it possible to control $\dot{\chi}$ in addition to the conditions expressed in Eqs. (4a) and (4b). To this end, we replaced the second line of Eq. (4a) with $\vec{\omega} = \mathbf{0}$.

One interesting result arising from the addition of vibrational control is the fact that employing periodic inputs could modify the properties of a mechanical system. To examine the influence of periodicity on the stabilizing properties of the designed feedback control, we revised Eq. (5) to incorporate a periodic term as

$$\vec{\tau} = \vec{\tau}_e - K\left(\vec{x} - \vec{x}_e\right) + \alpha_u \vec{h} \sin \Omega_u t \tag{6}$$

where Ω_u is the input frequency, $\vec{h}$ is a constant vector, and α_u is a scalar parameter determining the amplitude of input vibrations.

The procedure described above can likewise be used to control other motions such as yaw and sideslip, as long as the number of input torques in the n-chain is equal or greater than the number of coordinates that are desired to be controlled.

2.4. Motion with undulation

To reproduce shape changes in the n-chain that resemble undulatory waves, we employed a sinusoidal wave of varying θ_i s traveling posteriorly, with the entire model comprising one wavelength. Such a wave was mathematically written as:

$$\theta_j(t) = \frac{\pi}{2} \cos\left(2\pi \frac{j}{n} - \Omega_u t\right), \quad j = 2, \ldots, n \tag{7}$$

By differentiating Eq. (7) and substituting the results into Eq. (2), the rate of translation and rotation of the model, as well as the joint torques, could be determined. However, at this point, we were mostly interested in the passive stability that undulation could possibly provide, without considering the required control effort. Therefore, to eliminate the torques from the calculations, we rewrote the whole-body equations of motion as:

$$M_{11} \begin{Bmatrix} \dot{\vec{v}} \\ \dot{\vec{\omega}} \end{Bmatrix} = \vec{f}_1 - M_{12} \ddot{\Theta} \tag{8}$$

in which M_{11}, M_{12}, and $\vec{f}_1$ are proper partitions of M and $\vec{f}$, and $\ddot{\vec{\Theta}}$ aptly takes the role of control inputs. It is also evident from Eq. (7) that

$$\ddot{\vec{\Theta}} = -\Omega_u^2 \vec{\Theta} \tag{9}$$

We combine Eqs. (8) and (9) to obtain the equations of motion in the following form:

$$\begin{Bmatrix} \dot{\vec{v}} \\ \dot{\vec{\omega}} \end{Bmatrix} = M_{11}^{-1}\left(\vec{f}_1 + \Omega_u^2 M_{12}\vec{\Theta}(t)\right) \tag{10}$$

in which the periodicity of the input is emphasized by the explicit dependence of the shape variables on time.

2.5. Simulations

We developed custom-written programs in MATLAB (version 2014a) to integrate the equations of motion using the Dormand-Prince method (Dormand and Prince, 1980). We also used built-in MATLAB functions to find the fixed-point solutions of section 2.3 to design the LQR feedback matrix. Among the several solutions that we found for the fixed-point, we carried out the simulations with the one having the farthest dominant pole from the origin.

In spite of the effectiveness of the LQR, because it was based on local linearization of the system, there was a limit for the initial deviation before stabilization fails. Hence, it would make sense to measure effectiveness of the stabilization and the influence from the periodic input in terms of the size of the basin of stability. Here, we defined stability as not being too deflected from the upright configuration, so it would be reasonable to consider the basin of stability only in the $\phi - \psi$ plane, instead of the whole state space. For the same reason, vector $\vec{h}$ in Eq. (6) was chosen to be the summation of the columns in the gain matrix K of the LQR associated with ϕ and ψ (see Eq. (5)). To determine the basin of stability, we discretized the $\phi - \psi$ plane, and carried out simulations with initial conditions selected from the discrete points one by one. Based on the observed snake undulation data (Socha et al., 2005, Jafari et al., 2014), the frequency of the periodic inputs was selected to be 1.4 Hz in the simulations, unless specified.

Because the rotation angles ϕ, ψ and χ describe the orientation of the first link, not the 'average' body orientation, little physical sense can be made of the results for the body

orientation when presented in terms of these angles. This issue was resolved by introducing the x'-y'-z' coordinate frame, with the z' axis being parallel to the z axis, and the x' axis determined such that the center of mass velocity, v_G, lies in the x'-z' plane (Fig. 1B). We defined the roll, pitch, and yaw angles as the consecutive rotation angles that would transform the inertial frame into the x'-y'-z' frame.

3. Results

Fig. 3 shows the fixed-point solutions of the chain model with three and four links that were obtained as outlined in section 2.3, along with the trajectories of the orientation angles and the center of mass (CoM) velocities. In Figs. 3A and 3B, the shape of the model and the in-plane component of the fixed-point velocities are plotted. Although the velocity vector is shown at the 'head' point, it is clear that any point of the model has the same velocity. As the fixed-point solutions were found subject to Eq. (4b), the axis of gravity is perpendicular to the x-y plane. The solutions for $n = 3$ and $n = 4$ were generally similar, with a C-shape in which the airfoils made moderate sweep angles with the velocity direction. Examining the numerical values revealed that (i) in both solutions, every airfoil made the same angle with the velocity vector, and (ii) v_y and v_z were the same in both solutions, meaning that the angle of attack was also the same and equal to $\alpha = 27.4°$ for all of the airfoils. As a result, equilibrium in the vertical direction becomes trivial: with the same angle of attack and normal velocity, both models produced the same amount of lift force to cancel the same weight.

Figs. 3C to 3F prove the success of the LQR in stabilizing the fixed point by showing that the trajectories starting from an initial point somewhat away from the fixed point converged to it. The initial deviation for the plotted trajectories were $\phi_i = 30°$, $\psi_i = 40°$ with the subscripts denoting the initial conditions, and a 2% deviation in the velocity. Note that the roll, pitch and yaw angles plotted in Figs. 3C and 3D are calculated based on the x'-y'-z' coordinate frame (Fig. 1B), and their initial values are not necessarily equal to ϕ_i and ψ_i. Figs. 3C to 3F also show the effect of the periodic term in Eq. (6), which made the trajectories starting from the same initial state converge to oscillating about the fixed-point solution without becoming unstable. However, the periodic input caused the yaw angle to deviate from the equilibrium value and start to

decrease or increase with time. This happened owing to the existence of the variable χ, which became the same as the yaw angle at the fixed point, where $\phi = \psi = 0$. We had no control authority on χ because it was cyclic (i.e., it did not appear in the equations of motion) and unactuated. Although there exist methods to control systems having unactuated cyclic variables (e.g., Grizzle et al., 2005), we did not employ them here because our primary goal was to control the roll and pitch motions.

Fig. 4 depicts the basin of stability in the $\phi - \psi$ plane with colors representing the minimum amplitude of the periodic input, α_u (see Eq. (6)), required to have a stable trajectory. The amplitudes are normalized with respect to the maximum value used for the simulations. Although the maximum amplitude for $n = 3$ and $n = 4$ were different, they were selected such that they resulted in the same control effort, defined as the average torque at the joints (see Appendix A2). The initial deviations from the fixed point solutions were ϕ_i and ψ_i, in addition to a 2% deviation in the velocity. No data exists for the roll and pitch angles in actual snake flight, but (Socha et al., 2005) reported glide angles up to 60°, based on which we considered the maximum ϕ_i and ψ_i deviation to be 60°. We defined a trajectory to have not diverged, if neither ϕ nor ψ reached 80° during a 15 s simulation, which was long enough for any instabilities to be manifested. It should be noted that the basin of stability is plotted only in the first quadrant because it is symmetric about the ϕ and ψ axes. It is evident from Fig. 4 that the LQR could provide stability only for a finite portion of the shown space. When the initial angles went far away from the fixed-point solution, the stabilization by the LQR alone failed, but the trajectories could be stabilized with the addition of a periodic term to the control input. In the three-link model, ϕ_i mainly determined whether the LQR alone was sufficient for stability, and $\phi_i = 40°$ was the approximate border for the periodic inputs being required for stability. The four-link model had a more complex behavior, with both ϕ_i and ψ_i playing roles to determine where the LQR alone stabilized the trajectories. Also, stabilization of the trajectories with farther initial conditions generally required larger amplitudes of the periodic input. However, this method could not be used without limits either, as the empty regions in Fig. 4 show those initial conditions for which no stable trajectories could be found. Nevertheless, by adding a periodic term to the control input, we could significantly expand the basin of stability, particularly for $n = 3$.

Next, we explored how the amplitude and frequency of the input influenced its stabilizing properties. Fig. 5 shows how different periodic input amplitudes caused the trajectories starting from various ϕ_i and ψ_i to converge to the fixed-point (green regions) or become unstable (orange regions). As before, a trajectory was considered unstable if either ϕ or ψ reached 80° during a 15 s simulation. Note that the regions shown in Fig. 5 are not plotted in the $\phi - \psi$ plane and should not be confused with the basin of stability. Figs. 5A to 5D summarize the results for $n = 3$ and indicate that for the majority of the simulated initial conditions, there existed a range for the amplitude of the input, within which the trajectories remained stable. In addition, as could be expected, the stable region became smaller as ϕ_i increased, because the initial conditions moved farther from the fixed-point solution. Figs. 5E to 5F summarize the results for $n = 4$ and show a more complicated behavior, with some trajectories becoming stable and unstable, and sometimes stable again, as the input amplitude increased from zero to the maximum value. Moreover, there exist 'islands' of stable and unstable parameter sets within the unstable and stable regions, respectively. Nonetheless, proper periodic inputs could be employed to stabilize many of the trajectories for which the LQR failed, also for $n = 4$. Such trajectories are identified as parts of the horizontal axes that are borders of the orange regions.

Fig. 6 encapsulates the effects of the input frequency on the size of the basin of stability. The figure shows the percentage of the $\phi_i - \psi_i$ space that could be stabilized using the LQR and the periodic term with any amplitude. The input frequency range, $\Omega_u = 1$ to 2.2 Hz, was selected to match the range observed in actual snake flight (Socha et al., 2005). It is evident from Fig. 6 that for the three-link model, the basin of stability was the largest with the input frequency within the range 1.4-1.6 Hz, whereas $\Omega_u = 1.8$ Hz resulted in a moderate size of the basin of stability, and the other cases were even inferior. Therefore, an optimal range for the input frequency existed where the basin of stability became the largest; outside of this optimal range, the basin of stability shrank rapidly. However, the four-link model exhibited a different behavior, in which the size of the basin of stability gradually increased with frequency from ~70% to ~95% of the total variable space. Although a local maximum existed at $\Omega_u = 1.6$ Hz, it was insignificant and did not imply an optimum value.

The detailed effects of the input frequency are reflected in Fig. 7, where the curves are plotted for several input frequencies and show the minimum values of the input amplitude

required to stabilize the trajectories. Where the curves do not continue, no input could be found for stabilization, so the basin of stability was larger where the curves spanned a bigger fraction of the plot domain. It is clear from the figure that frequency had nonuniform effects on different parts of the parameter space. For instance, the curves might become discontinuous at their left or right ends (e.g. compare the $\phi_i = 60°$ curves in Figs. 7D and 7E), or in the middle (e.g. compare the $\phi_i = 50°$ curves in Figs. 7A and 7B). Figs. 7F to 7J reveal that the basin of stability spanned the entire range of ψ_i at $\phi_i \leq 50°$, whereas the shape of the basin of stability at $\phi_i \geq 55°$ changed drastically with frequency; but those large changes had limited influence on the size of the basin of stability (Fig. 6).

Next, we considered the passive dynamics of the n-chain with high-amplitude undulation (Eqs. (7) and (10)), and used the previously mentioned criterion to track whether they lost stability for a range of frequencies and link numbers. The results are depicted in Fig. 8A, where the orange region indicates the set of frequencies and link numbers that made the model become unstable, and the green region contains the set of parameters that resulted in passively stable trajectories. The figure verifies that undulation could provide passive stability for the chain model for several frequencies and link numbers. Apart from the scattered green islands, the bulk of the stabilizing parameters were within the region to the upper right corner of the plot, where both the frequency and the number of links were the largest. This bulk region was separated from the rest of the plot by a borderline, which could be described as undulation frequency being a function of the number of links, $\Omega_u = f(n)$, where frequency generally decreased with the number of links. The most important inference drawn from Fig. 8A is that for any specific number of links, there existed a minimum frequency of undulation, above which passive stability was obtained. Although the figure suggests that the bulk green region did not extend below $n = 12$, because we have not examined larger frequencies, it would not be prudent to make deductions about the existence of a minimum number of links for passive stability to be possible.

Fig. 8B shows the orientation angles of the model for $\Omega_u = 1.6$ Hz and $n = 20$. This simulation started from an upright configuration, 8 m/s forward velocity, and 3 m/s sinking velocity. It is observed that the roll angle increased from zero to about 25° and then back to zero in about 5 seconds. The roll angle continued to oscillate about zero for the rest of the time. The pitch angle increased from zero to about 50° in 5 seconds, and then started to gradually go back

to zero. The yaw angle started to oscillate about approximately -90° after reaching this value. The large deviation of the yaw angle should not be interpreted as a sign of instability, as the stability criterion in this work concerns remaining upright, but not directional control. Fig. 8C shows the rates of roll and pitch angles, which indicate they continued to oscillate about zero without diverging. It is observed from Fig. 8D, which shows the forward and sinking speeds, that while the forward speed varied limitedly during the simulation time, the sinking speed first decreased from -3 m/s to about -10 m/s and then returned to approximately its initial value. All in all, at the end of the simulation, every variable that appeared in the equations of motion went back to approximately its initial value. Therefore, it is expected that the model would continue to remain stable no matter how long simulation lasts. Note that yaw, which deviates from its initial value, is closely related to the angle χ, and has no effect on the model dynamics.

4. Discussion

4.1. Glide simulations

The results of this work prove the effectiveness of using periodic inputs to stabilize gliding trajectories of the n-chain as measured by the size of the basin of stability. The results are important from the point of view that the periodic part of the input is not determined from the feedback, therefore the periodic input can contribute to the trajectory stability at any point in the state space, meaning that the stabilizing properties of the periodic inputs used in the model are quite general. The only requirement for the stabilizing effectiveness of the periodic input is that the amplitude and frequency have to be properly tuned (Figs. 5 and 7). Moreover, the basins of stability for the three-link and four-link models are not similar, indicating that the stabilization is dependent on the model's number of links.

An interesting consequence of adding the periodic term to the control input was that it caused the model to rotate in the yaw direction with an averaged constant rate, whereas the yaw angle would asymptotically converge to some constant value in the absence of the periodic input. As explained earlier, the reason for this behavior is that angle χ, which becomes the same as the yaw angle at the fixed point, is cyclic and unactuated; therefore, it is not controllable and is expected to be influenced by any perturbation including the periodic inputs. As a result, the

model lacks directional control and disturbances change its direction of motion. On the other hand, the effect of the periodic input on the yaw angle is predictable and constant in average, making it possible for the periodic inputs to be used as a simple means to 'drive' the model in the yaw direction. Upon reaching the desired direction, the periodic inputs are 'turned off', after which all variables including the yaw rate will dissipate and go to zero, and the system proceeds with the new direction.

The periodic motions in the controlled glide simulations are small-amplitude compared to undulation in flying snakes; they cause the model to wobble about the fixed-point shape, which is asymmetrical about any axis (Fig. 3). By contrast, high-amplitude undulation waves render averaged symmetry about the fore-aft axis, which is expected to minimize the control demand. In addition, according to the theory of vibrational control, undulation is a zero-mean periodic input to the system and may be able to provide open-loop stability. The simulations of the passive dynamics of the model with high-amplitude undulation confirm that it could indeed provide stability without any control. Our results are also in accordance with the averaging theorem, as they indicate that passive stability is obtained for any undulation frequency above a certain value. The minimum required frequency is a generally decreasing function of the number of links, which suggests that a lager number of links, or equivalently smoother shape changes, helps to obtain passive stability. Moreover, because power consumption is proportional to the square of frequency, with a larger number of links, stability is obtained at lower energy cost.

Fig. 8A shows that some low-frequency undulatory motions can also lead to passive stability, even at zero frequency ($n = 6$). However, these low-frequency motions are scattered and separate from the compact set of high-frequency parameters. Such scattered parameters could not be predicted by the averaging theorem, but they have been studied in some simple mechanical systems (Berg and Wickramasinghe, 2015). Fig. 8A also suggests that a minimum number of links is needed to obtain passive stability with undulatory motions. Testing this hypothesis requires analyzing the model at higher frequencies, which was not done in this work. However, it is noteworthy that some other mechanical systems, namely boomerangs, are made of as few as two rigidly connected airfoils and fly through the air with near zero rates of roll and pitch, but they use high spin rates instead of shape reconfigurations.

Finally, although we used a single snake data for the simulations, the results obtained here are generally valid. The only snake-specific parameters are the model's mass and total

length, which do not change the form of Eq. (2), but merely scale the velocities, frequencies and input torques. More importantly, because the angles are nondimensional variables, the fixed-point shapes and the basins of stability remain unchanged.

4.2. Implications about gliding snakes

Our first hypothesis about why airborne snakes undulate was that undulation is a necessary condition for stable gliding. The results obtained from the controlled glide simulations negate the hypothesis, as we found stabilizable fixed points in the state space, to which the trajectories converged asymptotically. Our analysis shows that stable trajectories could be obtained with a minimum number of three airfoils in the model. Therefore, it is theoretically possible for the airborne snakes to hold a static posture and glide, provided that the snakes have sufficient postural control to dissipate disturbances. For instance, fine locomotor control executed independently along the snake body as prescribed by the LQR can maintain stability. This control strategy needs accurate feedback from the state variables including velocities, orientation angles and their rates, and shape angles and their rates. However, the neural and musculoskeletal systems of the snakes might not be sufficient to accomplish such a complex task. Particularly, this issue could hinder the early stages of the evolution of the gliding behavior, when the required traits had not been developed yet. By contrast, the simulations suggest that snakes could use large-amplitude undulation to obtain some degree of open-loop stability, and become less dependent on the feedback and active control. Of course, the passive stability of the simulated trajectories is presumably a result of several idealizations in the modeling; nevertheless, the closed-loop control can be formed about the ideally passively stable trajectories and therefore be less demanding. A very similar deduction was made in (Jafari et al., 2014), where a model with some idealizations resulted in passively stable trajectories, but a more realistic model required active control.

The properties of the chain model can also explain how the snakes obtain an agile aerial performance despite lacking specialized flight surfaces. The closed-loop control can be applied to stabilize not only the roll and pitch motions as exemplified by our simulations, but also other motions such as yaw and sideslip. These control strategies are force-based (i.e., the shape changes are used to alter the aerodynamic forces and achieve the desired motion) and work as

long as a sufficient number of links in the n-chain is considered. If the chain model has more links than necessary, the redundant control inputs conduce to larger reachable and controllable sets (Sontag, 1998) within the state space, which translate into the complicated tasks that cannot be performed by the system with the minimum number of links. Having well above a hundred vertebrae, the snakes are able to perform several maneuvers in this way. Additionally, the snakes can implement inertial reorientation by exploiting shape changes to rotate in 3D irrespective of the aerodynamic forces. In this regard, the induced rotation is similar to the righting of lizards using tail inertia (Jusufi et al., 2010) and certain bat maneuvers using wing inertia (Bergou et al., 2015). With inertial reorientation, the snakes can perform maneuvers that are not observed in other gliders, such as surprisingly sharp turning at low speeds and turning without banking (Socha, 2002). Therefore, it is suggested that the snakes can accomplish multiple maneuvers because of their unrestrained ability for postural changing, which is enabled by their ample musculoskeletal design. In other words, in the case of gliding by snakes, a seemingly inept body design turns out to be a versatile asset, which facilitates unexpected functionalities.

Before closing this section, the interested reader who wishes to learn more details on the physical basis of inertial reorientation is referred to consult the literature on the geometric phase of holonomic and nonholonomic systems (e.g. Bloch et al., 2005, Koon and Marsden, 1997).

4.3. Modeling limitations

The theoretical analysis made in this work entails the following limitations, which are related to the model assumptions:

- Despite our scarce knowledge about the aerodynamic interaction between the fore and the aft body (Miklasz et al., 2010), it is reasonable to speculate that the flow structures created upstream are intercepted by the downstream parts, producing some aerodynamic coupling. Because no data is available in this regard, as a first-order approximation, each model link was assumed aerodynamically uncoupled from the links before and after. Moreover, we neglected aerodynamic end effects, such as tip-vortices or effects due to the low aspect ratio of the airfoils. However, owing to the robustness of the model stabilizations, we expect to attain no major difference in the main results by incorporating the influence from the mentioned aerodynamic effects in the model.

- The model assumes that the links are uniform, whereas the real snake displays varying morphology along the body length. In particular, the width is non-uniform, being maximal at mid-body and tapering toward the tail, and the cross-sectional shape may not be constant. However, these variations are insignificant, and the link shape is close enough to the real snake to be sufficient for a first-order model.
- The model structure was not sufficient to simulate the beginning part of the snake glide, when the speeds are small and the undulating configuration is not formed yet. In practice, any simulation starting from small initial velocities would result in instability; the stable trajectories could be obtained only with sufficiently large initial velocities. As discussed in (Jafari et al., 2014), this part of the glide involves kinematics that have not been quantified and are likely to produce different aerodynamic forces than those in the developed phase of the glide.

4.4. Conclusion

In this study, we set out to understand the role of undulation in the dynamics of snake flight using theoretical modeling. We simulated trajectories of the n-chain model about its biomechanically relevant fixed-point solutions for $n = 3$ and $n = 4$. A linearization-based stability analysis showed that the fixed-point solutions were unstable, but could be stabilized using shape variables as inputs. Although the stabilization was not accomplished globally, it was shown to be effective for a considerable portion of the state space that was relevant to the actual kinematics of snakes. Further exploration revealed that by adding small-amplitude periodic motion about the fixed-point shape, the size of the basin of stability significantly expanded. Moreover, we examined the simulations with large-amplitude undulatory motions and demonstrated that open-loop stability could be obtained with sufficiently large frequency of undulation. All in all, this study exemplified methods of maintaining stability during glide with a morphing body instead of employing symmetrically paired wings. It was also suggested that the undulation lowers the demand for a complex closed-loop control system by allowing it to be formed about an ideally passively stable trajectory.

Modification of our theoretical modeling into a more realistic representation of the flying snakes requires further exploration of their kinematics as well as understanding the full

aerodynamics of the snake's cross-sectional shape. A study is currently underway to determine the behavior of two snake-like 2D airfoils placed in tandem (Jafari et al., in preparation), but the effects of low aspect ratio, unsteady motions, and sweep angle has also to be found. Experiments with the snakes being perturbed in their developed stage of glide, or with robotic models are needed to verify our results. Upon verification, the methods of this work can be used to study several aspects of snake flight including the dynamics of turning or the effects of shape kinematics on the trajectory. Moreover, a similar approach can be applied to limbless motion through any fluid, for example with the swimming of eels (Tytell et al., 2010).

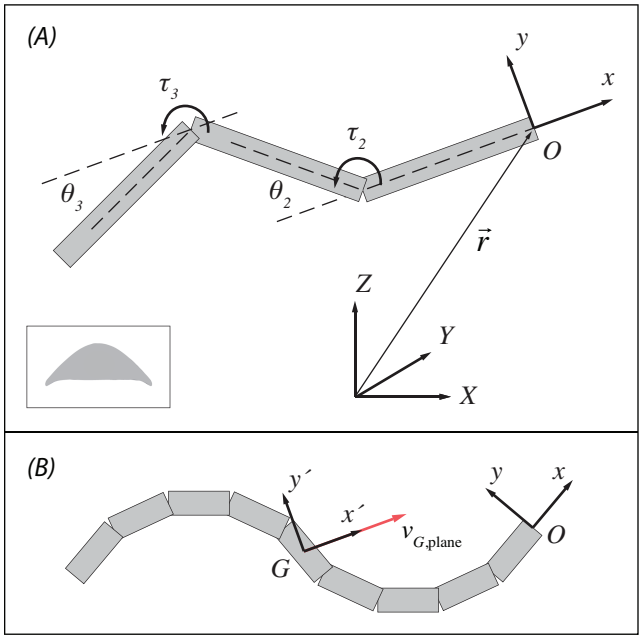

Fig. 1: Overview of the n-chain model. (A) A representative view of the n-chain model with n=3 identical links. The inset shows the snake-like cross-sectional shape of the links. The x-y-z frame is fixed to the first link, whereas the X-Y-Z coordinate system is inertial. The entire body of the model, which is viewed from the z-direction in this figure, lies in the x-y plane. The shape of the model is determined by the angle each link makes with the x-axis. The overall position and orientation of the model are determined by the position vector $\vec{r}$ and the orientation of x-y-z frame relative to the X-Y-Z frame. The joint torques represent the effort needed to change the shape of the n-chain. (B) The roll, pitch, and yaw angles are defined based on the x'-y'-z' coordinate frame, in which the z'-axis is parallel to the z-axis, and the x'-axis is determined such that the center of mass velocity, v_G, lies in the x'-z' plane. Therefore, the misleading effects caused by the rotation of the first link with respect to the average body motions do not contaminate the results.

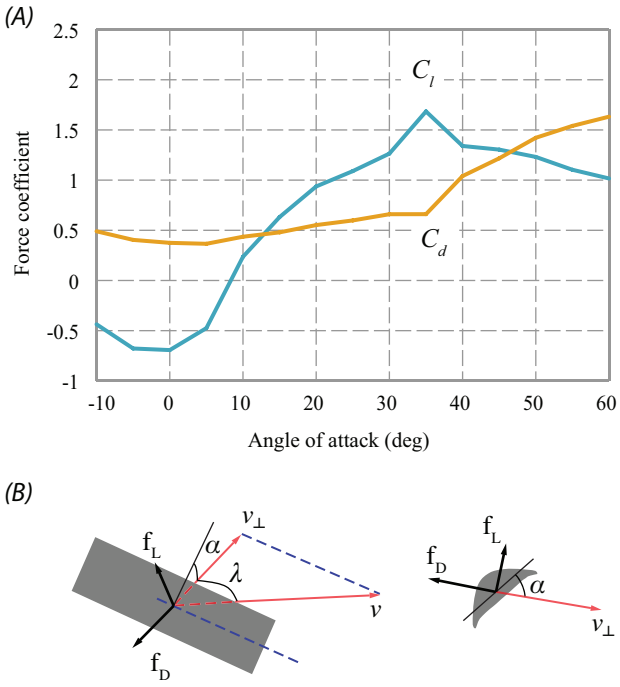

Fig. 2: Modeling of the aerodynamic forces. The local forces in the blade element method were calculated using the local velocities and the steady lift and drag coefficients for the snake airfoil (A), as determined by (Holden et al., 2014). (B) Sweep angle, λ, was accounted for by using simple sweep theory, in which only the normal component of the velocity, $v_\perp$, contributes to producing forces (left). Any force component along the airfoil span axis was neglected (right).

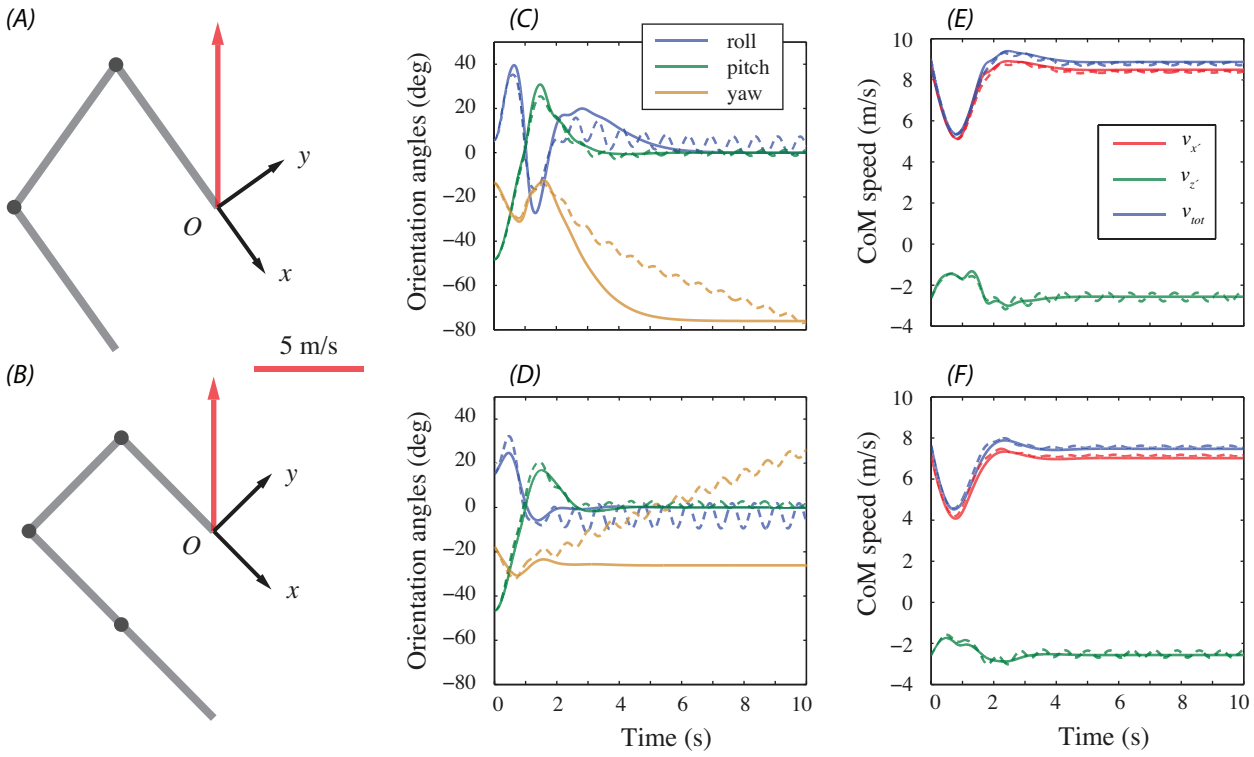

Fig. 3: The fixed-point solutions of the n-chain model with three and four links. (A-B) The model shape and the in-plane component of the fixed-point velocities. Although the velocity vector is shown at the 'head' point, every point of the model has the same velocity. The axis of gravity is perpendicular to the figure plane. Simulations for the model orientation (C-D), and CoM velocities (E-F). Using the LQR to stabilize the fixed point, the trajectories with the initial conditions of $\phi_i = 30°$, $\psi_i = 40°$, and a 2% deviation in the initial velocity converged to the fixed point (solid lines). The state variables starting from the same initial condition, but having the periodic term in their input, converged to oscillating about the fixed-point solution without becoming unstable (dashed lines). The yaw angle, which was not a state variable, and therefore was not controllable, started to decrease or increase with time when the periodic term was added to the input.

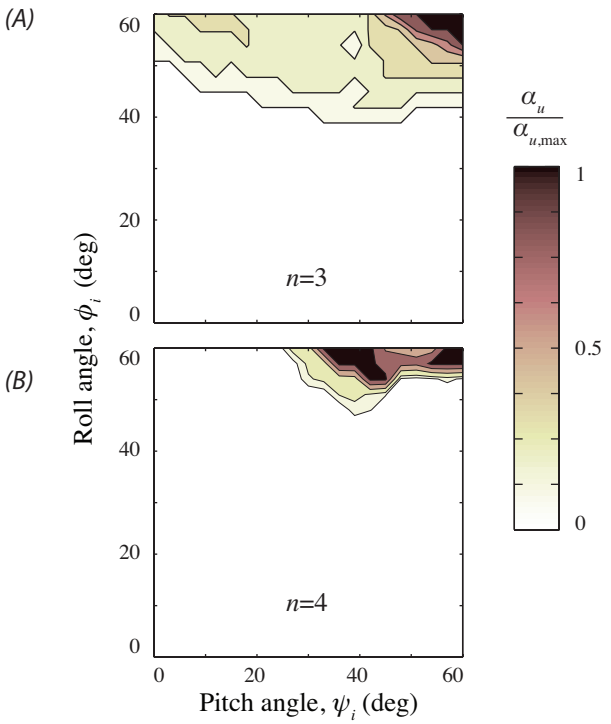

Fig. 4: The basin of stability in the $\phi - \psi$ plane. Colors represent the minimum amplitude of the periodic input, α_u, required to have a stable trajectory. The amplitudes are normalized with respect to maximum values that resulted in the same control effort for both $n = 3$ and $n = 4$. ϕ_i and ψ_i were the initial deviations from the fixed point solutions, in addition to a 2% deviation in the velocity. The basin of stability is plotted only in the first quadrant because it is symmetric about the ϕ and ψ axes. The addition of the periodic term to the input significantly expanded the size of the basin of stability by making the trajectories stable where the LQR alone failed. For the initial conditions inside the white regions, no stabilizing control input could be found.

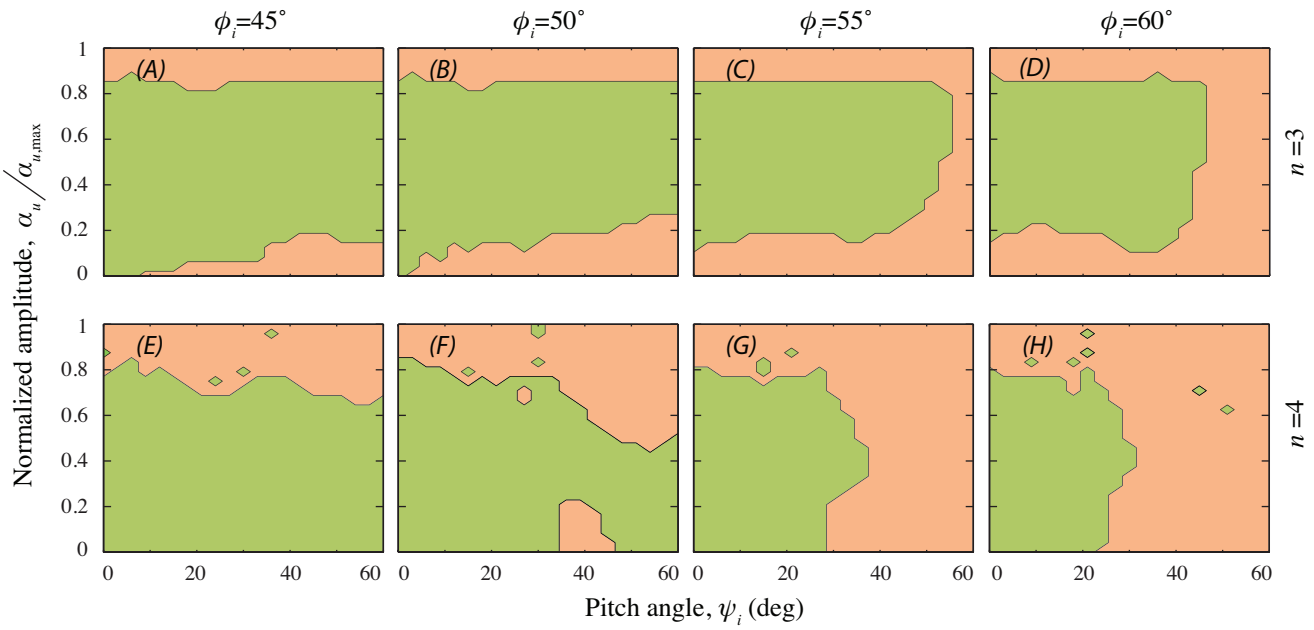

Fig. 5: The effect of the periodic input amplitude on the stabilizing properties of the input in the three-link model (A-D) and the four-link model (E-H). With the set of parameters shown in green, the trajectories converged to the fixed-point, whereas they became unstable with the parameters shown in orange. The plots do not represent the basin of stability because they are not in the $\phi - \psi$ plane. In the three-link model, for the majority of the simulated initial conditions, there existed a range for the amplitude of the input, within which the trajectories remained stable. However, in the four-link model, increasing the input amplitude could possibly change the stability properties of the trajectories with the same initial condition multiple times.

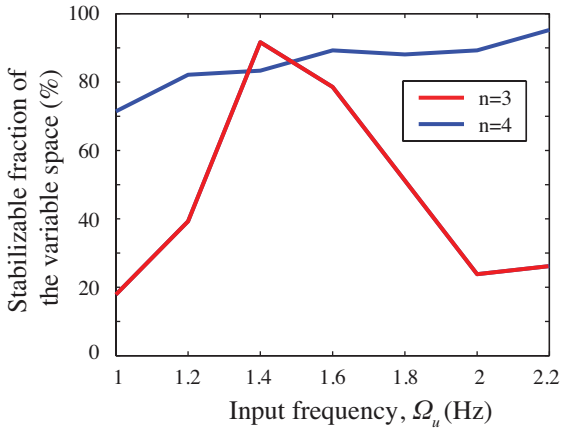

Fig. 6: The effect of undulation frequency on the total size of the basin of stability. The set all of the trajectories that could be stabilized using the LQR and the periodic term with any amplitude was highly depending on the input frequency in the three-link model. The basin of stability became the largest within the range Ω_u = 1.4-1.6 Hz, but rapidly shrank outside this optimal range. By contrast, in the four-link model, the size of the basin of stability moderately changed with input frequency, and no optimal range was observed.

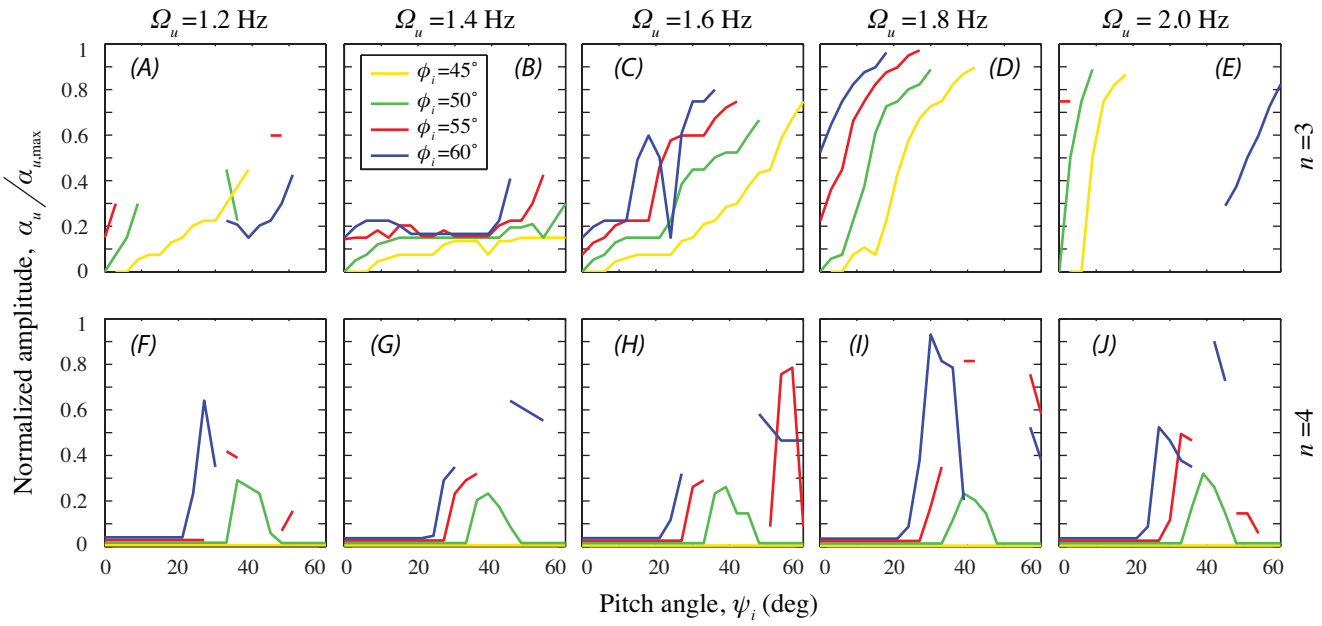

Fig. 7: The effects of input frequency on the shape of the basin of stability. The curves show the minimum values of the input amplitude required to stabilize the trajectories. Where the curves are discontinuous, no stabilizing input could be found. The shape of the basin of stability changed nonuniformly with the input frequency for both $n = 3$ and $n = 4$. The curves became discontinuous at their left or right ends ($\phi_i = 60°$ curves in D and E), or in the middle ($\phi_i = 50°$ curves in A and B). For $n = 4$, the basin of stability spanned the entire range of ψ_i at $\phi_i \leq 50°$, but became dependent on the frequency at $\phi_i \geq 55°$ (F-J).

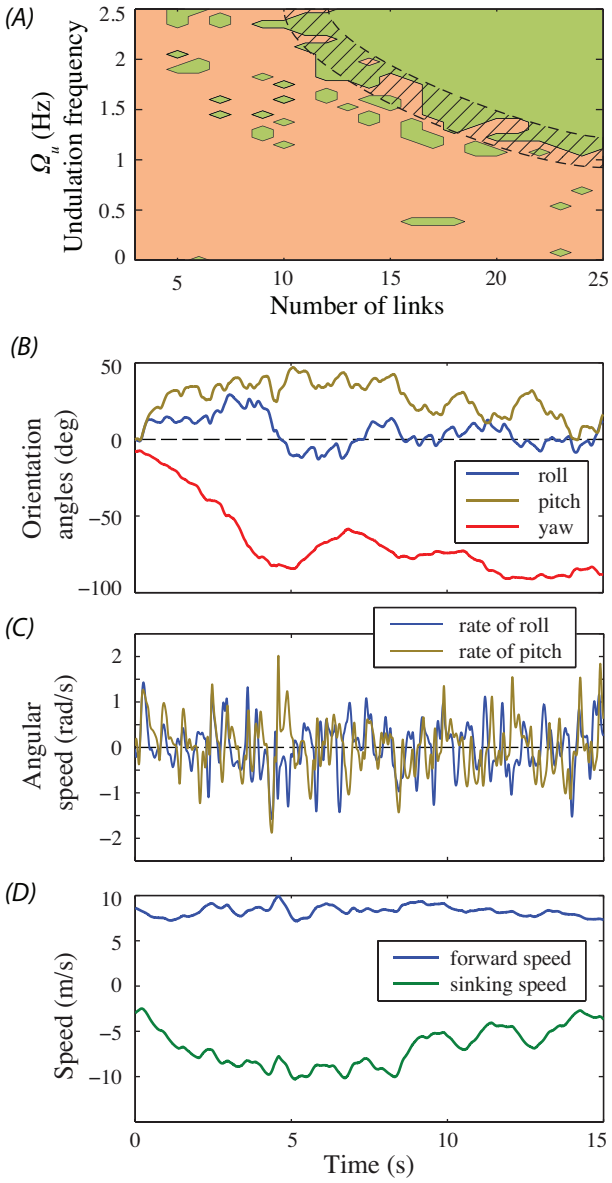

Fig. 8: The passive dynamics of the model with high-amplitude undulation (Eq. (7)), and with varying number of links and undulation frequency. (A) The green region contains the set of frequencies and link numbers that resulted in passively stable trajectories, and the orange region contains the set of parameters that made the model unstable. Within the bulk green region to the upper right corner of the figure, which is separated from the rest of the parameter space with the hatched band, undulation worked as a zero-mean input to render passive stability above a certain frequency for any link number, as the theory of vibrational control predicts. (B-D) The simulation results starting from 8 m/s forward velocity, and 3 m/s sinking velocity, with $\Omega_u = 1.6$ Hz and $n = 20$. (B) The roll and pitch angles deviated from zero and reached a maximum of ~25° and ~50°, respectively, but they returned back to oscillate about zero during the simulation time. The yaw angle exhibited a large deviation, which indicates that directional stability was not achieved. (C) The rates of the roll and pitch angles, showing that they continued to oscillate about zero. (D) Although the forward speed did not undergo large changes, the sinking speed

decreased from -3 m/s to -10 m/s, and returned back to its initial value.

References

ALEXANDER, R. M. 2003. *Principles of animal locomotion*, Princeton University Press.

BARUH, H. 1999. *Analytical dynamics*, WCB/McGraw-Hill Boston.

BERG, J. M. & WICKRAMASINGHE, I. M. 2015. Vibrational control without averaging. *Automatica,* 58**,** 72-81.

BERGOU, A. J., SWARTZ, S. M., VEJDANI, H., RISKIN, D. K., REIMNITZ, L., TAUBIN, G. & BREUER, K. S. 2015. Falling with style: bats perform complex aerial rotations by adjusting wing inertia. *PLoS Biol,* 13**,** e1002297.

BIEWENER, A. A. 2003. *Animal locomotion*, Oxford University Press.

BLOCH, A. M., MARSDEN, J. E. & ZENKOV, D. V. 2005. Nonholonomic dynamics. *Notices of the AMS,* 52**,** 320-329.

BOLTZ, F. W., KENYON, G. C. & ALLEN, C. Q. 1960. Effects of sweep angle on the boundary-layer stability characteristics of an untapered wing at low speeds. *NASA TN,* D-338.

BULLO, F. 2002. Averaging and vibrational control of mechanical systems. *SIAM Journal on Control and Optimization,* 41**,** 542-562.

CHERNOUSKO, F. L. 2005. Modelling of snake-like locomotion. *Applied Mathematics and Computation,* 164**,** 415-434.

DORMAND, J. R. & PRINCE, P. J. 1980. A family of embedded Runge-Kutta formulae. *Journal of Computational and Applied Mathematics,* 6**,** 19-26.

DOWLING, K. Limbless locomotion: learning to crawl. Robotics and Automation, 1999. Proceedings. 1999 IEEE International Conference on, 1999. IEEE, 3001-3006.

ELLINGTON, C. 1984. The aerodynamics of hovering insect flight. I. The quasi-steady analysis. *Philosophical Transactions of the Royal Society of London. B, Biological Sciences,* 305**,** 1-15.

ENNER, F., ROLLINSON, D. & CHOSET, H. Simplified motion modeling for snake robots. Robotics and Automation (ICRA), 2012 IEEE International Conference on, 2012. IEEE, 4216-4221.

GRIZZLE, J., MOOG, C. H. & CHEVALLEREAU, C. 2005. Nonlinear control of mechanical systems with an unactuated cyclic variable. *Automatic Control, IEEE Transactions on,* 50**,** 559-576.

GUCKENHEIMER, J. & HOLMES, P. 2013. *Nonlinear oscillations, dynamical systems, and bifurcations of vector fields*, Springer Science & Business Media.

HIROSE, S. & MORISHIMA, A. 1990. Design and control of a mobile robot with an articulated body. *The International Journal of Robotics Research,* 9**,** 99-114.

HOLDEN, D., SOCHA, J. J., CARDWELL, N. D. & VLACHOS, P. P. 2014. Aerodynamics of the flying snake *Chrysopelea paradisi*: how a bluff body cross-sectional shape contributes to gliding performance. *Journal of Experimental Biology,* 217**,** 382-394.

JAFARI, F., ROSS, S. D., VLACHOS, P. P. & SOCHA, J. J. 2014. A theoretical analysis of pitch stability during gliding in flying snakes. *Bioinspiration & Biomimetics,* 9**,** 025014.

JONES, R. T. 1947. *Effects of sweepback on boundary layer and separation*, National Advisory Committee for Aeronautics.

JUSUFI, A., KAWANO, D., LIBBY, T. & FULL, R. 2010. Righting and turning in mid-air using appendage inertia: reptile tails, analytical models and bio-inspired robots. *Bioinspiration & Biomimetics,* 5**,** 045001.

KANE, T. R. & LEVINSON, D. A. 1985. *Dynamics, theory and applications*, McGraw Hill.

KAPITZA, P. 1951. Dynamic stability of a pendulum with an oscillating point of suspension. *Journal of Experimental and Theoretical Physics,* 21**,** 588-597.

KOON, W. S. & MARSDEN, J. E. The geometric structure of nonholonomic mechanics. Decision and Control, 1997., Proceedings of the 36th IEEE Conference on, 1997. IEEE, 4856-4861.

LILJEBÄCK, P., PETTERSEN, K. Y., STAVDAHL, Ø. & GRAVDAHL, J. T. Stability analysis of snake robot locomotion based on averaging theory. Decision and Control (CDC), 2010 49th IEEE Conference on, 2010. IEEE, 1977-1984.

MALADEN, R. D., DING, Y., UMBANHOWAR, P. B. & GOLDMAN, D. I. 2011. Undulatory swimming in sand: experimental and simulation studies of a robotic sandfish. *The International Journal of Robotics Research,* 30**,** 793-805.

MEERKOV, S. M. 1980. Principle of vibrational control: theory and applications. *Automatic Control, IEEE Transactions on,* 25**,** 755-762.

MIKLASZ, K., LABARBERA, M., CHEN, X. & SOCHA, J. 2010. Effects of body cross-sectional shape on flying snake aerodynamics. *Experimental Mechanics,* 50**,** 1335-1348.

MORGANSEN, K. A., VELA, P. A. & BURDICK, J. W. Trajectory stabilization for a planar carangiform robot fish. Robotics and Automation, 2002. Proceedings. ICRA'02. IEEE International Conference on, 2002. IEEE, 756-762.

MORI, M. & HIROSE, S. Three-dimensional serpentine motion and lateral rolling by active cord mechanism ACM-R3. Intelligent Robots and Systems, 2002. IEEE/RSJ International Conference on, 2002. IEEE, 829-834.

PRAUTSCH, P. & MITA, T. Control and analysis of the gait of snake robots. Control Applications, 1999. Proceedings of the 1999 IEEE International Conference on, 1999. IEEE, 502-507.

SAITO, M., FUKAYA, M. & IWASAKI, T. 2002. Modeling, analysis, and synthesis of serpentine locomotion with a multilink robotic snake. *IEEE Control Systems Magazine,* 22**,** 64-81.

SCHLICHTING, H. & TRUCKENBRODT, E. 1979. *Aerodynamics of the Aeroplane, (revised)*. McGraw Hill Higher Education, New York.

SOCHA, J. J. 2002. Kinematics: Gliding flight in the paradise tree snake. *Nature,* 418**,** 603-604.

SOCHA, J. J. 2006. Becoming airborne without legs: the kinematics of take-off in a flying snake, *Chrysopelea paradisi*. *Journal of Experimental Biology,* 209**,** 3358-3369.

SOCHA, J. J. 2011. Gliding flight in Chrysopelea: turning a snake into a wing. *Integrative and Comparative Biology,* 51**,** 969-982.

SOCHA, J. J., JAFARI, F., MUNK, Y. & BYRNES, G. 2015. How animals glide: from trajectory to morphology 1. *Canadian Journal of Zoology,* 93**,** 901-924.

SOCHA, J. J. & LABARBERA, M. 2005. Effects of size and behavior on aerial performance of two species of flying snakes (*Chrysopelea*). *Journal of Experimental Biology,* 208**,** 1835-1847.

SOCHA, J. J., MIKLASZ, K., JAFARI, F. & VLACHOS, P. P. 2010. Non-equilibrium trajectory dynamics and the kinematics of gliding in a flying snake. *Bioinspiration & Biomimetics,* 5**,** 045002.

SOCHA, J. J., O'DEMPSEY, T. & LABARBERA, M. 2005. A 3-D kinematic analysis of gliding in a flying snake, *Chrysopelea paradisi*. *Journal of Experimental Biology,* 208**,** 1817-1833.

SONTAG, E. D. 1998. *Mathematical control theory: deterministic finite dimensional systems*, Springer.

TAHA, H. E., TAHMASIAN, S., WOOLSEY, C. A., NAYFEH, A. H. & HAJJ, M. R. 2015. The need for higher-order averaging in the stability analysis of hovering, flapping-wing flight. *Bioinspiration & Biomimetics,* 10**,** 016002.

TAHMASIAN, S. & WOOLSEY, C. A. 2015. A Control Design Method for Underactuated Mechanical Systems Using High-Frequency Inputs. *Journal of Dynamic Systems, Measurement, and Control,* 137**,** 071004.

TAHMASIAN, S., WOOLSEY, C. A. & TAHA, H. E. 2014. Longitudinal flight control of flapping wing micro air vehicles. *Proc. AIAA SciTech*, 203-269.

THOMSEN, J. J. 2005. Slow high-frequency effects in mechanics: problems, solutions, potentials. *International Journal of Bifurcation and Chaos,* 15, 2799-2818.

TYTELL, E. D., HSU, C.-Y., WILLIAMS, T. L., COHEN, A. H. & FAUCI, L. J. 2010. Interactions between internal forces, body stiffness, and fluid environment in a neuromechanical model of lamprey swimming. *Proceedings of the National Academy of Sciences,* 107, 19832-19837.

Chapter 4. Experimental study of the aerodynamics of snake-like airfoils in tandem configuration

Abstract

Upon becoming airborne, flying snakes flatten their body to make a roughly triangular cross-sectional shape, which enables them to produce lift and gain horizontal acceleration. In addition to flattening their body, the snakes assume an S-like posture, which makes it possible that aerodynamic interactions occur between the fore and the aft body. Such interactions have been studied experimentally; however, models with a very coarse approximation of the cross-sectional shape of snakes were used in the experiment. Moreover, the effects were measured only for the downstream model. In the present study, the aerodynamic interactions of the snake body were approximated by two-dimensional anatomically accurate airfoils placed in tandem with several snake-related configurations. The experiments were conducted in a water tunnel, and load cells were used to measure lift and drag forces produced by both airfoils simultaneously. In addition, the flow field data were obtained using digital particle image velocimetry (PIV). The results confirmed strong dependence of the aerodynamic performance on the tandem arrangement, with the lift coefficients being generally more influenced. Two sets of configurations particularly stood out; the first set included configurations close to the most probable posture of real flying snakes, and the second set showed extreme variation in the lift-to-drag ratio with slight changes in the vertical stagger. Spectral analysis showed that the upstream and downstream dominant frequencies usually locked, suggesting interactions between the downstream airfoil and the vortices shed upstream. Inspecting flow field around the airfoils revealed that the tandem arrangement modified the separated flow and the wake size. Whenever the wake vortices were formed closer to the models, they produced suction on the dorsal surface of the model resulting in lift enhancement. Moreover, the downforce created by the flow separation from the ventral surface of the models at 0° angle of attack was a function of tandem arrangement. Pressure fields were calculated to confirm the information obtained from the flow topology.

1. Introduction

Three species of snakes in the genus *Chrysopelea* found in Southeast Asia have developed the ability to glide (Socha, 2002, Socha, 2011, Socha et al., 2015). Flying snakes do not appear anatomically exceptional, and with a typical snake body, they seem to be inept for gliding. However, their aerial performance is comparable to other gliding animals (Scholey, 1986, McGuire, 1998, Socha et al., 2005). The flying snakes lack any specialized surfaces to produce the required flight forces; instead they use their entire body as a wing. Upon becoming airborne, the snake splays its ribs to transform a rounded cylindrical body to have a roughly triangular cross-sectional shape. This shape is symmetrical in the fore-aft axis with a semi-triangular dorsal surface and a concave ventral surface, which has a pair of ventrally oriented 'lips' on each lateral edge (Socha, 2011). Fig. 1A shows the mid-body profile of an airborne *C. paradisi*; although personal observations of the authors indicate slight shape variations along the body, no exact data are available for those variations. In addition to flattening their body, airborne flying snakes assume an S-like posture (Fig. 1B) and start to undulate laterally by sending traveling waves posteriorly down the body. With this dynamic behavior, different parts of the body move with respect to each other, but a staggered configuration is maintained during the shallowing part of the glide (Fig. 1C).

The gliding ability of the snakes fundamentally depends on the aerodynamics of their body shape as a peculiar wing profile. Three studies provide our current understanding of the aerodynamics of the snake's cross-sectional shape (Holden et al., 2014, Miklasz et al., 2010, Krishnan et al., 2014). As first-order approximations, all of these studies neglected the effects of undulation, 3D posture, and possible variation of the snake profile along the body, and determined the steady behavior of uniform 2D models having snake-like cross-sectional shapes. Miklasz et al. (2010) used empty, half-full and full semi-circular tubing to coarsely model the snake profile, and they found an aerodynamic behavior robust to shape changes. The lift coefficient was shown to increase up to 30° angle of attack reaching a maximum of 1.5, but high lift was maintained up to 55° angle of attack, with a lift-to-drag ratio of 2.4-2.8 over a wide range of angles of attack. Stall gradually occurred beyond 30° angle of attack, as lift failed off slowly and drag increased. The ventral lip at the trailing edge was found to have the biggest impact on producing high lift forces by further deflecting the flow downward. Holden et al. (2014) studied the aerodynamic performance of anatomically accurate models with the cross-sectional shape of Fig. 1A. They used load cell measurement and digital particle image velocimetry (PIV) and

focused on the fluid dynamics to determine the underlying physics of snake's aerodynamics. In addition, they examined several Reynolds numbers representing a range of body sizes and glide speeds. They found lift and drag coefficients generally resembling the results of (Miklasz et al., 2010) with slight dependence on Reynolds number; however, the anatomically-accurate snake profile enjoyed a significantly larger maximum lift coefficient of 1.9 for Reynolds numbers $Re \geq 9000$. Vortex trajectory analysis of the experimental velocity field and subsequent computational investigations (Krishnan et al., 2014) suggested that vortex-induced suction on the dorsal surface of the snake may underlie such a surprisingly high lift coefficient.

The snake profile is superior to many other thick airfoils in steady flows with the same Reynolds numbers; however, even such an outstanding aerodynamic performance is not sufficient to explain the gliding abilities of real snakes. For instance, estimations of the required lift-to-drag ratio based on the assumption of equilibrium gliding at 13° glide angle – the shallowest glide angle observed in snakes – are significantly larger than the measured values (Socha et al., 2010, Holden et al., 2014). Therefore, some mechanism must give the snakes a better aerodynamic performance than the already measured data. Unsteady and 3D effects have previously been shown to augment lift in some biological systems (e.g. Bahlman et al., 2013, Wang et al., 2014, Shyy et al., 2009, Song et al., 2014, Muijres et al., 2008, Lentink and Dickinson, 2009, Bomphrey et al., 2006), but the snake's exceedingly large value of advance ratio (ratio of the forward motion to the reciprocating motion) compared to that of insects and birds (Vogel, 2003, Dickson and Dickinson, 2004, Holden et al., 2014) suggests that unsteady mechanisms are less likely to produce a significant aerodynamic contribution. Another possibility, rendered by the staggered S-shaped configuration of the gliding snake, is that a complex interaction between the fore and the aft body takes place where vortices formed upstream are intercepted by the downstream cross-sections. Such interactions have been previously observed in flapping wings with an often favorable contribution to the aerodynamics (Akhtar et al., 2007, Lehmann, 2008, Lehmann, 2009, Maybury and Lehmann, 2004, Usherwood and Lehmann, 2008, Wang and Russell, 2007, Warkentin and DeLaurier, 2007, Weimerskirch et al., 2001). There also exist a few studies (Scharpf and Mueller, 1992, Michelsen and Mueller, 1987, Husain et al., 2005) on static tandem airfoils in flows with Reynolds numbers $Re=8.5\times10^4$-2.25×10^5, showing mixed aerodynamic effects. A simplified preliminary study (Miklasz et al., 2010) used 2D snake-like airfoils and Re=15000; gap and stagger were varied, but the upstream

and downstream angles of attack were kept fixed at 25°. The force coefficients, measured only for the downstream airfoil, suggested that the tandem arrangement of two airfoils could produce significant lift enhancement and drag reduction for the downstream airfoil relative to a solitary airfoil at the same angle of attack.

These results should be considered with caution because differences between the simple geometry of the model and the snake's true cross-sectional shape may result in large differences in flow patterns, potentially causing a large deviation between the measured force coefficients and those experienced by the snakes. Moreover, a vast portion of the tandem arrangement parameter space remains unexplored. The present work aims to study the characteristics of the complex interactions among the snake's body parts. In a simplified approach, those interactions can be approximated by two-dimensional anatomically accurate airfoils placed in tandem with several snake-related configurations (Fig. 1B). By varying the gap and stagger spacing between the two airfoils as well as the angles of attack, it is possible to reproduce a wide range of conditions representative of the snake's flight configurations. Load cells are used to measure the individual lift and drag forces acing on each airfoil. Also, digital particle image velocimetry (PIV) is used to determine the flow field data and test the hypothesis that the underlying vortex-blade interaction is responsible for the vortex-induced lift augmentation and drag reduction. This study furthers our knowledge about how snakes produce flight forces. Because control of gliding is carried out using aerodynamic forces, valuable insight is also provided about how the snake's control system works in connection with its aerodynamics. Finally, this study determines the physical bounds on the aerodynamic capabilities of the tandem airfoils, allowing us to predict the limits on the snake's aerial performance.

2. Methods

In designing our experiments, we had to minimize the number of independent variables so that the number of test cases would not become impractically large. First, we used the previous measurements (Holden et al., 2014) showing that the aerodynamic performance of a single airfoil is mildly dependent on the Reynolds number. Hence, in the present study, we kept the Reynolds number fixed at Re=13000 (with chord as the characteristic length), which is representative of the developed stage of glide in an adult snake. Instead, we emphasized the effects of the

staggering configuration. The parameter space for placing two airfoils in tandem consisted of the distances between the airfoils parallel to the flow (gap, Δx) and perpendicular to it (stagger, Δy), and the upstream and downstream angles of attack, α_u and α_d. Sampling of this large parameter space entailed a trade-off between being able to capture the important phenomena and generating a feasible test matrix. To somewhat reduce the volume of the parameter space, we restricted our attention to its snake-relevant portion, which was determined based on the previously determined kinematic data (Socha et al., 2010). Guided by these data, the distances were varied in the ranges $2c < \Delta x < 8c$ and $0c < \Delta y < 5c$, with c being the chord length of the airfoil. Because no data exist for the angle of attack, we used the range of glide angles reported in (Socha et al., 2005) to approximate the range of angles of attack as $0 < \alpha_u, \alpha_d < 60°$. This approximation is justified by the kinematic data indicating that the snakes glide generally level with the ground (Socha et al., 2010), in conjunction with assuming small twist along the body, which means that the body cross-sectional shape is more or less aligned with the plane of mean body posture. We also considered the possibility that the fore and the aft body may not have the same angle of attack; however, in accordance with the assumption of small twist, we rejected combinations with excessive difference between α_u and α_d. The generated test matrix is summarized in Table 1. The combinations of the angles of attack in the test matrix could be sorted in two groups: (i) the upstream angle of attack was kept fixed at $\alpha_u = 30°$ and the downstream angle of attack was varied from 0° to 60°, and (ii) the downstream angle of attack was kept fixed at $\alpha_d = 30°$ and the upstream angle of attack was varied from 0° to 60°.

Load cell measurements were carried out to determine the aerodynamic performance of the tandem airfoil arrangements for all of the 4×6×8=192 test cases from Table 1. Next, we used digital particle image velocimetry (DPIV) to obtain the flow field measurements for select cases that exhibited significant lift enhancement compared to single models. The velocity field results were used to estimate the aerodynamic forces and verify the load cell measurements, as well as to carry out several other analyses including proper orthogonal decomposition and spectral analysis.

2.1. Experimental model and test facility

All experiments were conducted with the snake models used in (Holden et al., 2014). The models were geometrically accurate replicas of the cross-sectional shape of the airborne snake (Fig. 1A). Each model was rapid prototyped from ABS plastic (DREAMS lab, Virginia Tech) with a chord of 25.4 mm and an aspect ratio of 20 to simulate a single 2D segment of the snake's. The experiments were conducted in a closed-loop water tunnel in Virginia Tech with a 0.6×0.6×1.5 m test section. The freestream turbulence intensity at the test location was less than 3% at speeds up to 0.5 m/s (Gifford et al., 2011).

2.2. Load cell measurements

In the experimental setup of (Holden et al., 2014), four 5 lb (22 N) load cells (LCFD-5, accuracy: ±0.15% FSO, DMD-465WB, strain-gage amplifiers; Omega Engineering, Stamford, CT, USA) were used to simultaneously measure the lift and drag forces on the model, which was mounted to the load cells with support arms. The setup was designed to minimize unwanted effects: the support arms were completely encased by acrylic sidewalls to prevent interaction with the water flow, the leading edges of the acrylic sidewalls were designed with super-ellipse shapes to avoid separation, and the model spanned the entire width between the sidewalls with a clearance of ~1 mm to eliminate 3D effects. For the tandem model experiments, the sidewalls of the same setup were modified with two grids of holes as shown in Fig. 2 to accommodate the second model. This way, the lift and drag forces on one of the models were measured while the other model was fixed to the sidewalls. LabVIEW software (National Instruments, Redmond, WA, USA) and a DAQ board (NI PCI-6251) were used to record the data for each trial at a sampling rate of 1000 Hz for 30 s. The weight of the experimental setup and model was accounted for by zeroing the force measurement before each trial.

The lift and drag coefficients were calculated as

$$C_L = \frac{2F_L}{\rho U^2 c l} \ , \ C_D = \frac{2F_D}{\rho U^2 c l} \tag{1}$$

where F_L and F_D are the measured lift and drag forces, ρ is the water density, U is the freestream velocity, c is the chord length, and l is the span length of the model.

The experiments and analyses of this section were entirely carried out by Daniel Holden following his own research work (Holden, 2011).

2.3. Flow field measurements

The flow field was spatiotemporally resolved using planar digital PIV measurements to quantify flow field characteristics including vorticity and pressure fields. To minimize the undesirable optical effects in the captured images, the acrylic sidewalls of the force measuring setup were modified to accommodate detachable walls of acrylic exclusively cut for each combination of gap and stagger (Fig. 3A). The experimental models were rigidly mounted to the detachable walls for the PIV measurements. To seed the water tunnel, we used small, neutrally buoyant, hollow glass spheres (mean diameter, 126.4 μm) that acted as flow tracers. The particles were illuminated using a dual head laser system (Pegasus PIV, New Wave Research, Portland, OR, USA), whose light was guided through an optical train and spread into a thin plane (1 mm thickness). To eliminate the shadow cast by the models, two mirrors were placed above the snake model on top of the experimental setup to reflect the laser plane back through the test section. The desired region of interest was quite large containing the two models, the sizable distances between them (maximum of 6 chords of gap and 3 chords of stagger, see Table 1), and the downstream wake. We used two cameras to be able to capture this region with sufficient resolution. Even so, the camera placement needed to be carefully designed because (i) adequate overlap ought to exist between the field of view of the two cameras, and (ii) to capture the entire height of the desired field of view, the cameras had to be placed at a 1 in vertical offset for the cases with stagger of $\Delta y = 2$c or 3c, whereas they had to be placed at the same level for the cases with stagger of $\Delta y = 0$c or 1c (Fig. 3B). High-speed video cameras (XS-5, Integrated Design Tools, Tallahassee, FL, USA) were used to record images at a sampling rate of 1000 Hz. With a resolution of 1024×1280 pixels for each camera, an image magnification of 108.1 μm/pixel was achieved. Before taking each set of data, both cameras took images of a calibration grid (an aluminum plate with a grid of dots), which was placed accurately at the laser sheet plane. The calibration data were used to determine the overlap between the two cameras, and to later 'stitch' the upstream and downstream data.

The time-resolved DPIV images were processed with the publicly available code PRANA, developed at Virginia Tech (Eckstein and Vlachos, 2009). We used the Robust Phase Correlation (RPC) with three iterations of multigrid iterative deformable windows (Scarano,

2001) to correlate the images and determine the instantaneous velocity field. Iterative deformable windows were used because they improved the particle image pattern and prevented loss-of-pairs due to in-plane motion at areas with high shear. Gaussian image masking and spatial filtering of the velocity fields between iterations were employed to stabilize the iterative process (Schrijer and Scarano, 2008). PIV processes were carried out with three passes, one pass with 64×64 pixel interrogation windows, and two passes with 32×32 pixel interrogation windows. After each pass, the results were validated using velocity thresholding and universal outlier detection to replace significantly bad vectors (Westerweel and Scarano, 2005). The final processed velocity fields had a uniform vector grid spacing of 8 pixels.

2.4. Spectral analysis

Spectral analysis was performed on the force coefficients (Eq. (1)) to determine the dominant spectral components and the vortex shedding behavior. The frequencies were made nondimensional as

$$f^* = \frac{fh}{U} \tag{2}$$

where f is the frequency, h is the characteristic length, and U is the freestream velocity. The characteristic length was considered for both models to be the same and equal to the projection of the model with 30° angle of attack perpendicular to the freestream.

To provide a comparison between the force and velocity data, spectral analysis was performed also on the velocity field, one chord length downstream of the centroid of each airfoil (Fig. 3B).

2.5. PIV-based aerodynamic force calculation

Starting from the integral form of the momentum equation for a steady control volume surrounding an airfoil, the force acting on the airfoil is found to be

$$\bar{F} = -\iiint \rho \frac{\partial \bar{v}}{\partial t} dV - \oiint \rho \bar{v} \left(\bar{v} \cdot \hat{n}\right) dS - \oiint p\hat{n}\, dS + \oiint \hat{n} \cdot \bar{\bar{\tau}}\, dS \tag{3}$$

where $\bar{F}$ is the force vector, $\bar{v}$ is the velocity vector, ρ is the water density, p is the pressure, $\hat{n}$ is the force vector, and $\bar{\bar{\tau}}$ is the stress tensor. For a statistically steady flow, the time average of the first integral, which is the unsteady term, is zero. The second and third integrals represent the contributions from the momentum flux and pressure, respectively. The last integral, which includes the contribution of viscous effects, is usually eliminated by properly choosing a control surface on whose boundaries the viscous stresses and the turbulence stresses are negligible. However, we were not able to follow the same procedure because the downstream airfoil was too close to either the upstream airfoil (cases with $\Delta x = 2c$) or the downstream boundary of the image (cases with $\Delta x = 6c$). To find the stress integral, we calculated the stress tensor as

$$\tau_{ij} = \mu\left(\frac{\partial u_i}{\partial x_j} + \frac{\partial u_j}{\partial x_i}\right),\ i, j = 1,2 \tag{4}$$

in which, the partial derivatives were numerically obtained using the second-order central difference method. The pressure field was calculated using virtual-boundary, omni-directional pressure integration (Charonko et al., 2010).

After finding the forces, Eq. (1) was used to obtain the lift and drag coefficients.

2.6. Proper orthogonal decomposition

Proper orthogonal decomposition (POD) is a mathematical tool to decompose a dataset in space and time into orthogonal basis functions that capture the most energetically important modes of the data. In fluid mechanics, POD can be considered as a physics-based filter retaining the most energetic modes of the velocity field, which tend to be less contaminated by noise. By contrast, the lower energy modes contain a large amount of noise and are discarded. POD has been applied to a wide variety of problems in fluid mechanics in this way (Smith et al., 2005, Santa Cruz et al., 2005, Berkooz et al., 1993). Here, we filtered the velocity data using POD with the method of snapshots (Smith et al., 2005) and kept the modes that accounted for 80% of the total energy.

In connection with POD, the energy fraction of modes and entropy are defined as

$$\mathrm{EF}_j = \frac{\lambda_j}{\sum_{i=1}^{N} \lambda_i} \ , \ j = 1,\ldots,N \tag{5}$$

$$H = -\frac{1}{\log N} \sum_{i=1}^{N} \mathrm{EF}_i \log\left(\mathrm{EF}_i\right) \tag{6}$$

where λ_i is the energy of mode i, and N is the total number of modes. Basically, energy fraction is the ratio of each mode's energy to the total energy. For organized wakes, only a small number of modes would dominate the flow, whereas mode energy is distributed more uniformly in a very turbulent flow. Entropy quantifies the complexity and order of the flow. With a minimum value of 0, entropy indicates that the total energy is contained in only one mode, and with a maximum of 1, it means that the energy is distributed evenly among all of the modes (Santa Cruz et al., 2005).

2.7. Uncertainty analysis

We used the propagation of error to calculate the uncertainty ranges for the lift and drag coefficients obtained from the force measurements. It was shown in (Holden, 2011) that the random error in the force measurements was negligible; therefore, we considered only the systematic uncertainty. The terms contributing to the uncertainty of the force measurements include (i) load cell data (combined linearity and hysteresis error of 0.15% FSO), (ii) freestream velocity (0.02 m/s), (iii) moment arm lengths (5×10^{-4} m), (iv) model chord length (5×10^{-7} m), and (v) model span (7.9×10^{-5} m). For more details, see (Holden, 2011).

3. Results

3.1. Lift and drag coefficients

The overall aerodynamic performances of the tandem configuration of the snake models are summarized in Fig. 4, where the lift and drag coefficients obtained from tandem force measurement data are compared to the summation of those coefficients for two solitary models having the same angles of attack. Each of the eight plots in the figure represents the data for a

combination of α_u and α_d (See Table 1). In general, the lift coefficient underwent more changes than the drag coefficient. The tandem effects were larger when the models were placed closer to each other, but when the distance between the models increased, the tandem lift and drag coefficients generally converged to those of single models. In particular, the tandem effects diminished, almost independent of gap, when the stagger became larger than two chord lengths, except for the lift coefficients with $\alpha_u = 0°$ and $\alpha_d = 30°$, which received the utmost influence from the tandem arrangement. For these angles of attack and with $\Delta x = 2c$, extreme changes occurred in the lift coefficient, where it went from zero (about -100% change) to more than three times (~200% change) of the single model data, with the stagger changing from zero to one chord. The lift and drag coefficients degraded when the models were at zero stagger for all configurations except those with $\alpha_u = 30°$ and $\alpha_d = 0°$. For the latter cases, the lift coefficients somewhat increased whereas the drag coefficients with $\Delta x > 2c$ almost did not change.

Fig. 5 summarizes the changes in the lift-to-drag ratio. As for the lift and drag coefficients, changes in the lift-to-drag ratio generally became smaller when the models were placed farther apart, with the stagger having a larger influence than the gap. Also, the lift-to-drag ratio mainly followed the patterns in the lift coefficient, most noticeably for cases with $\alpha_u = 30°$ and $\alpha_d = 0°$, or $\alpha_u = 0°$ and $\alpha_d = 30°$, as the drag coefficient received smaller effects from the tandem arrangement. The big variation in the lift-to-drag ratio with $\Delta x = 2c$, $\alpha_u = 30°$ and $\alpha_d = 60°$ was an exception that resulted from simultaneous lift enhancement and drag reduction. Fig. 6 shows the contour plots of the overall lift-to-drag ratio of the tandem airfoils in the Δx-Δy plane with each panel corresponding to a combination of the angles of attack. When $\alpha_u = 20°$ and $\alpha_d = 30°$, or vice versa, the tandem lift-to-drag ratio was generally larger than other combinations of the angles of attack, and it displayed small dependence on the relative position of the airfoils. At these combinations of the angles of attack, the maximum value of the tandem lift-to-drag ratio exceeded 2.2 and was almost 20% larger than that of single models with the same angles of attack. For some other combinations of the angles of attack, relatively large changes in the lift-to-drag ratio could be obtained by adjusting the horizontal and vertical distance between the airfoils. For instance, with $\alpha_u = 30°$ and $\alpha_d = 0°$, there was a preferred posture ($\Delta x = 6c$ and $\Delta y = 1c$) that would produce a considerable enhancement in the

aerodynamic performance of the tandem system. Also, with $\alpha_u = 30°$ and $\alpha_d = 60°$, the tandem lift-to-drag ratio became close to its global maximum value at $\Delta x = 2c$ and $\Delta y = 1c$ although it rapidly decayed and remained almost unchanged for other postures.

The circles in Fig. 5 specify the cases for which flow fields were measured with PIV. The PIV cases were selected based on the distinguished changes in their lift-to-drag ratios, and they were used to study the fluid mechanisms behind the extreme tandem effects and the aerodynamic properties of the snake-related configurations. To minimize redundancy, almost all of the flow field results in this work concern the cases depicted by red circles. The following two categories of tandem arrangements were considered in the selection of the 'red' cases: (i) Analysis of body configurations in airborne snakes (Socha et al., 2010) has revealed that the most probable relative position of the fore and the aft body airfoils is 6-8 chords of gap and 2-3 chords of stagger. These data conspicuously overlapped with the configurations having $\alpha_u = 30°$ and $\alpha_d = 0°$ that produced the largest tandem effect on the lift coefficient and the lift-to-drag ratio. The first group of the red cases includes those configurations along with the 'neighbors' that lack the large tandem effect. For instance, by just changing the downstream angle of attack, the significant tandem effect in $\Delta x = 6c$, $\Delta y = 2c$, $\alpha_u = 30°$, $\alpha_d = 0°$ nearly vanished in $\Delta x = 6c$, $\Delta y = 2c$, $\alpha_u = 30°$, $\alpha_d = 20°$. (ii) The uttermost tandem effects happened with $\Delta x = 2c$, $\alpha_u = 0°$ and $\alpha_d = 30°$, which are included in the second group of the red cases along with their less influenced neighbors.

Within each highlighted group, the three cases that had the same gap and angles of attack but were different in stagger were the most interesting, as very large changes in the aerodynamic performance could be obtained with small changes in the vertical separation. The individual lift and drag coefficients of these configurations are tabulated in Table 2. The first three configurations in Table 2 are relevant to the real snake posture ($\Delta x = 6c$, $\alpha_u = 30°$, $\alpha_d = 0°$), for which the aerodynamic performance of the upstream airfoil was similar and almost the same as a single model at 30° angle of attack. By contrast, the downstream airfoil produced significantly larger lift and smaller drag with $\Delta y \leq 2c$, but the enhanced performance was lost at $\Delta y = 3c$. The second three configurations in Table 2 are the cases experiencing the uttermost tandem effects ($\Delta x = 2c$, $\alpha_u = 0°$, $\alpha_d = 30°$). At $\Delta y = 0c$, the lift and drag of both tandem models changed with respect to their single model counterparts, but the overall lift summed to about zero, which

resulted in a drastic negative change in the combined lift and lift-to-drag ratio (Figs. 4 and 5). At $\Delta y = 1c$, the upstream airfoil with 0° angle of attack produced positive lift, as opposed to negative lift of a single model (Holden et al., 2014), which was the most important contribution to the drastic enhancement of the combined aerodynamic performance. At $\Delta y = 2c$, the upstream lift became negative again but remained larger than the single model lift; therefore, the tandem system experienced a smaller positive change in the aerodynamic performance.

In Fig. 7, the individual lift and drag coefficients estimated from the PIV data are compared to those as measured using the load cells, with the error bars representing the measurement uncertainty. Overall, the results obtained from the two methods were in satisfactory agreement, with the PIV estimated results mostly lying within the uncertainty range of the measured data, and with the maximum relative error being about 18%. The data were grouped according to the abovementioned categories; the red shades denote the two groups of cases whose details were studied, and the blue shade specifies the rest of the PIV cases. It is observed that for the first red group, where the gap between the models was larger, the upstream model was almost unaffected by the presence of the other model; however, the downstream model in some cases received the influence of the upstream model resulting in a largely modified lift coefficient. By contrast, in the second red group where the gap was smaller, the lift and drag of both models were altered.

3.2. Spectral analysis

Fig. 8 shows the spectra of the measured forces, which represent the vortex shedding behavior of the tandem system. It is observed that for all the upstream cases in Fig. 8A, a single dominant frequency existed at $f^* \approx 0.23$, which was independent of the tandem configuration. The dominant frequency of the downstream airfoil was 'locked' at the upstream dominant frequency for four cases, it was different ($f^* \approx 0.34$) for two other cases, and in another configuration the downstream spectra exhibited two peaks, one of which coincided with the upstream peak. The spectra of the cases in Figs. 8C and 8D were less orderly, with the peak frequency varying from $f^* \approx 0.23$ to $f^* \approx 0.42$, and neither of the upstream and downstream groups showing a preferred dominant frequency. In particular, no clear peak could be identified for the case $\Delta x = 2c$,

$\Delta y = 0c$, $\alpha_u = 0°$ and $\alpha_d = 30°$; however, increasing the stagger to $\Delta y = 1c$ resulted in two locked dominant frequencies. When the stagger was increased to $\Delta y = 2c$, the secondary peak vanished and the primary dominant frequencies no longer matched. For all other configurations, no secondary peak was observed, but the upstream and downstream primary peaks matched.

Fig. 9 shows the probability density of the upstream and downstream dominant frequencies for different combinations of the angles of attack. Each probability density curve was obtained from the compilation of all peaks in the spectra of any combination of gap and stagger. Generally, the upstream model experienced a single peak, which was also shared by the downstream model. This frequency was a function of the configuration and varied with the angles of attack. In addition to the upstream dominant frequency, the downstream model exhibited one or more peaks that could be smaller or larger than the upstream peak frequency. Overall, the tandem configuration could influence the spectra of the models by changing the dominant frequency, which was usually shared by both models, and by creating additional peaks for the downstream model.

Figs. 10 and 11 encompass the spatially resolved power spectra of the vertical velocity component one chord downstream of each airfoil. These results were in agreement with those obtained from the spectral analysis of forces. In addition to the dominant frequencies, the velocity spectra revealed the behavior of the wake structure behind each model. It is observed that the position and distribution of the wake varied with the configuration. For the cases presented in Fig. 10, the upstream high power band was relatively narrow and symmetric relative to the airfoil position, with the maximum energy contained between $Y = -c$ and $Y = c$. By contrast, the downstream wake was asymmetric and shifted a little upward, except for $\Delta x = 6c$, $\Delta y = 2c$, $\alpha_u = 30°$, $\alpha_d = 20°$, which had a symmetric spectrum. The cases presented in Fig. 11 experienced greater influence from the tandem configuration, which caused the vertical position, distribution width, and frequency of the high power band to vary. For the case $\Delta x = 2c$, $\Delta y = 0c$, $\alpha_u = 0°$, $\alpha_d = 30°$, the power was spread for a large range of frequencies and no preferred frequency could be identified. For the same gap and angles of attack but with stagger increased to $\Delta y = 1c$, a clear high power upstream band emerged at $f^* \approx 0.42$. The downstream spectra exhibited a band at $f^* \approx 0.23$ which was shifted downward; moreover, the upstream wake was sensed two chord lengths above the downstream model. Keeping the same configuration but

increasing the stagger to $\Delta y = 2c$ caused the downstream band to become stronger and symmetric; also, the upstream wake was no longer sensed. Keeping the stagger at $\Delta y = 1c$ and changing the upstream angle of attack to $\alpha_u = 20°$ caused the power bands of both models to spread over a larger spatial and frequency range. Dependence of the downstream wake structure on the tandem configuration was also observed in the cases with $\Delta x = 4c$. An interesting point about the tandem wake was that it had a larger spatial distribution than a single model. For instance, the spatial distribution of the wake of model at 0° angle of attack in tandem configuration was comparable to that of a single model at 60° angle of attack (Holden et al., 2014).

3.3. Velocity field

To visualize the flow topology and better understand the mechanisms through which the tandem configuration modifies the aerodynamic performance of the system, the mean velocity field is plotted in Figs. 12 and 13 for the cases tabulated in Table 2. The background color indicates the velocity magnitude normalized with respect to the freestream velocity and the gray shades are the regions where the flow field data could not be captured owing to shadows. The previous results indicating that with $\Delta x = 6c$, $\alpha_u = 30°$, $\alpha_d = 0°$, the upstream airfoil was mainly not affected by the hanging the stagger were confirmed by the mean velocity fields of Fig. 12, which clearly show that mean velocities around the upstream airfoils were almost identical. However, the mean flow speeds close to the downstream airfoil as well as the mean downstream wake were significantly influenced by the tandem arrangement. In particular, the downstream wake grew considerably longer as the stagger increased. Fig. 13A shows that with $\Delta x = 2c$, $\alpha_u = 0°$, $\alpha_d = 30°$ and zero stagger, the downstream airfoil interfered with formation of the upstream wake and caused it to become excessively elongate. It is further observed that the mean flow speeds in the vicinity of both airfoils were significantly altered by the change in the stagger. For instance, the flow speed close to the dorsal surface of the downstream model at $\Delta y = 0c$ was notably smaller than that at $\Delta y = 1c$ and $\Delta y = 2c$, whereas the flow speed close to the ventral surface of the upstream body substantially decreased when the stagger was increased from $\Delta y = 0c$ to $\Delta y = 1c$.

For a single snake-like airfoil, flow separation from the lower surface of the models with 0° angle of attack has been argued to play an important role in producing negative lift by creating a low pressure region (Holden et al., 2014). Figs. 14 and 15 depict the mean streamlines in the vicinity of the 0° angle-of-attack airfoils of the tandem configurations in Table 2 and provide details of the flow structure around them. It is clear that flow generally separated from the concave ventral surface creating a 'trapped' vortex in the cavity. However, the size of the ventral wake and the strength of the trapped vortex were depending on the configuration. Even in one case, where $\Delta x = 2c$, $\Delta y = 1c$, $\alpha_u = 0°$, $\alpha_d = 30°$, the gap flow did not allow the flow to separate from the lower surface and no ventral vortex could be formed (Fig. 15B). Finer details about the size and structure of the dorsal wakes can also be observed from Figs. 14 and 15.

The mean recirculation region (also referred to as the mean wake bubble) is defined as the region in the flow where the streamwise component of the velocity and the freestream velocity are in opposite directions. In the absence of vortex shedding, the length of the mean recirculation region has been related to the base pressure of certain bluff bodies (Balachandar et al., 1997), stating that a shorter recirculation region would produce a larger base suction, and therefore a larger drag coefficient. The small upstream drag coefficient for the case $\Delta x = 2c$, $\Delta y = 0c$, $\alpha_u = 0°$, $\alpha_d = 30°$ could be explained by its excessively long recirculation region (Fig. 16B). Moreover, in Fig. 16A, $\Delta y = 1c$ resulted in the smallest recirculation region, suggesting that – as mentioned earlier – the wake vortices were formed closer to the dorsal surface and the suction from vortices increased lift and decreased drag. A similar mechanism is suggested for the high lift and small drag of the case $\Delta x = 2c$, $\Delta y = 1c$, $\alpha_u = 0°$, $\alpha_d = 30°$ according to Fig. 16B.

3.4. Pressure field

According to Eq. 3 and ignoring the unsteady effects for a statistically steady flow, three factors contribute to the net force acting on the airfoils: (i) pressure, (ii) the momentum flux, and (iii) the viscous stresses. PIV data were used to estimate each of these terms as well the total lift and drag coefficients, and the results for the tandem configurations of Table 2 are shown in Fig. 17. The load cell data are also included for comparison. As previously indicated by Fig. 7, the PIV-based estimations of the lift and drag coefficients were in agreement with the load cell measurements and confirmed them. Moreover, it was revealed that the contribution from the viscous stresses

was mostly negligible, whereas the momentum flux could make a large contribution or a small one (e.g. ~48% to the upstream lift, and ~0% to the downstream lift with $\Delta x = 2c$, $\Delta y = 0c$, $\alpha_u = 0°$, $\alpha_d = 30°$). However, it was pressure that made for the largest part of each of the force coefficients. Therefore, the effects of the tandem arrangement on the aerodynamic behavior of the airfoils could be broadly examined by considering the changes in the mean pressure field shown in Figs. 18 and 19.

In Fig. 18, the upstream pressure in all cases experienced a large high-pressure zone at the ventral surface and a large low-pressure zone at the dorsal surface near the apex. The characteristics of this pressure field were slightly influenced by the varying stagger. However, significant changes in the downstream pressure field were observed. The high-pressure zone at the stagnation point on the dorsal surface of the models increased both in size and magnitude as the stagger increased from $\Delta y = 1c$ to $\Delta y = 3c$. More importantly, the low-pressure zone at the ventral surface became significantly stronger creating an increasing downforce. The aft of the model was also surrounded by a low-pressure region.

Fig. 19 shows that at $\Delta y = 0c$, the upstream pressure field consisted of a high-pressure region at the stagnation point on the dorsal surface and a low-pressure zone at the concave ventral zone. At $\Delta y = 1c$, the high-pressure zone increased in size and enveloped even parts of the ventral surface. The whole aft body and the dorsal surface past the apex were surrounded by a low-pressure region caused by wake vortices. By increasing the stagger to $\Delta y = 3c$, the low-pressure zone considerably expanded and enveloped some parts of the dorsal surface before the apex as well as the whole ventral surface. Fig. 19 shows that the downstream pressure field was also a function of stagger. At $\Delta y = 0c$, rambling high-pressure regions existed at the leading edge and the ventral surface, whereas a strong low-pressure zone surrounded most of the dorsal surface and the whole aft of the model. However, at $\Delta y = 1c$ and $\Delta y = 2c$, the pressure field became generally similar to the 30° angle-of-attack airfoils of Fig. 18, with high-pressure and low-pressure zones at the ventral and dorsal surfaces, respectively.

3.5. POD modes

The entropies calculated in connection with proper orthogonal decomposition of the cases in Table 2 are plotted in Fig. 20. The majority of the tandem model entropies were significantly larger than the maximum entropy of $H = 0.425$ for a single model (Holden et al., 2014). Clearly, the tandem model flow was less ordered and entailed greater turbulence. It is also observed that the largest entropies belonged to the cases with the largest interaction between the two airfoils. In particular, a very large entropy for the case $\Delta x = 2c$, $\Delta y = 0c$, $\alpha_u = 0°$, $\alpha_d = 30°$ was obtained (Fig. 20B) because the downstream airfoil interfered with the formation of upstream wake, which in return, altered the flow around the downstream model. This scenario is evident from Fig. 21A which depicts the associated first two POD eigenmodes. Santa Cruz et al. (2005) and Epps and Techet (2010) showed that the first two eigenmodes can be used to accurately reconstruct the dynamics of Kármán vortex streets. Therefore, Fig. 21A indicates that a strong and organized Kármán vortex street could not be produced. With $\Delta y = 1c$, the entropy decreased but the interaction between the models still existed as the vortices shed from the two models were coupled (Fig. 21B). With $\Delta y = 2c$, the entropy decreased even more as the interaction between the two models considerably diminished. Fig. 21C shows that the more energetic vortex shedding modes, which were produced by the downstream model, were only slightly influenced by the presence of the upstream model.

4. Discussion

4.1. Tandem aerodynamic performance

Our results verified the strong dependence of the aerodynamic performance of the tandem system on the configuration. However, that dependence was not uniform throughout the configuration space. For example, the lift and drag coefficients were very sensitive to the relative position of the airfoils at some combinations of the angles of attack, whereas the sensitivity of the aerodynamics performance on the gap and stagger were minimal for other angles of attack. Nonetheless, the results showed greater sensitivity to stagger, and the tandem effects almost universally diminished when the stagger was larger than three cord lengths. This can be explained by the vortex-blade interaction mechanism responsible for the aerodynamic force production. For smaller stagger, the vortices shed from the upstream airfoil passed closer to the

downstream airfoil, and therefore could produce a larger influence on it. By contrast, when the vertical distance between the airfoils increased, less interaction could happen.

To account for the details of how the lift and drag coefficients varied with the tandem configuration, we need to consider the flow topology. The velocity fields depicted in Fig. 12 show that the mean velocities around the upstream airfoils remained almost unchanged by the varying stagger when $\Delta x = 6c$, $\alpha_u = 30°$, $\alpha_d = 0°$. This confirms the corresponding data in Table 2 indicating that the aerodynamic performance of the upstream model was almost the same at these configurations. Fig. 12 also shows the effects of the tandem arrangement on the downstream airfoil. The mean velocities close to the dorsal and ventral surfaces of this airfoil at $\Delta y = 1c$ were respectively larger and smaller compared to those at $\Delta y = 3c$. Therefore, the downstream airfoil at $\Delta y = 1c$ enjoyed a larger circulation and produced a larger lift according to the Kutta-Joukowski theorem. Moreover, it is observed that the mean wake was shorter at $\Delta y = 1c$, meaning that wake vortices were formed closer to the dorsal surface of the model and vortex-induced suction could augment lift. In a similar manner, the mean velocity fields depicted in Fig. 13 can explain the aerodynamic performances of the airfoils with $\Delta x = 2c$, $\alpha_u = 0°$, $\alpha_d = 30°$ summarized in Table 2. First, the interference of the downstream model with the upstream wake resulted in a distorted wake and therefore no vortex-induced lift enhancement could be achieved. In addition, the upstream wake did not allow the mean velocities close to the dorsal surface of the downstream model to reach the large magnitudes observed in Figs. 13B and 13C. Therefore, the circulation-based downstream lift was considerably smaller. Fig. 13B shows that one chord of stagger modified the gap flow such that (i) the upstream wake could form but was pushed by the gap flow closer to the model, (ii) the mean velocity close to the ventral surface of the upstream airfoil decreased, and (iii) the mean velocity close to the dorsal surface of the downstream airfoil increased. These mechanisms augmented both the upstream and downstream lift through vortex-blade interaction and circulation modification. Fig. 13C shows that increasing the stagger to $\Delta y = 2c$ diminished the effect of the mentioned mechanisms, and therefore, the combined lift and lift-to-drag ratio decreased. Nonetheless, the downstream lift was a maximum at $\Delta y = 2c$, which was the result of the mean wake vortices formed closest to the dorsal surface of the airfoil.

In addition to the circulation around the airfoils and the wake, separation of flow from the model's lower surface originating at the leading edge altered the lift production of the airfoils with 0° angle of attack. Holden et al. (2014) observed negative lift for a single airfoil at 0° angle of attack and argued that it was the result of a low-pressure zone at the concave ventral surface created by a vortex trapped in the cavity. The negative lift was also observed for almost all of the 0° angle-of-attack airfoils in the present study, but the magnitudes of the negative lift were dependent on the tandem configuration. As clearly observed from Fig. 14A, for $\Delta x = 6c$, $\Delta y = 1c$, $\alpha_u = 30°$, $\alpha_d = 0°$, separation occurred at the leading edge and the resulting vortex created a strong down-force that resulted in negative lift. By increasing the stagger to $\Delta y = 2c$ and $\Delta y = 3c$, the trapped vortex gained more strength (Figs. 14B and 14C) and created larger down-forces, which explain why the magnitude of the downstream negative lift increases with stagger for these cases. Fig. 15A evidences the same mechanism for the upstream negative lift with $\Delta x = 2c$, $\Delta y = 0c$, $\alpha_u = 0°$, $\alpha_d = 30°$. However, when the stagger was increased to $\Delta y = 1c$, the gap flow changed in a way that did not allow the trapped vortex to form below the model. As a result, no down-force was created and the upstream lift became positive. Further increasing the stagger to $\Delta y = 2c$ allowed a weak vortex to reappear and the upstream lift became negative again, although with a smaller magnitude than the case with $\Delta y = 1c$.

Overall, drag was much less influenced by the tandem configuration than lift because, unlike lift, drag was created mostly by pressure difference. Fig. 4 shows that zero stagger generally had negative effect on both lift and drag. The negative impact on the combined lift likely originates from the downstream lift being degraded by the upstream wake. Also, drag was reduced by the low-pressure zone created in front of the downstream airfoil. Figs. 13A and 19A exemplify the mentioned interactions between the upstream wake and the downstream airfoil and their effects on the pressure distribution around the downstream airfoil. The situation was different with the downstream airfoil at 0° angle of attack, where the combined lift was enhanced at $\Delta y = 0c$. Inspection shows that decrease in the magnitude of the negative lift of the downstream airfoil made for the biggest contribution to the overall lift enhancement. It might be possible that the upstream wake modified the flow around the 0° angle-of-attack downstream airfoil such that the trapped vortex at the concave ventral surface diminished, and as a result the downforce decreased.

The mean pressure fields of Figs. 18 and 19 provide a more direct explanation of the changes in the lift and drag coefficients of the tandem configurations in Table 2. The pressure field is correlated with the velocity field, confirming the argument that suction created by wake vortices was the predominant mechanism for producing lift. In particular, the low-pressure zone at the ventral surface, which was the key factor related to the magnitude of the negative lift coefficient, changed in accordance with the strength of the ventral vortex. The pressure distribution also accounted for producing drag and its variation with the tandem configuration. For instance, the upstream airfoil with $\Delta x = 2c$, $\Delta y = 0c$, $\alpha_u = 0°$, $\alpha_d = 30°$ experienced an exceptionally small drag coefficient (Table 2) as a result of the diminished base suction in comparison to the cases with $\Delta y = 1c$ and $\Delta y = 2c$, which had increased base suctions and experienced drag coefficients larger than that of a single model (See Figs. 7 and 19). Moreover, Figs. 19B and 19C show that the dorsal low-pressure zone moved slightly beyond the apex as the stagger was changed from $\Delta y = 1c$ to $\Delta y = 2c$. Therefore, in the latter case, the horizontal component of the suction significantly increased resulting in a larger drag coefficient.

The vortex-blade interaction that we used to explain the aerodynamic performance of the tandem system was further confirmed by the spectral analysis revealing that the dominant frequency of the downstream force was locked at that of the upstream force when there was significant modifications in the lift and drag coefficients (Fig. 8). For instance, the dominant frequency of the upstream airfoils (30° angle of attack) in Fig. 8A matched that of a single model with the same angle of attack, likely because the upstream flow was not influenced by the downstream model. The dominant frequency of the downstream airfoil (0° angle of attack) with $\Delta y = 1c$ and $\Delta y = 2c$ matched that of the upstream airfoil ($f^* \approx 0.23$) and a substantial lift-to-drag enhancement was observed for these cases. However, at $\Delta y = 3c$, the downstream dominant frequency became 'unlocked' from the upstream wake and its value suddenly changed to the single model value ($f^* \approx 0.34$). Thereupon, the lift enhancement was entirely lost (See Figs. 4 and 8). Another interesting point about the tandem wake was that it had a larger spatial distribution than a single model. For instance, the spatial distribution of the wake of model at 0° angle of attack in tandem configuration could be comparable to that of a single model at 60° angle of attack (Compare Figs. 10 and 11 to the results of (Holden et al., 2014)).

4.2. Implications about gliding snakes

Despite the large lift enhancement obtained with some configurations close to the kinematics of flying snakes, it is not possible to conclude that the snakes take the staggered posture in order to exploit such aerodynamic enhancements. In fact, the snakes use many other configurations with $\Delta x > 6c$ and $\Delta y > 3c$ (Socha et al., 2010), for which little or no aerodynamic effects exist. Moreover, the snakes rarely use small gaps that would result in the largest tandem effects we observed. Nonetheless, with the angles of attack being 30° and 20° in no particular order, almost any combination of gap and stagger would produce a near-maximum lift-to-drag ratio. Therefore, the snakes might be able to modulate their body posture to exploit such optimal angles of attack. It is interesting to note that in the shallowing part of the glide, the snakes maintain a body angle of 25° from the glide path (Socha et al., 2010), but no further inferences could be made owing to the lack of data for the variation of the airfoil angle along the body.

The results also did not support the hypothesis that lift-to-drag enhancement provided by tandem interactions are sufficient to explain the smallest glide angles observed in snakes. None of the configurations, even those with the largest aerodynamic enhancements, could increase the overall lift-to-drag ratio to the required value of 3.08-4.33 (Socha et al., 2005, Socha et al., 2010). In fact, as demonstrated by Table 2, most of the aerodynamic enhancements happened with one of the airfoils having a 0° angle of attack. Because of the poor performance of the single model with this angle of attack, even its relatively enhanced performance cannot be sufficient. However, the results of this study are not sufficient to dispute the hypothesis either, as a large portion of the parameter space remains unexplored. For example, we did not consider the tandem configurations with both angles of attack at 30°. Moreover, we did not examine the special angle of attack of 35°, for which a single airfoil produced narrow dominant peaks in the lift coefficient ($C_L = 1.9$) and the lift-to-drag ratio ($L/D = 2.7$) with more than 30% increase with respect to the neighboring values at 30° angle of attack. It might be possible that the tandem interactions augment the peak even more and produce sufficiently large lift-to-drag ratios required for the minimum glide angles observed in snakes. Other simplification in the present study was that the effects of the sweep angle, 3D shape of the snake body and spanwise camber were ignored. In particular, it has been shown that spanwise camber is somewhat related to controlling profile drag in a bird (KleinHeerenbrink et al., 2016).

Another hypothesis about why the snakes use the staggered configuration is that they can exploit the resulting changes in the lift and drag to control their gliding trajectory. The relatively large changes in the overall lift-to-drag ratio that accompany slight adjustments in the posture make this hypothesis reasonable. Also, the control hypothesis implies that the snakes would have to actively keep their body in a favorable posture where the sensitivity of the aerodynamic forces to tandem configuration is a maximum. The agreement between this implication and the most probable relative position of body segments in the flying snakes (Socha et al., 2010) along with the results of the present study (see Figs. 4 and 5 with $\alpha_u = 30°$, $\alpha_d = 0°$) further supports the control hypothesis. A possible scenario through which the snakes can actually use tandem aerodynamics to control their glide trajectory is outlined below. In a simple planar motion, if the tandem system is simply assumed to represent the mass distribution of the snake body as well as the aerodynamic forces, it follows that the pitching moments produced by upstream-downstream asymmetry can be used to control the pitch angle (also see (Jafari et al., 2014)). In a three-dimensional motion, with the complex shape of the snake body, external moments can be produced about any arbitrary axis, and therefore full orientation control is achieved. For the control hypothesis to gain weight, it should also be examined whether the snakes are capable of body movements fast enough for controlling their glide. In the developed stage of glide, where the airspeed is close to its equilibrium value, the weight of each part of the body is almost supported by the aerodynamic forces. As a result, any muscular forces and moments will produce an acceleration, which quickly reconfigures the body. It is therefore reasonable to hypothesize that the snakes use postural reconfigurations to modify the aerodynamic forces and use them to control their motion. It is further suggested that the snakes try to keep their posture close to 'sensitive' configurations, which allow them to correct their trajectory with small motions.

4.3. Conclusion

This study determined the aerodynamic performance of a tandem system with airfoils having the cross-sectional shape of *C. paradisi*. As previously observed in single model experiments, vortex shedding and separation dominated the aerodynamics of the tandem system. The vortex-blade interactions were shown to be the main mechanism through which the tandem configuration modifies the overall aerodynamic performance. In addition to understanding the aerodynamics of

flying snakes, the results of this work provide valuable insight about the underlying physics that the control system of the snake uses to maintain the stability or maneuver in midair. Finally, these results can be incorporated in theoretical studies of the dynamics of flying snakes. For instance, (Jafari et al., in prep, Jafari et al., 2014) developed theoretical models of flying snakes , but they used the results of (Holden et al., 2014) to model the aerodynamic forces. Such models can be refined using the tandem aerodynamic data to better approximate the real snakes.

The following limitations existed in our approach: (i) Although the exact variation of cross-sectional shape along the snake body is not known, at least the lateral lips on the ventral side have been reported to become smaller posteriorly toward the vent (Socha, 2011). We ignored the variation of body shape and used uniform models. (ii) The snakes have a complex 3D posture, which can result in complex flow structures and produce significant aerodynamic effects. However, as a first step approximation, the snake posture was modeled just by two straight airfoils. (iii) Based on the results of (Holden et al., 2014) stating that the single model aerodynamics were generally mildly dependent on the Reynolds number, the effects of the Reynolds number were not considered. However, that study also reported significant effects of the Reynolds number at the angle of attack of 35°. (iv) Other effects such as sweep angle and relative motion of the airfoils were also ignored. More realistic experiments in the future are required to assess the degree of importance of the above simplifications.

Table 1: The test matrix for the load cell measurements. Pairs of the angles of attack are separated based on which model has 30° angle of attack. Table entries, one from each column, were combined to determine the test points in the parameter space.

Δx (c)	Δy (c)	(α_u, α_d)
		(30°, 0°)
	0	(30°, 20°)
2	1	(30°, 40°)
4	2	(30°, 60°)
6	3	(0°, 30°)
8	4	(20°, 30°)
	5	(40°, 30°)
		(60°, 30°)

Table 2. The individual lift and drag coefficients for the most interesting cases of tandem effects. The first three cases were relevant to the actual kinematics of flying snakes, and the next three cases received the largest changes in the aerodynamic performance. Within each group, the cases differ only by the stagger.

$\Delta x - \Delta y - \alpha_u - \alpha_d$	$C_L^{upstream}$	$C_D^{upstream}$	$C_L^{downstream}$	$C_D^{downstream}$
6c-1c - 30°-0°	1.3393	0.6799	-0.1116	0.3444
6c-2c - 30°-0°	1.3965	0.7041	-0.1480	0.3568
6c-3c - 30°-0°	1.3588	0.7046	-0.8277	0.4096
2c-0c - 0°-30°	-0.5046	0.3207	0.5358	0.3277
2c-1c - 0°-30°	0.1919	0.4877	1.6255	0.5508
2c-2c - 0°-30°	-0.3455	0.4674	1.6985	0.6725

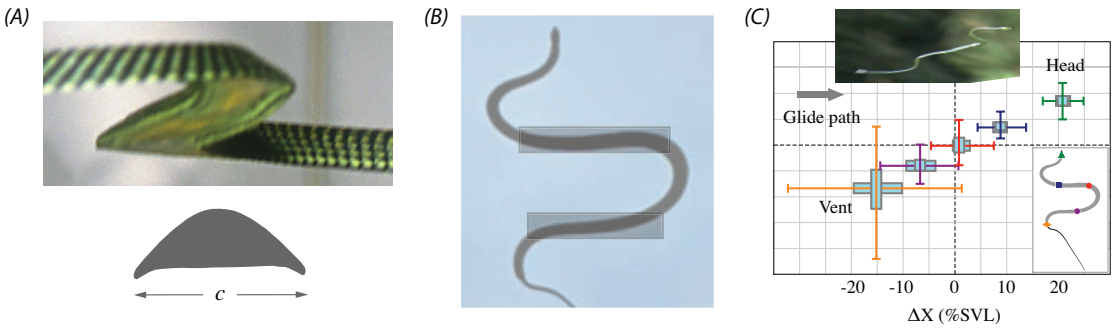

Fig. 1: The flying snake body shape and posture while airborne. (A) The snakes flatten their body when airborne, creating an unconventional airfoil to produce lift (adapted from (Socha, 2011)). (B) The snake assumes an S-like posture, in which the body parts that are roughly perpendicular to the airflow can be considered as a pair of airfoils in tandem. (C) During the developed stage of glide, the snake maintains a staggered posture, as evidenced by the experimental kinematic data from *C. paradisi*. The shown data summarize the displacements of five landmarks on the snake body relative to its mass center and normalized with respect to the snout-vent length (adapted from (Socha et al., 2010)).

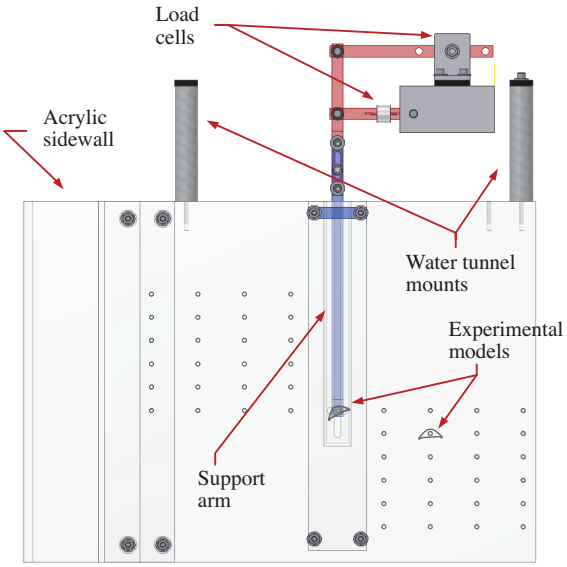

Fig. 2: The sidewalls of the setup used by (Holden et al., 2014) to measure forces on a single airfoil were modified with two grids of holes to accommodate a second model. With the new setup, measurements could be done on one of the airfoils, while the other one was fixed to the walls.

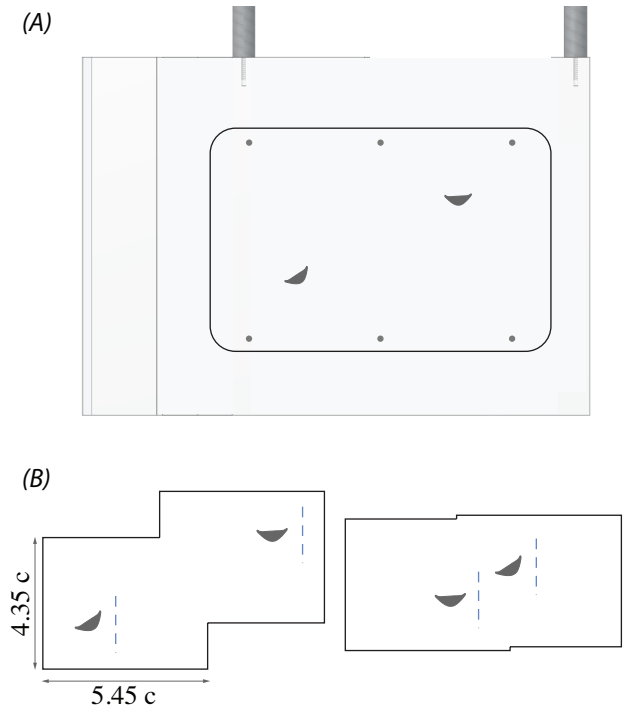

Fig. 3: The PIV measurement setup. (A) The sidewalls of the force measurement setup were modified to accommodate acrylic plates designed for each combination of gap and stagger. The airfoils were fixed to the plates upside down to minimize the shadows. (B) Two cameras were used to capture the required field of view. For two or three chords of stagger, the cameras were placed with one inch vertical offset, whereas they were placed level for smaller staggers. The blue dashed lines indicate the position where power spectral analysis was performed on the velocity data.

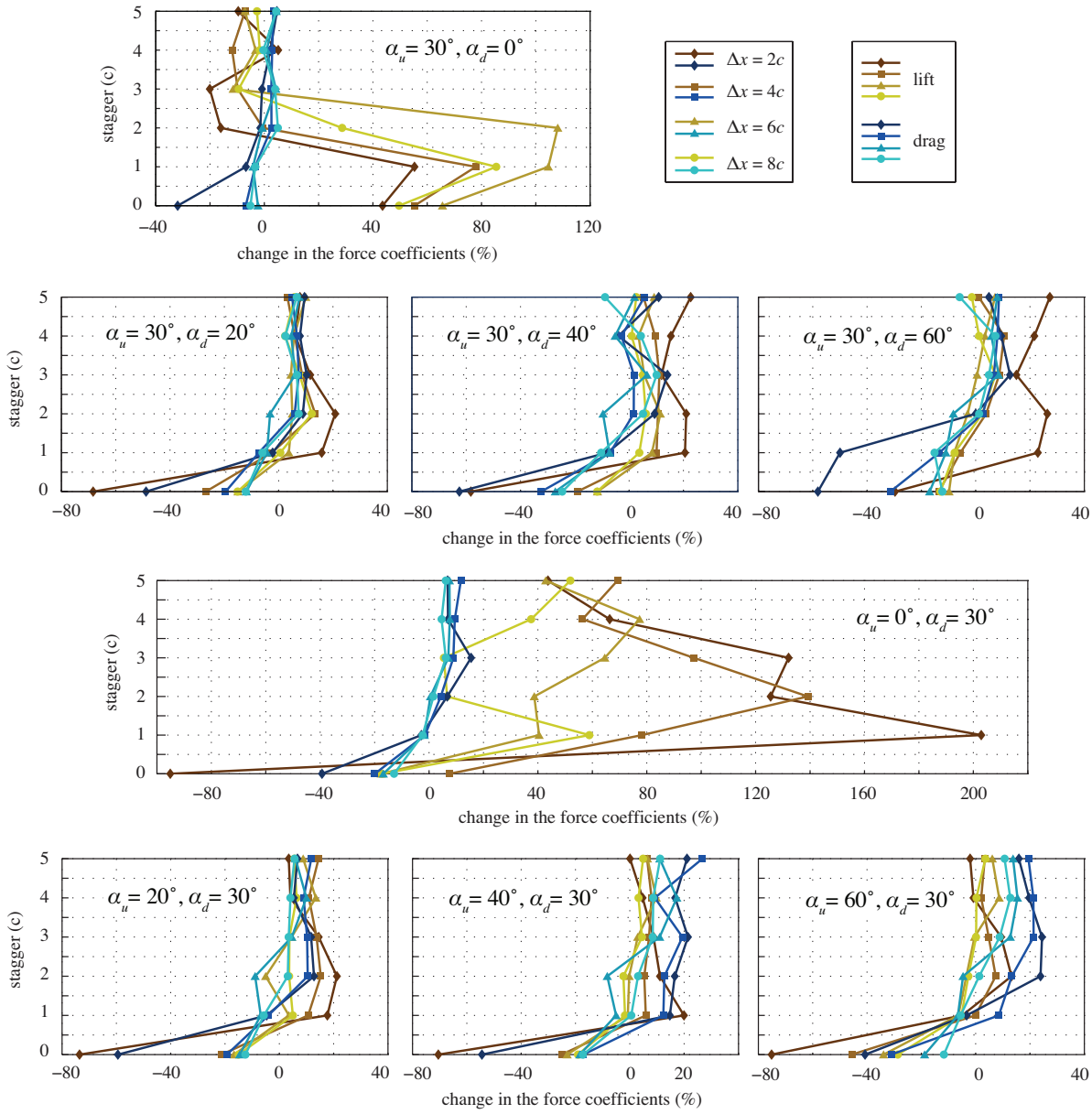

Fig. 4: The combined lift and drag produced by the tandem system. The curves show the percent change in the data compared to the results for single airfoils having the same angles of attack. The cases grouped in each panel have the same combination of angles of attack, and the curves depict the effects of gap and stagger within each group, revealing that stagger generally has a much stronger effect on the combined aerodynamic performance, and that lift is influenced by the tandem arrangement more noticeably than drag.

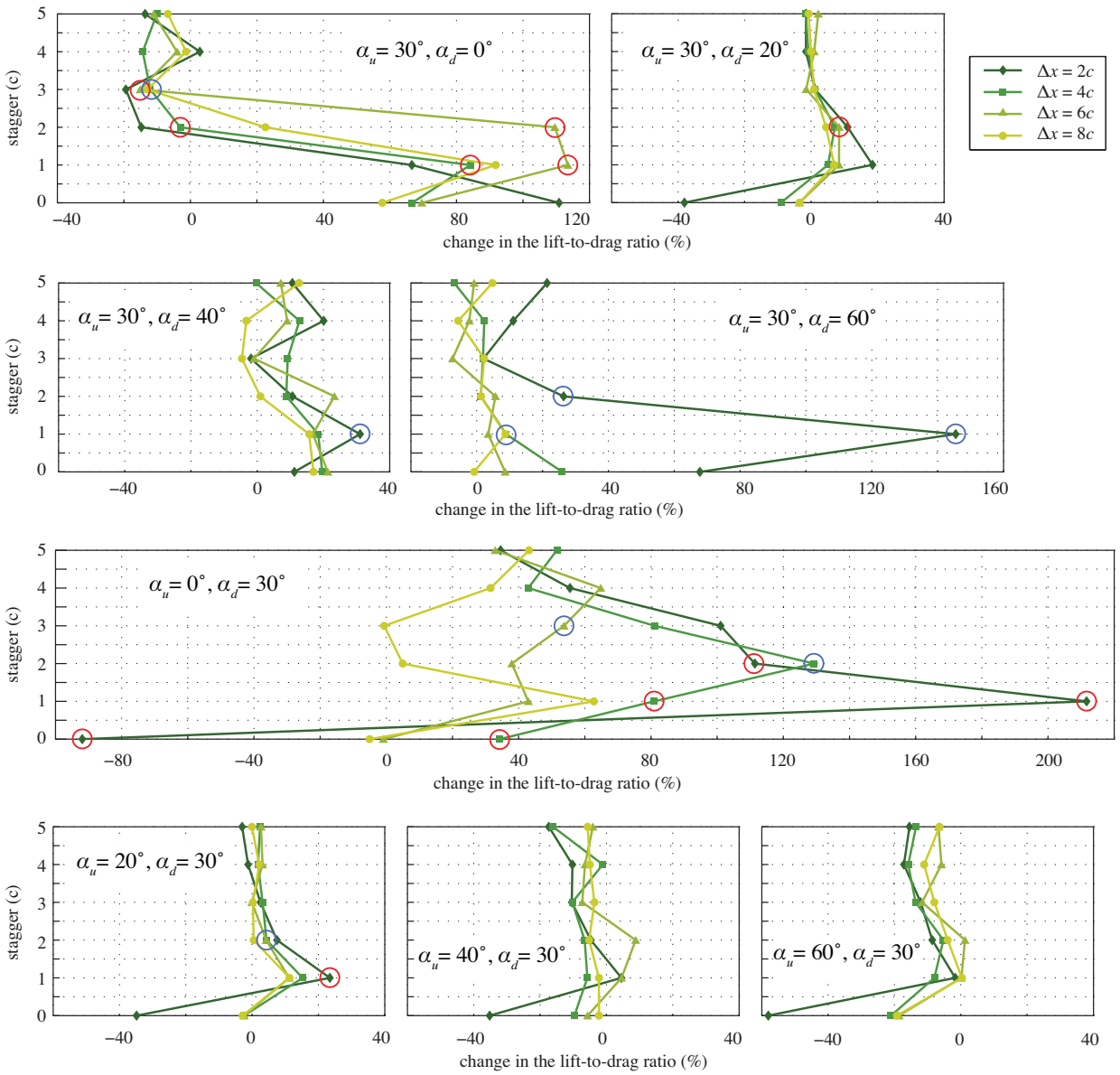

Fig. 5: The combined lift-to-drag ratio for the tandem system. The curves show the percent change in the data compared to the results for single airfoils having the same angles of attack. The cases grouped in each panel have the same combination of angles of attack. The cases with striking lift-to-drag augmentation along with their 'neighbors' that lack such effects were selected for the PIV experiments. The circled data specify the PIV cases. To minimize redundancy, the results were explored in greater detail only for the cases circled in red.

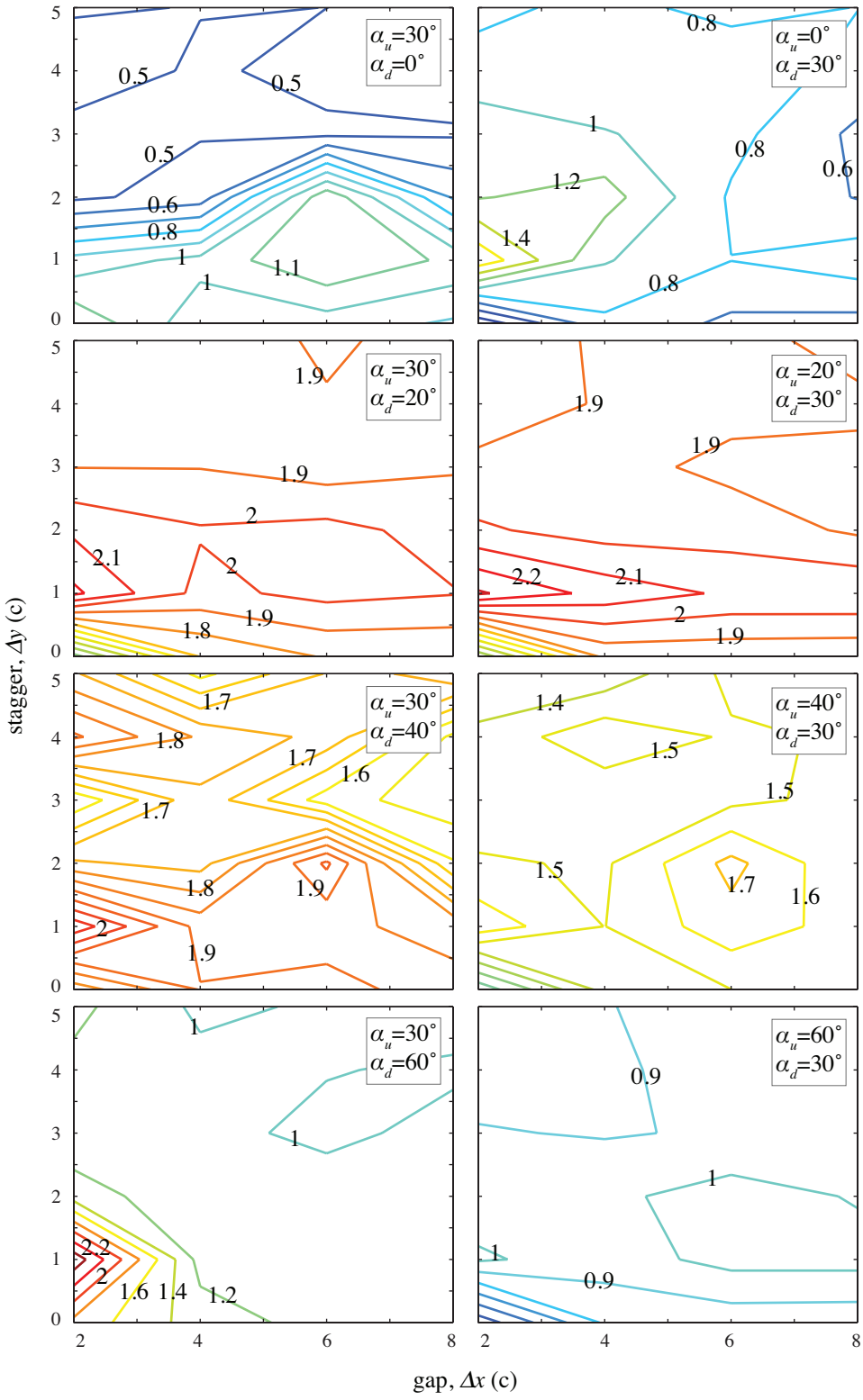

Fig. 6: Contour plots of the overall lift-to-drag ratio of the tandem airfoils in the Δx - Δy plane. Each panel shows the data for a combination of the angles of attack.

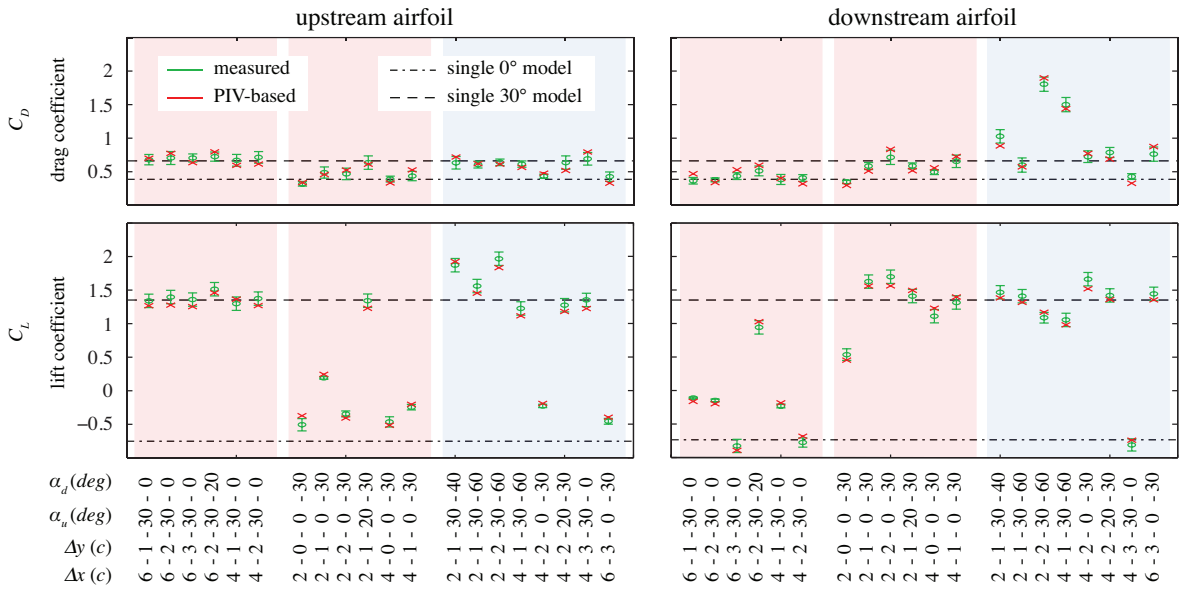

Fig. 7: Comparison between the load cell measurements and the PIV-based estimation of the lift and drag coefficients. The error bars indicate the uncertainty of the measured data. The data are categorized in three groups. The flow fields for the two groups specified by the red shade were explored in greater detail. The first red group includes the tandem configurations relevant to the kinematics of real snakes, and the second red group includes the cases with the most extreme tandem effects. The rest of the PIV cases are shaded blue.

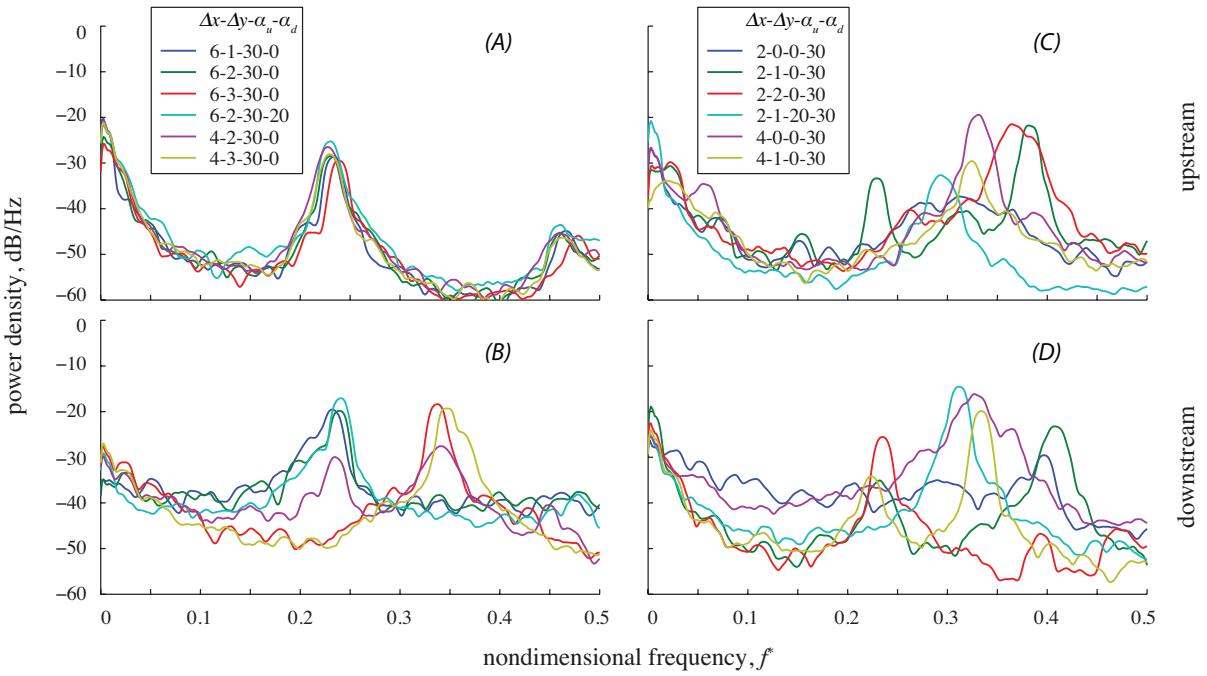

Fig. 8: Power spectral densities of the force measurements helps to understand the vortex shedding behavior of the two configuration groups of interest. (A) The upstream PSD of the group related to the snake kinematics is independent of the configuration. (B) The downstream peak frequency is locked at the upstream peak for some cases, but it is different for others. (C) The upstream PSD of the group experiencing the largest tandem effects is a function of tandem arrangement. (D) Both of the two peak frequencies of the case with the largest lift-to-drag enhancement ($\Delta x = 2c$, $\Delta y = 1c$, $\alpha_u = 0°$, $\alpha_d = 30°$) coincide, whereas other cases exhibit less coherence between the upstream and downstream PSDs.

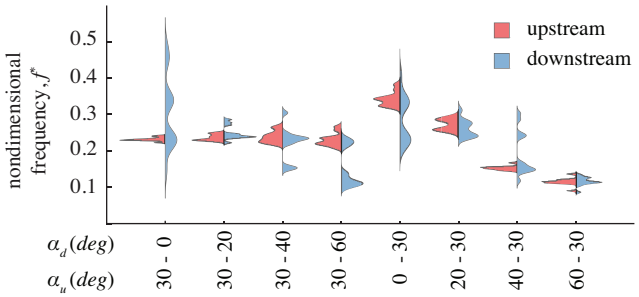

Fig. 9: Dependence of the PSD peaks on the tandem configuration. For each set of angles of attack, the probability density of the compilation of all peak frequencies of all combinations of gap and stagger was calculated and plotted separately for the upstream and downstream models. The results show that the tandem configuration could influence the spectra of the models by changing the dominant frequency, which is usually shared by both models, and by creating additional peaks for the downstream model.

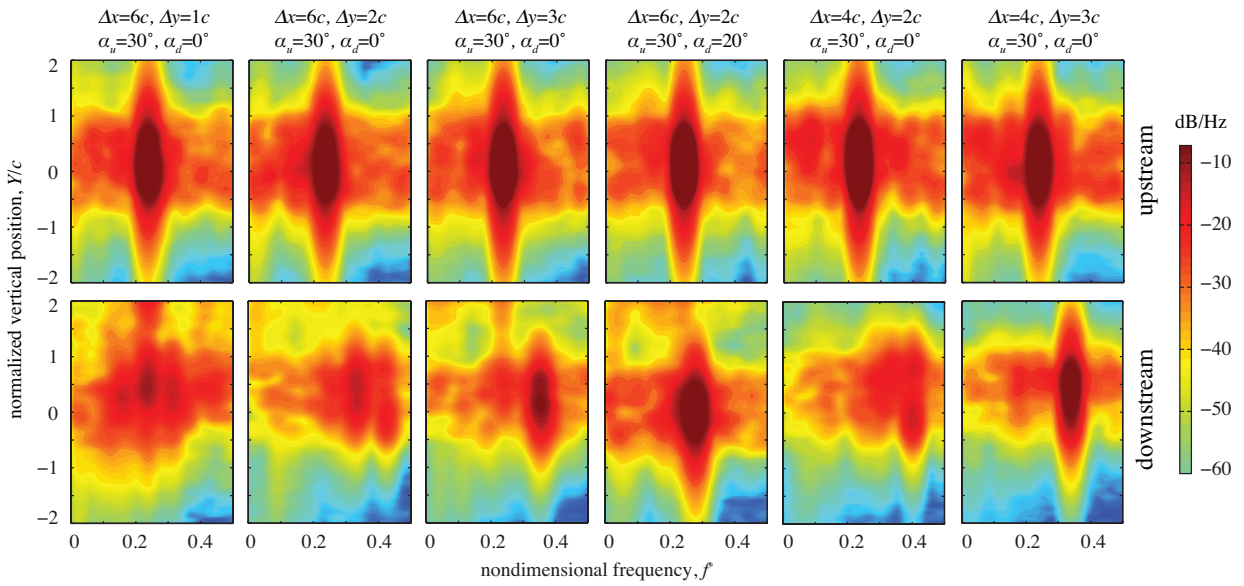

Fig. 10: Spatially resolved PSD of the vertical velocity component one chord downstream of each airfoil from the tandem configurations relevant to the flying snake kinematics. The upstream results with a single dominant frequency suggest a conventional bluff body wake. The downstream wakes are generally more turbulent and contain a broader spectrum of flow structures; however, the cases with the largest stagger ($\Delta y = 3c$) have structured wakes.

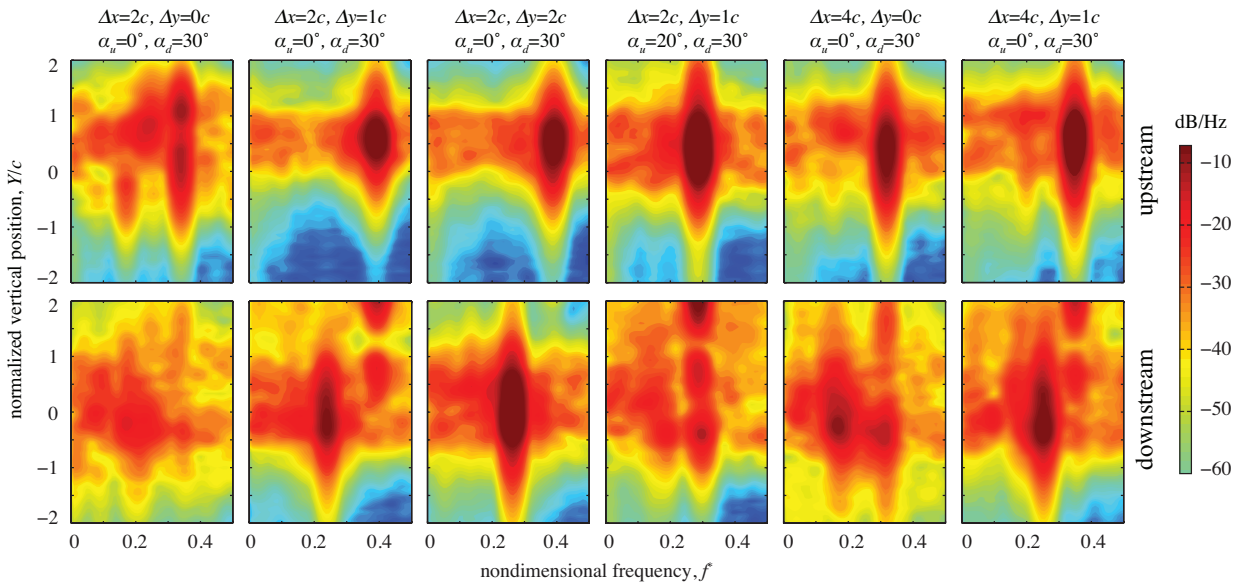

Fig. 11: Spatially resolved PSD of the vertical velocity component one chord downstream of each airfoil from the configurations experiencing the largest tandem effects. Except for $\Delta y = 0c$, the upstream wakes have a single dominant frequency, which varies with gap and stagger. The downstream wakes are generally more turbulent and power is spread through a large range of space and frequency domain.

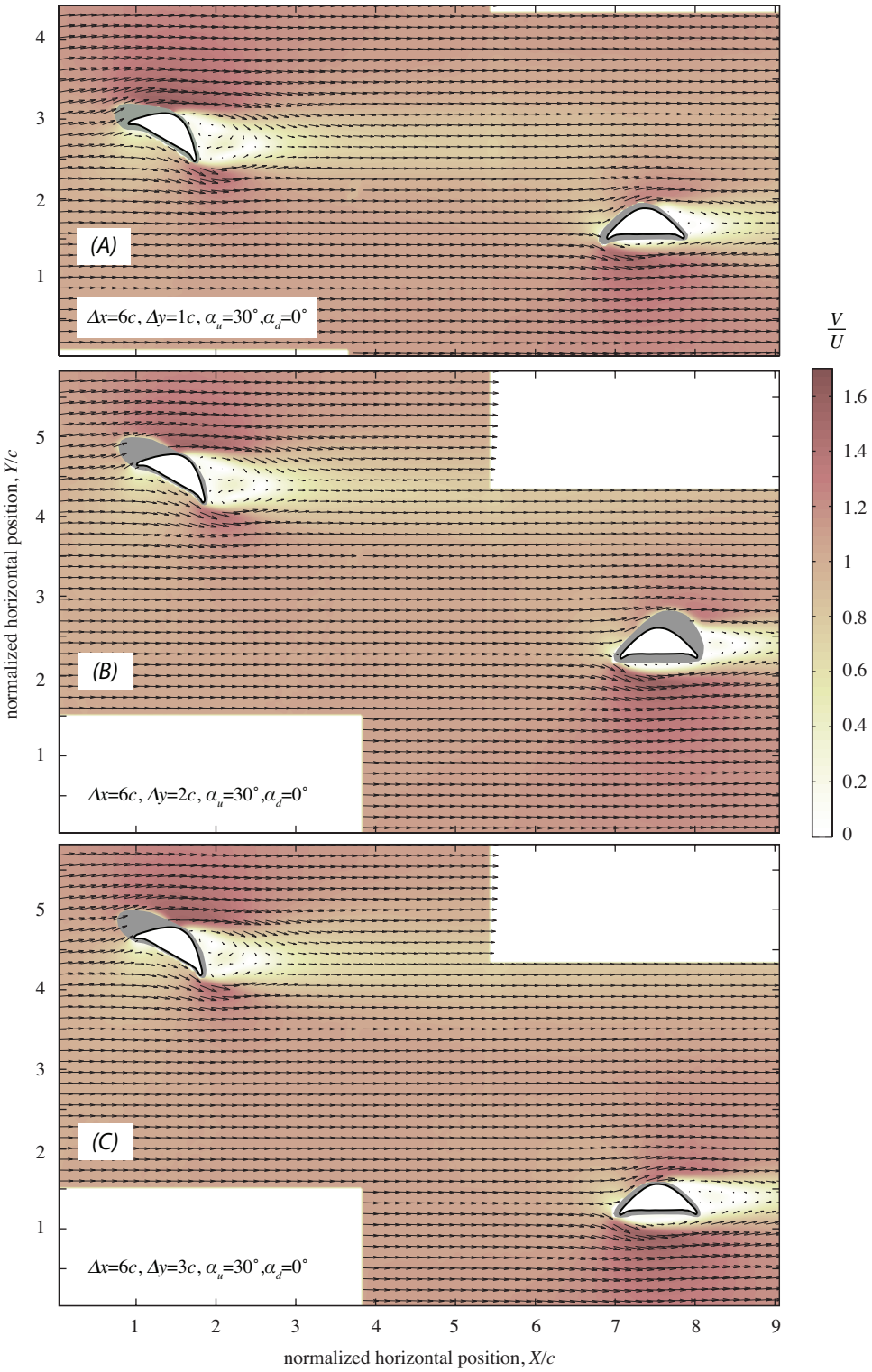

Fig. 12: The mean velocity field for three of the cases relevant to the kinematics of flying snakes. The background color indicates the normalized velocity magnitude, and the gray shades are the regions where the flow could not be resolved owing to shadows. The configurations are

the same except for the stagger. Unlike the upstream models, the flows around the downstream models are influence by the configuration.

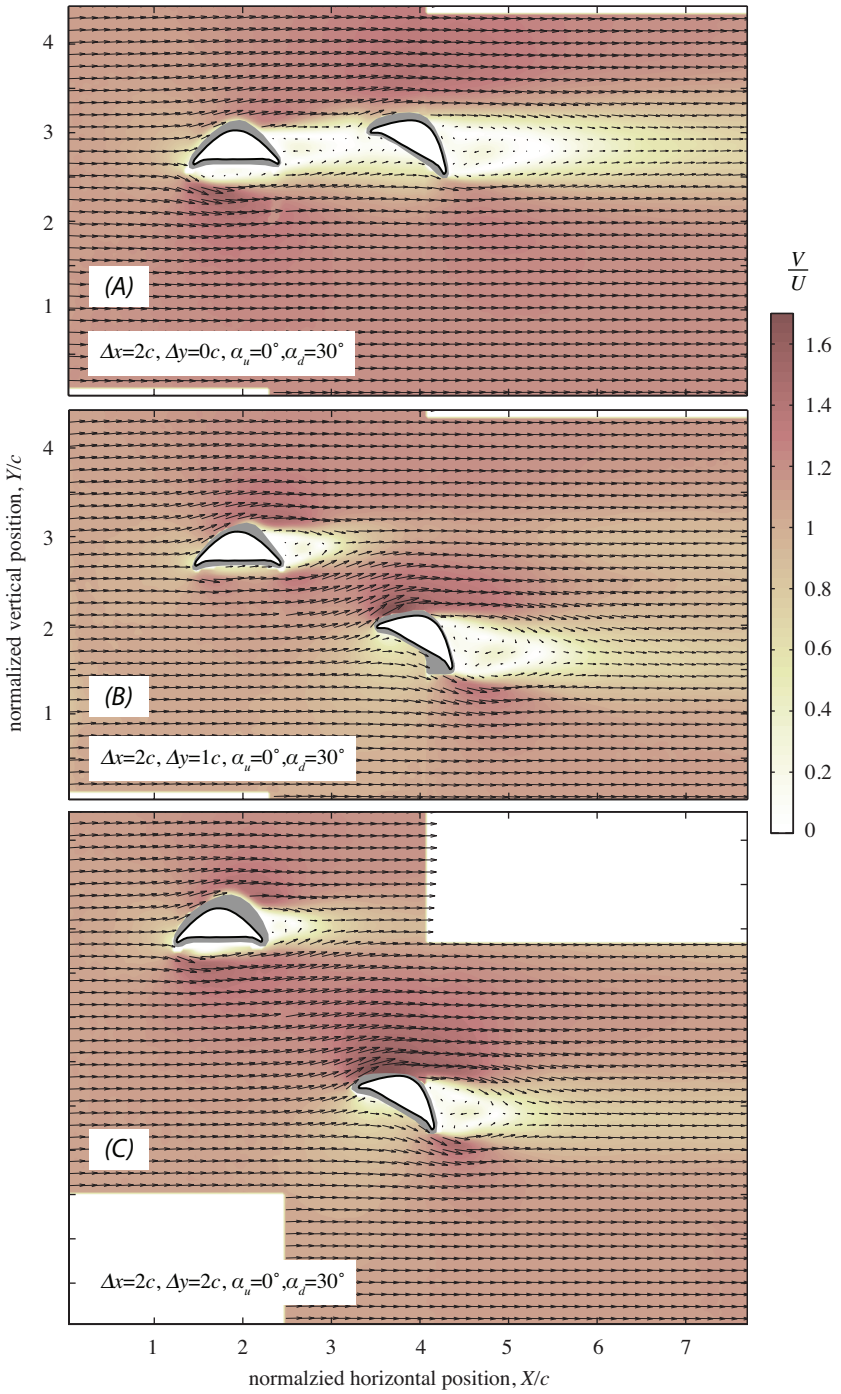

Fig. 13: The mean velocity field for three of the cases experiencing the largest tandem effects. The background color indicates the normalized velocity magnitude, and the gray shades are the regions where the flow could not be resolved owing to shadows. The configurations are the same except for the stagger. The flows around the upstream and downstream models are both influence by the configuration.

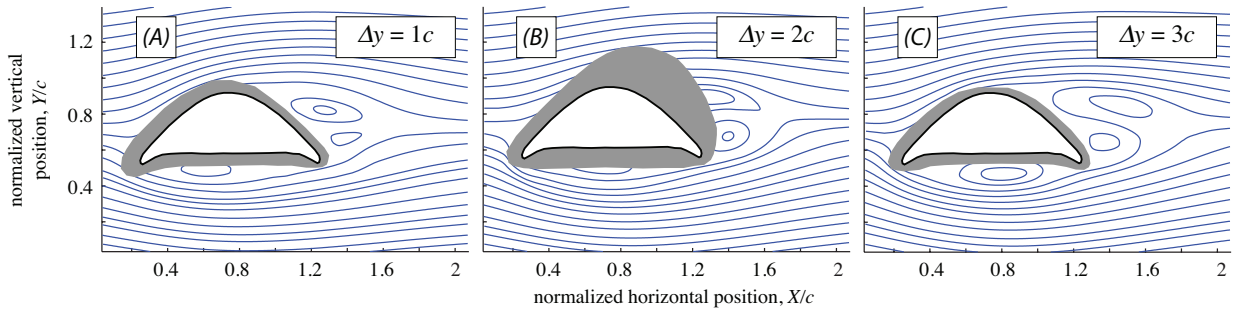

Fig. 14: The mean streamlines in the vicinity of the downstream models for three the cases relevant to the kinematics of flying snakes shown in Fig. 12. The configurations are the same ($\Delta x = 6c$, $\alpha_u = 30°$, $\alpha_d = 0°$) except for the stagger. The vortex trapped under the models is created when the flow on the ventral surface separates at the leading edge. The trapped vortex creates a downforce that results in negative lift. For the cases shown here, the strength of the vortex, and therefore the magnitude of the negative lift, varies with the stagger (See Table 2).

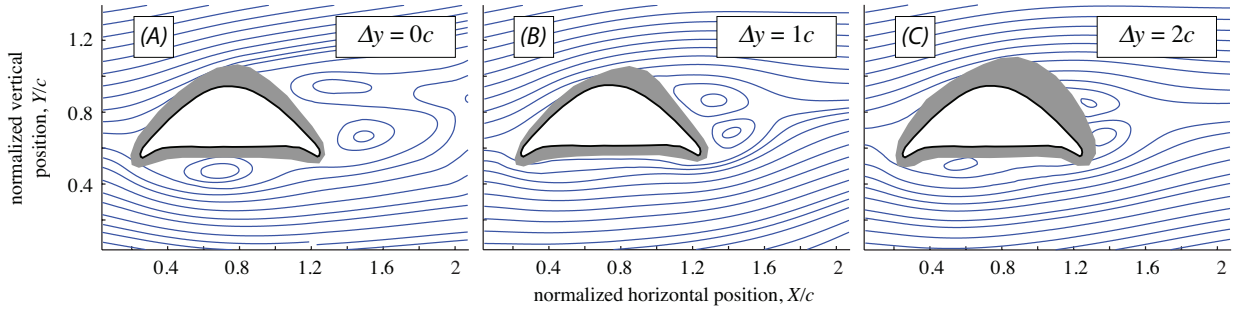

Fig. 15: The mean streamlines in the vicinity of the upstream models for the cases experiencing the largest tandem effects shown in Fig. 13. The configurations are the same ($\Delta x = 2c$, $\alpha_u = 0°$, $\alpha_d = 30°$) except for the stagger, which results in different flow structures. In particular, with one chord of stagger, the vortex that is normally trapped under the model vanishes and a positive lift is achieved (See Table 2).

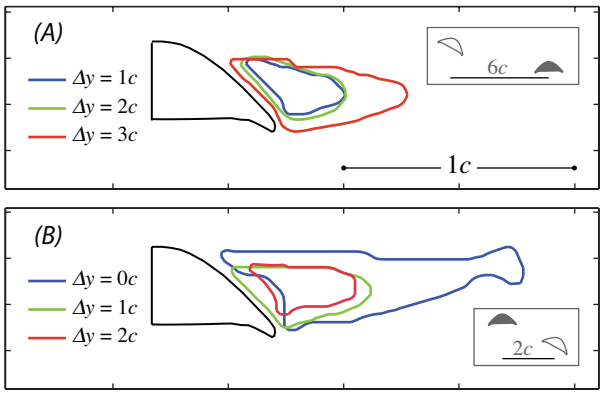

Fig. 16: The mean recirculation regions in the wake of (A) the downstream models of Fig. 14, and (B) the upstream models of Fig. 15. The recirculation region is where the streamwise velocity component and the freestream are in opposite directions.

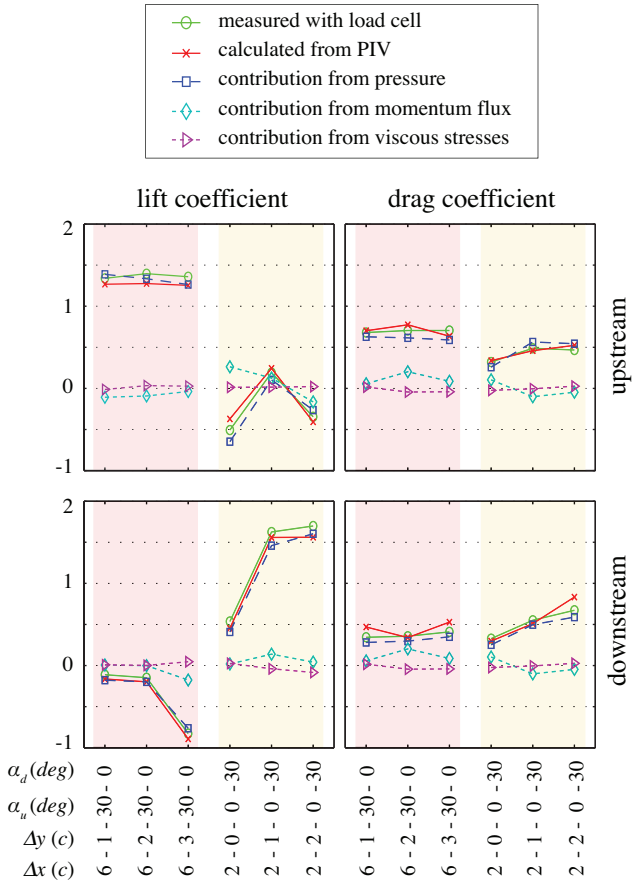

Fig. 17: The individual contributions of pressure, momentum flux, and viscous stresses to producing the lift and drag of the upstream and downstream airfoils for the cases summarized in Table 2. For these cases, viscous stresses made negligible contribution, whereas pressure accounted for the biggest contribution.

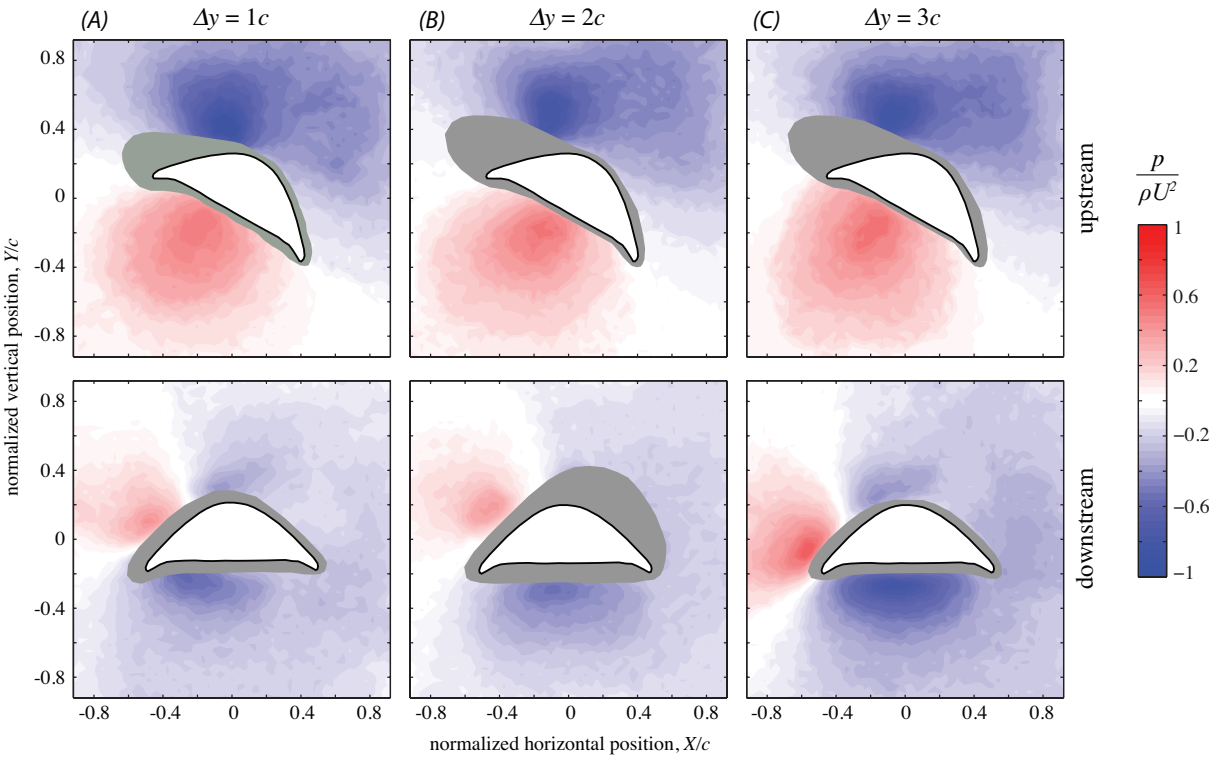

Fig. 18: The mean pressure fields in the vicinity of the models for the three cases relevant to the kinematics of flying snakes shown in Fig. 12. The configurations are the same ($\Delta x = 6c$, $\alpha_u = 30°$, $\alpha_d = 0°$) except for the stagger. Unlike the upstream pressure field, the downstream pressure field was influenced by the tandem arrangement. In particular, the size and strength of the low-pressure region at the ventral surface of the model significantly changed with the stagger.

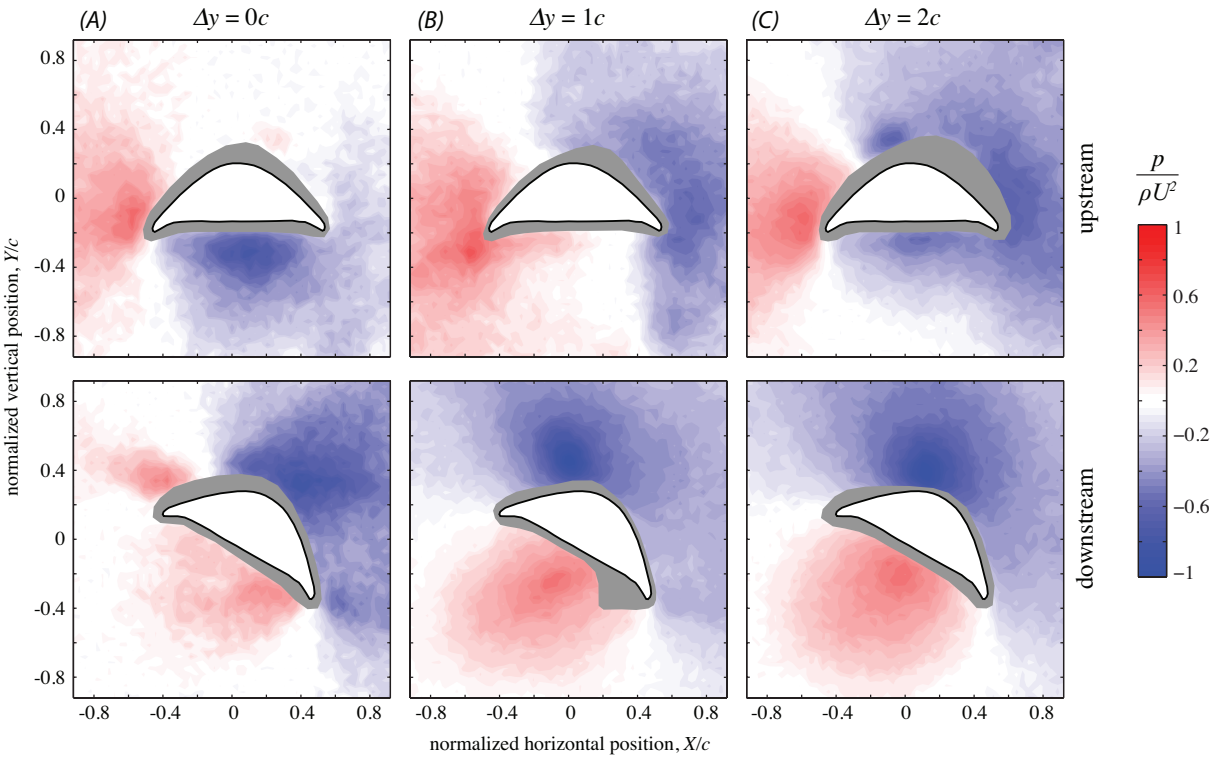

Fig. 19: The mean pressure fields in the vicinity of the models for the three cases experiencing the largest tandem effects shown in Fig. 13. The configurations are the same ($\Delta x = 2c$, $\alpha_u = 0°$, $\alpha_d = 30°$) except for the stagger. Both the upstream and downstream models were influenced by the tandem arrangement. In particular, at $\Delta y = 1c$, the typically low-pressure region at the ventral surface of the upstream model is partly replaced by a high-pressure zone, which results in a positive lift, unusual for a snake-like airfoil at 0° angle of attack.

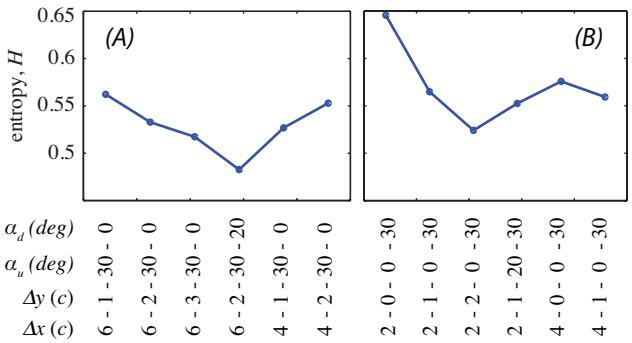

Fig. 20: The entropy associated with the POD, which indicates the level of flow organization, for (A) the cases relevant to the kinematics of flying snakes, and (B) the cases experiencing the largest tandem effects.

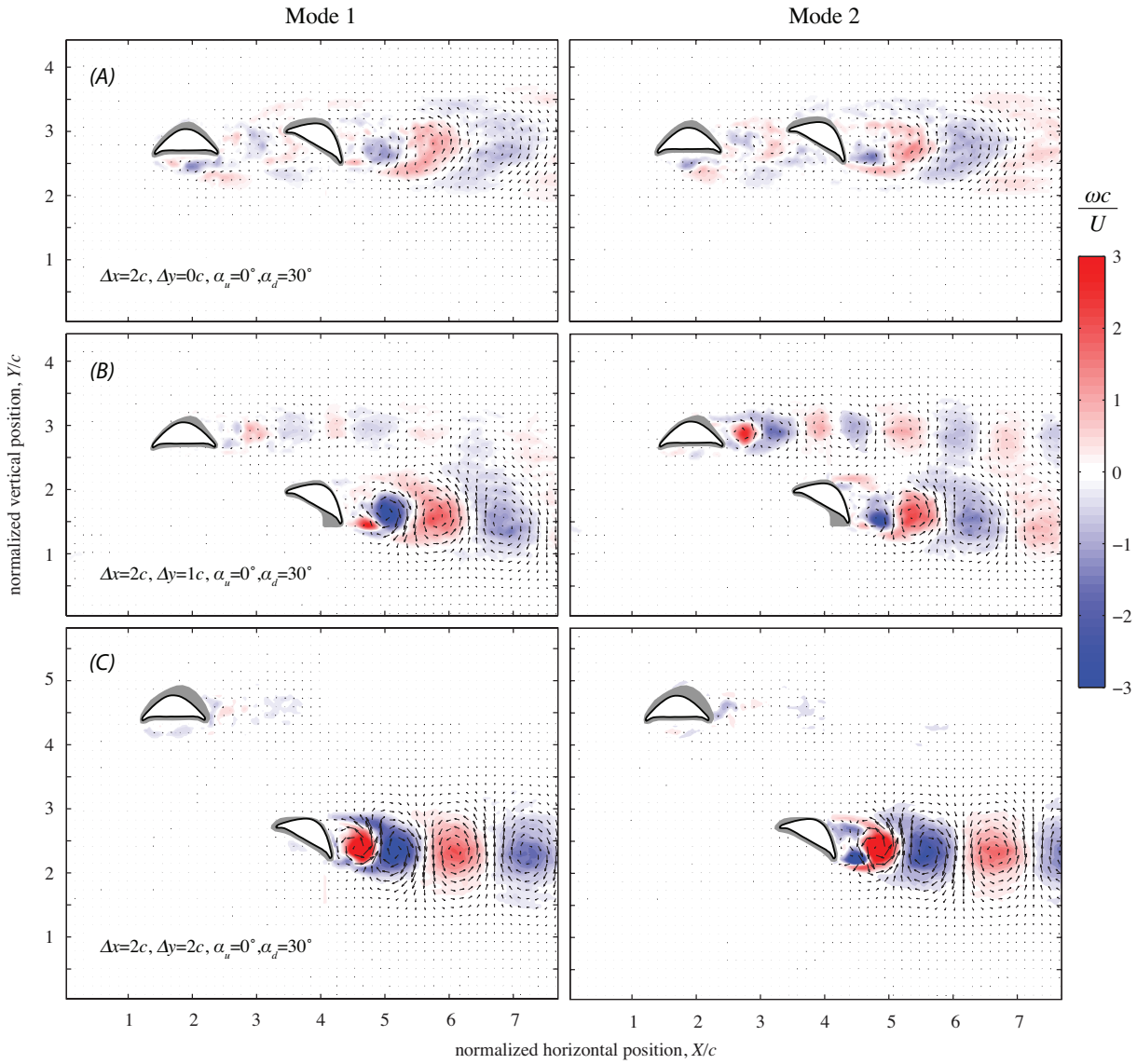

Fig. 21: The first two POD eigenmodes for three of the cases experiencing the largest tandem effects, illustrated by the velocity vectors and the nondimensional vorticity. These eigenmodes are representative of the dynamics of Kármán vortex streets.

References

AKHTAR, I., MITTAL, R., LAUDER, G. V. & DRUCKER, E. 2007. Hydrodynamics of a biologically inspired tandem flapping foil configuration. *Theoretical and Computational Fluid Dynamics,* 21**,** 155-170.

BAHLMAN, J. W., SWARTZ, S. M., RISKIN, D. K. & BREUER, K. S. 2013. Glide performance and aerodynamics of non-equilibrium glides in northern flying squirrels (*Glaucomys sabrinus*). *Journal of The Royal Society Interface,* 10**,** 20120794.

BALACHANDAR, S., MITTAL, R. & NAJJAR, F. 1997. Properties of the mean recirculation region in the wakes of two-dimensional bluff bodies. *Journal of Fluid Mechanics,* 351**,** 167-199.

BERKOOZ, G., HOLMES, P. & LUMLEY, J. L. 1993. The proper orthogonal decomposition in the analysis of turbulent flows. *Annual Review of Fluid Mechanics,* 25**,** 539-575.

BOMPHREY, R. J., LAWSON, N. J., TAYLOR, G. K. & THOMAS, A. L. 2006. Application of digital particle image velocimetry to insect aerodynamics: measurement of the leading-edge vortex and near wake of a Hawkmoth. *Experiments in Fluids,* 40**,** 546-554.

CHARONKO, J. J., KING, C. V., SMITH, B. L. & VLACHOS, P. P. 2010. Assessment of pressure field calculations from particle image velocimetry measurements. *Measurement Science and Technology,* 21**,** 105401.

DICKSON, W. B. & DICKINSON, M. H. 2004. The effect of advance ratio on the aerodynamics of revolving wings. *Journal of Experimental Biology,* 207**,** 4269-4281.

ECKSTEIN, A. & VLACHOS, P. P. 2009. Digital particle image velocimetry (DPIV) robust phase correlation. *Measurement Science and Technology,* 20**,** 055401.

EPPS, B. P. & TECHET, A. H. 2010. An error threshold criterion for singular value decomposition modes extracted from PIV data. *Experiments in Fluids,* 48**,** 355-367.

GIFFORD, A. R., DILLER, T. E. & VLACHOS, P. P. 2011. The physical mechanism of heat transfer augmentation in stagnating flows subject to freestream turbulence. *Journal of Heat Transfer,* 133**,** 021901.

HOLDEN, D. 2011. *Flying snakes: aerodynamics of body cross-sectional shape.* MSc thesis, Virginia Tech, VA, USA.

HOLDEN, D., SOCHA, J. J., CARDWELL, N. D. & VLACHOS, P. P. 2014. Aerodynamics of the flying snake *Chrysopelea paradisi*: how a bluff body cross-sectional shape contributes to gliding performance. *Journal of Experimental Biology,* 217**,** 382-394.

HUSAIN, Z., ABDULLAH, M. & YAP, T. 2005. Two-dimensional analysis of tandem/staggered airfoils using computational fluid dynamics. *International Journal of Mechanical Engineering Education,* 33**,** 195-207.

JAFARI, F., ROSS, S. D., VLACHOS, P. P. & SOCHA, J. J. 2014. A theoretical analysis of pitch stability during gliding in flying snakes. *Bioinspiration & Biomimetics,* 9**,** 025014.

KLEINHEERENBRINK, M., WARFVINGE, K. & HEDENSTRÖM, A. 2016. Wake analysis of aerodynamic components for the glide envelope of a jackdaw (*Corvus monedula*). *Journal of Experimental Biology,* 219**,** 1572-1581.

KRISHNAN, A., SOCHA, J. J., VLACHOS, P. P. & BARBA, L. 2014. Lift and wakes of flying snakes. *Physics of Fluids (1994-present),* 26**,** 031901.

LEHMANN, F.-O. 2008. When wings touch wakes: understanding locomotor force control by wake–wing interference in insect wings. *Journal of Experimental Biology,* 211**,** 224-233.

LEHMANN, F.-O. 2009. Wing–wake interaction reduces power consumption in insect tandem wings. *Experiments in Fluids,* 46**,** 765-775.

LENTINK, D. & DICKINSON, M. H. 2009. Rotational accelerations stabilize leading edge vortices on revolving fly wings. *Journal of Experimental Biology,* 212**,** 2705-2719.

MAYBURY, W. J. & LEHMANN, F.-O. 2004. The fluid dynamics of flight control by kinematic phase lag variation between two robotic insect wings. *Journal of Experimental Biology,* 207**,** 4707-4726.

MCGUIRE, J. A. 1998. *Phylogenetic systematics, scaling relationships, and the evolution of gliding performance in flying lizards (genus Draco)*. PhD thesis, University of Texas, Austin, TX, USA.

MICHELSEN, W. & MUELLER, T. Low Reynolds number airfoil performance subjected to wake interference from an upstream airfoil. AIAA Conference Paper, 1987. 87-2351.

MIKLASZ, K., LABARBERA, M., CHEN, X. & SOCHA, J. 2010. Effects of body cross-sectional shape on flying snake aerodynamics. *Experimental Mechanics,* 50**,** 1335-1348.

MUIJRES, F., JOHANSSON, L., BARFIELD, R., WOLF, M., SPEDDING, G. & HEDENSTRÖM, A. 2008. Leading-edge vortex improves lift in slow-flying bats. *Science,* 319**,** 1250-1253.

SANTA CRUZ, A., DAVID, L., PECHEUX, J. & TEXIER, A. 2005. Characterization by proper-orthogonal-decomposition of the passive controlled wake flow downstream of a half cylinder. *Experiments in Fluids,* 39**,** 730-742.

SCARANO, F. 2001. Iterative image deformation methods in PIV. *Measurement Science and Technology,* 13**,** R1.

SCHARPF, D. F. & MUELLER, T. J. 1992. Experimental study of a low Reynolds number tandem airfoil configuration. *Journal of Aircraft,* 29**,** 231-236.

SCHOLEY, K. 1986. The climbing and gliding locomotion of the giant red flying squirrel *Petaurista petaurista* (Sciuridae). *Biona Report,* 5**,** 187-204.

SCHRIJER, F. & SCARANO, F. 2008. Effect of predictor–corrector filtering on the stability and spatial resolution of iterative PIV interrogation. *Experiments in Fluids,* 45**,** 927-941.

SHYY, W., TRIZILA, P., KANG, C.-K. & AONO, H. 2009. Can tip vortices enhance lift of a flapping wing? *AIAA Journal,* 47**,** 289-293.

SMITH, T. R., MOEHLIS, J. & HOLMES, P. 2005. Low-dimensional modelling of turbulence using the proper orthogonal decomposition: a tutorial. *Nonlinear Dynamics,* 41**,** 275-307.

SOCHA, J. J. 2002. Kinematics: Gliding flight in the paradise tree snake. *Nature,* 418**,** 603-604.

SOCHA, J. J. 2011. Gliding flight in Chrysopelea: turning a snake into a wing. *Integrative and Comparative Biology,* 51**,** 969-982.

SOCHA, J. J., JAFARI, F., MUNK, Y. & BYRNES, G. 2015. How animals glide: from trajectory to morphology. *Canadian Journal of Zoology,* 93**,** 901-924.

SOCHA, J. J., MIKLASZ, K., JAFARI, F. & VLACHOS, P. P. 2010. Non-equilibrium trajectory dynamics and the kinematics of gliding in a flying snake. *Bioinspiration & Biomimetics,* 5**,** 045002.

SOCHA, J. J., O'DEMPSEY, T. & LABARBERA, M. 2005. A 3-D kinematic analysis of gliding in a flying snake, *Chrysopelea paradisi*. *Journal of Experimental Biology,* 208**,** 1817-1833.

SONG, J., LUO, H. & HEDRICK, T. L. 2014. Three-dimensional flow and lift characteristics of a hovering ruby-throated hummingbird. *Journal of The Royal Society Interface,* 11**,** 20140541.

USHERWOOD, J. R. & LEHMANN, F.-O. 2008. Phasing of dragonfly wings can improve aerodynamic efficiency by removing swirl. *Journal of The Royal Society Interface,* 5**,** 1303-1307.

VOGEL, S. 2003. *Comparative biomechanics: life's physical world*, Princeton University Press.

WANG, S., ZHANG, X., HE, G. & LIU, T. 2014. Lift enhancement by dynamically changing wingspan in forward flapping flight. *Physics of Fluids (1994-present),* 26**,** 061903.

WANG, Z. J. & RUSSELL, D. 2007. Effect of forewing and hindwing interactions on aerodynamic forces and power in hovering dragonfly flight. *Physical Review Letters,* 99**,** 148101.

WARKENTIN, J. & DELAURIER, J. 2007. Experimental aerodynamic study of tandem flapping membrane wings. *Journal of Aircraft,* 44**,** 1653-1661.

WEIMERSKIRCH, H., MARTIN, J., CLERQUIN, Y., ALEXANDRE, P. & JIRASKOVA, S. 2001. Energy saving in flight formation. *Nature,* 413**,** 697-698.

WESTERWEEL, J. & SCARANO, F. 2005. Universal outlier detection for PIV data. *Experiments in Fluids,* 39**,** 1096-1100.

Chapter 5. Conclusions

This work took the first steps toward a better understanding of how the snakes control their glide and maintain stability. In particular, the role of undulation and the S-shaped staggered posture were considered. Theoretical models were used to analyze the dynamics of flying snakes first in the longitudinal plane, and then in the three dimensions. The snake was modeled as a mechanical system with a number of airfoils. In the 2D approach, the airfoils were parallel to each other, and undulation was modeled by varying the length and mass of the airfoils. In the 3D analysis, the airfoils formed a chain, with undulation prescribed as a periodic input either for the joint torques or the joint angles. Despite their largely different structures, the two models led to similar deductions about the dynamics of snake flight, suggesting that (i) snake glide trajectories are passively unstable, and the snakes likely need a closed-loop control system to actively stabilize their trajectories, and (ii) in ideal conditions, passively stable trajectories relevant to the actual kinematics of snakes exist, and they provide an underlying stable framework around which a less demanding control system could be formed. The 3D model also verified the important role of undulation in expanding the basin of stability for the equilibrium gliding. Overall, the theoretical models of this study demonstrate the possibility of maintaining stability during gliding using a morphing body instead of symmetrically paired wings.

Physical models having the snake body's cross-sectional shape were tested in a water tunnel to study the aerodynamic interactions in a tandem arrangement. Such interactions are likely to be created by the staggered posture of snakes between the fore and the aft body. The results indicated that the tandem arrangement has significant effects on the aerodynamic forces on the upstream and downstream airfoils. Also, it was found that with specific arrangements, large changes in the aerodynamic performance could be produced with slight changes in the configuration. The aerodynamic performance is particularly sensitive to the stagger. It was therefore suggested that the snakes use the tandem effects, not necessarily as a means to produce more lift, but to control their glide trajectory by modifying the aerodynamics.

The above results contribute to many related fields. For instance, the chain model predicted a passively stable trajectory with undulation. This mode of locomotion, which was found here for the first time, can be used in many aerial and underwater bioinspired vehicles. Moreover, by determining the minimum set of requirements for a stable glide, an important

contribution was made to understanding the evolutionary path toward the gliding ability in snakes. This work has broader significance than merely its results. For the first time, purely theoretical approaches were used in this work to study the problem of stability analysis of gliding animals. The challenges and shortcomings of this approach had to be identified and overcome. This technique was proved to be effective, and it can likewise be employed in similar problems.

The approaches used in this study were subject to a number of limitations. Apart from the idealistic modeling of the snakes in 2D, the aerodynamic interactions among the airfoils and the 3D and unsteady effects were neglected in the theoretical works. In addition, the variation of mass, shape and size along the snake body was ignored, and no out-of-plane motion was allowed. The same idealizations existed in the experimental modeling approach too. Although each of these simplifications was argued to result in a relatively small error, the results of this work have to be validated with other theoretical or experimental work. An obvious next step would be using the tandem force coefficients in the theoretical models and study if that significantly changes the behavior of the model. If so, the results of the present work have to be considered with extra caution.

The outcome of this work was summarized in a number of hypotheses regarding the gliding behavior of flying snakes, which proposed that (i) the snakes required active control to remain stable, (ii) undulation contributes to stability, and (iii) staggered posture helps the snakes lower the control effort by increasing the sensitivity of aerodynamic forces to certain motions. Carefully designed experiments with real snakes to test these hypotheses seem extremely challenging, and robotic models seem to be a solution to conduct such experiments. Of course the range of applications of robotic models will go much further beyond testing the above hypotheses, and it seems that a deeper understanding of the physics of snake flight will need robotic replicas of the snakes in near future.

Appendices

A1. Derivation of the equations of motion for the two-dimensional model

A1.1. Equations of motion for Model 1

We recall that the momentum equation for a system with mass m, which changes with rate $\dot{m}$, is written as:

$$\frac{d}{dt}\left(m\mathbf{v}\right) = \mathbf{F} + \dot{m}\mathbf{u} \tag{A1}$$

where $\mathbf{F}$ is the net external force, $\mathbf{v}$ is the velocity of the system and $\mathbf{u}$ is the velocity of the mass flow entering it. In other words, the mass flow moving through the boundaries of the system acts like an external force on it and, therefore, we can derive the equations of motion for a variable mass system by substituting the *modified force*:

$$\mathbf{F}^{*} = \mathbf{F} + \dot{m}\mathbf{u} \tag{A2}$$

in the equations that we normally use for a system with constant mass.

If we define the linear momentum and the angular momentums about CoM as:

$$\mathbf{G} = \frac{d}{dt}\sum m_j \mathbf{v}_j \tag{A3}$$

$$\mathbf{H} = \sum\left(\mathbf{r}_j - \mathbf{r}_c\right) \times m_j \mathbf{v}_j \tag{A4}$$

where $\mathbf{r}_j$ is the position of mass m_j, and $\mathbf{r}_c$ is the position of CoM, we have:

$$\dot{\mathbf{G}} = \sum \mathbf{F}_j^{*} \tag{A5}$$

$$\dot{\mathbf{H}} = \sum\left(\mathbf{r}_j - \mathbf{r}_c\right) \times \mathbf{F}_j^{*} - \underline{\dot{\mathbf{r}}_c \times \mathbf{G}} \tag{A6}$$

It is helpful to mention that the underlined term in Eq. (A6) vanishes for a constant mass system, but we have to consider it here because of the variable mass.

The position of airfoils in Model 1 are readily given by:

$$\begin{cases} \mathbf{r}_1 = \left(x + d\cos\theta\right)\mathbf{i} + \left(z + d\sin\theta\right)\mathbf{j} \\ \mathbf{r}_2 = x\mathbf{i} + z\mathbf{j} \\ \mathbf{r}_3 = \left(x - d\cos\theta\right)\mathbf{i} + \left(z - d\sin\theta\right)\mathbf{j} \end{cases} \tag{A7}$$

The airfoil velocities could be found by differentiating Eq. (A7) with respect to time.

For the undulating mass (i.e., the mass moving among the airfoils), we assume that it passes the boundaries of each airfoil with *zero velocity relative to that airfoil*; hence, we let $\mathbf{u}_j = \mathbf{v}_j$.

Also, the position of CoM is calculated as:

$$\mathbf{r}_c = \frac{1}{m_{tot}} \sum m_j \mathbf{r}_j = \left(x + 2d \frac{\Delta m}{m_{tot}} \cos\theta \cos\omega t \right) \mathbf{i} + \left(z + 2d \frac{\Delta m}{m_{tot}} \sin\theta \cos\omega t \right) \mathbf{j} \tag{A8}$$

with airfoil masses defined in Eq. (1) of Chapter 2.

The equations of motion for Model 1 (Eqs. (2) and (3) of Chapter 2) can now be derived by substituting the above expressions in Eqs. (A5) and (A6).

A1.2. Equations of motion for Model 2

Here we relax the assumption of zero velocity of the undulating mass with respect to the airfoils; instead, we consider a uniform flow of mass along the middle link that transports mass between the airfoils (Fig. A1). This mass flow represents the undulation waves that pass along the flying snake's body. Clearly, the flow velocity should be proportional to the rate at which airfoils masses vary. Therefore, the flow velocity is given by:

$$u = u_w \sin\left(\omega t + \sigma\right) \tag{A9}$$

where u is the flow velocity, and u_w is the undulation wave speed. Using the data given in (Socha et al., 2005) we set $u_w = 0.28$ m/s.

We use Lagrange's equations to derive the equations of motion for Model 2. The set of generalized coordinates for this system was introduced in section 2.4 of Chapter 2, in terms of which the kinetic and potential energies are written as:

$$\begin{aligned} T = {} & \frac{1}{2} I_i \dot{\theta}^2 + \frac{1}{2} m_i \left[\left(\dot{x} - u\cos\theta \right)^2 + \left(\dot{z} - u\sin\theta \right)^2 \right] \\ & + \frac{1}{2} m_1 \left[\left(\dot{r}_1 + \dot{x}\cos\theta + \dot{z}\sin\theta \right)^2 + \left(r_1\dot{\theta} - \dot{x}\sin\theta + \dot{z}\cos\theta \right)^2 \right] \\ & + \frac{1}{2} m_2 \left[\left(\dot{r}_2 - \dot{x}\cos\theta - \dot{z}\sin\theta \right)^2 + \left(r_2\dot{\theta} + \dot{x}\sin\theta - \dot{z}\cos\theta \right)^2 \right] \end{aligned} \tag{A10}$$

$$V = m_i g z + m_1 g \left(z + r_1 \sin\theta \right) + m_2 g \left(z - r_2 \sin\theta \right) + \frac{1}{2} k \left(r_1 - l \right)^2 + \frac{1}{2} k \left(r_2 - l \right)^2 + \frac{1}{2} K_u \theta^2 \tag{A11}$$

Also, the dissipative energy function is:

$$R = \frac{1}{2} b\dot{r}_1^2 + \frac{1}{2} b\dot{r}_2^2 + \frac{1}{2} B_u \dot{\theta}^2 \tag{A12}$$

Finally, the virtual work of the aerodynamic forces plus the effect of variable mass of the airfoils (Pesce, 2003) through any virtual displacement is written as:

$$\begin{aligned}
\delta W = & \left[F_{l1} \sin\gamma_1 - F_{d1} \cos\gamma_1 + F_{l2} \sin\gamma_2 - F_{d2} \cos\gamma_2 \right] \delta x \\
& + \left[F_{l1} \cos\gamma_1 + F_{d1} \sin\gamma_1 + F_{l2} \cos\gamma_2 + F_{d2} \sin\gamma_2 \right] \delta z \\
& + \left[r_1 \left(F_{l1} \cos\beta_1 + F_{d1} \sin\beta_1 \right) - r_2 \left(F_{l2} \cos\beta_2 + F_{d2} \sin\beta_2 \right) \right] \delta\theta \\
& + \left[F_{l1} \sin\beta_1 - F_{d1} \cos\beta_1 + \dot{m} \left(\dot{x} \cos\theta + \dot{z} \sin\theta - u \right) \right] \delta r_1 \\
& + \left[-F_{l2} \sin\beta_2 + F_{d2} \cos\beta_2 + \dot{m} \left(\dot{x} \cos\theta + \dot{z} \sin\theta - u \right) \right] \delta r_2
\end{aligned} \tag{A13}$$

where $\dot{m} = -\Delta m \omega \sin\omega t$ is the time rate of change of airfoil masses, and u is calculated from Eq. (A9). The lift and drag forces are calculated based on the instantaneous velocities of the upstream and downstream airfoils and the corresponding lift and drag coefficients. Glide angle is obtained in terms of the generalized coordinates as:

$$\gamma_1 = -\tan^{-1} \left(\frac{\dot{z} + \dot{r}_1 \sin\theta + r_1 \dot{\theta} \cos\theta}{\dot{x} + \dot{r}_1 \cos\theta - r_1 \dot{\theta} \sin\theta} \right) \tag{A14a}$$

$$\gamma_2 = -\tan^{-1} \left(\frac{\dot{z} - \dot{r}_2 \sin\theta - r_2 \dot{\theta} \cos\theta}{\dot{x} - \dot{r}_2 \cos\theta + r_2 \dot{\theta} \sin\theta} \right) \tag{A14b}$$

Having found γ_j, the angle β_j is calculated as:

$$\beta_j = \theta + \gamma_j \,,\; j = 1,2 \tag{A15}$$

The equations of motion are derived upon inserting Eqs. (A10) through (A13) into the Lagrange's equations:

$$\frac{d}{dt} \frac{\partial T}{\partial \dot{x}_j} - \frac{\partial T}{\partial x_j} + \frac{\partial V}{\partial x_j} + \frac{\partial R}{\partial \dot{x}_j} = q_j \tag{A16}$$

with x_j and q_j being the generalized coordinates and forces, respectively. The consequent equations may be written in the matrix form of Eq. (10) of Chapter 2, where

$$\mathbf{M} = \begin{bmatrix} m_{tot} & 0 & -(m_1 r_1 - m_2 r_2)\sin\theta & m_1\cos\theta & -m_2\cos\theta \\ 0 & m_{tot} & (m_1 r_1 - m_2 r_2)\cos\theta & m_1\sin\theta & -m_2\sin\theta \\ -(m_1 r_1 - m_2 r_2)\sin\theta & (m_1 r_1 - m_2 r_2)\cos\theta & J_i + m_1 r_1^2 + m_2 r_2^2 & 0 & 0 \\ m_1\cos\theta & m_1\sin\theta & 0 & m_1 & 0 \\ -m_2\cos\theta & -m_2\sin\theta & 0 & 0 & m_2 \end{bmatrix} \tag{A17}$$

$$\mathbf{c} = \begin{bmatrix} -2(m_1\dot{r}_1 - m_2\dot{r}_2)\dot{\theta}\sin\theta - (m_1 r_1 - m_2 r_2)\dot{\theta}^2\cos\theta + m_i u\dot{\theta}\sin\theta \\ 2(m_1\dot{r}_1 - m_2\dot{r}_2)\dot{\theta}\cos\theta - (m_1 r_1 - m_2 r_2)\dot{\theta}^2\sin\theta - m_i u\dot{\theta}\cos\theta \\ 2(m_1 r_1\dot{r}_1 + m_2 r_2\dot{r}_2)\dot{\theta} - m_i u(\dot{x}\sin\theta - \dot{z}\cos\theta) + B_u\dot{\theta} \\ -m_1 r_1\dot{\theta}^2 + b\dot{r}_1 \\ -m_2 r_2\dot{\theta}^2 + b\dot{r}_2 \end{bmatrix} \tag{A18}$$

$$\mathbf{g} = \begin{bmatrix} 0 \\ m_{tot} g \\ (m_1 r_1 - m_2 r_2) g\cos\theta + K_u\theta \\ m_1 g\sin\theta + k(r_1 - l) \\ -m_2 g\sin\theta + k(r_2 - l) \end{bmatrix} \tag{A19}$$

$$\mathbf{q} = \begin{bmatrix} L_1\sin\gamma_1 - D_1\cos\gamma_1 + L_2\sin\gamma_2 - D_2\cos\gamma_2 \\ L_1\cos\gamma_1 + D_1\sin\gamma_1 + L_2\cos\gamma_2 + D_2\sin\gamma_2 \\ r_1(L_1\cos\beta_1 + D_1\sin\beta_1) - r_2(L_2\cos\beta_2 + D_2\sin\beta_2) \\ L_1\sin\beta_1 - D_1\cos\beta_1 \\ -(L_2\sin\beta_2 - D_2\cos\beta_2) \end{bmatrix} \tag{A20}$$

$$\mathbf{f} = \Delta m\omega \begin{bmatrix} (\dot{r}_1 + \dot{r}_2)\cos\theta - (r_1 + r_2)\dot{\theta}\sin\theta \\ (\dot{r}_1 + \dot{r}_2)\sin\theta + (r_1 + r_2)\dot{\theta}\cos\theta \\ (r_1 + r_2)\left[-\dot{x}\sin\theta + \dot{z}\cos\theta + (r_1 - r_2)\dot{\theta}\right] \\ \dot{r}_1 + u \\ -\dot{r}_2 + u \end{bmatrix} \tag{A21}$$

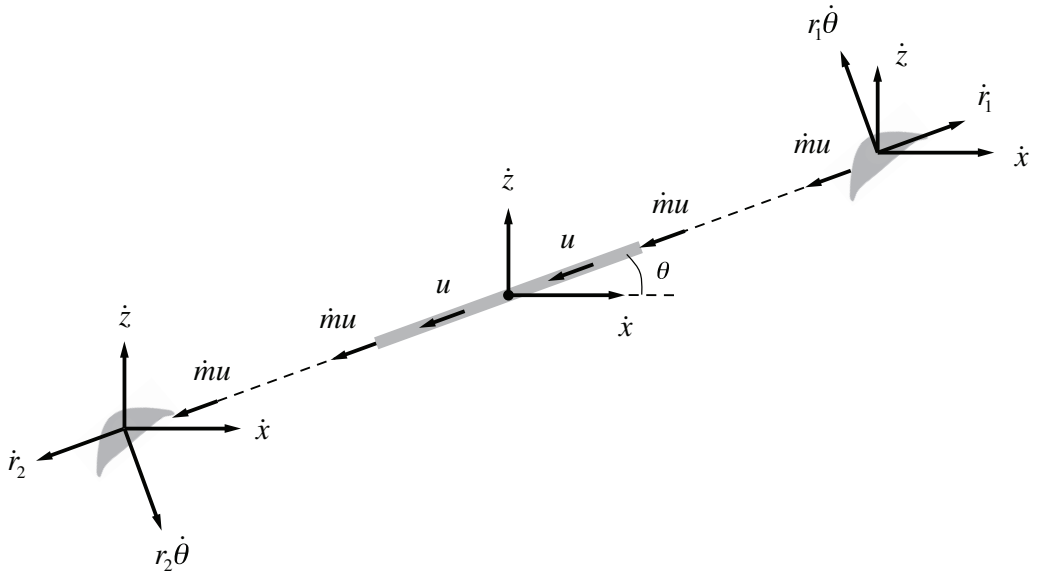

Fig. A1: The kinematics of Model 2 of Chapter 2 showing velocity components of the airfoils. The undulation of the body is considered as a smooth flow of mass along the middle link that transports mass between the airfoils. The velocity of the mass flow, which represents the undulating waves along the body, is proportional to the rate at which airfoils masses vary.

A2. Normalizing the periodic input amplitude based on the control effort

The head and tail points of the n-chain model of Chapter 3 are free, so the boundary conditions indicate that torque is always zero at those points. Because the n-chain model is an attempt to approximate the waveform of the real snake, it would be reasonable to assume a sinusoidal variation of torque along the body, which satisfies the mentioned boundary conditions (also see (Hirose and Yamada, 2009)). The appropriate form of torque is written as

$$\tau_j = \tau_0 \sin\left(2\pi \, {}^{j}\!/_{n}\right) \tag{A22}$$

where τ_i is the j^{th} joint torque, and τ_0 is some reference torque.

If we define the control effort as the RMS value of the joint torques, using Eq. (A22), it can be easily shown that

$$\tau_{rms} = \sqrt{\frac{1}{n}\sum_j \tau_j^2} = \frac{\sqrt{2}}{2}\tau_0 \tag{A23}$$

which is independent of the number of links.

Therefore, to be able to compare the simulation results properly, we normalized the amplitude of the periodic inputs for the models with different numbers of links, with respect to reference amplitude for each n that resulted in the same control effort.

References

HIROSE, S. & YAMADA, H. 2009. Snake-like robots [tutorial]. *Robotics & Automation Magazine, IEEE,* 16**,** 88-98.

PESCE, C. P. 2003. The application of Lagrange equations to mechanical systems with mass explicitly dependent on position. *Journal of Applied Mechanics*, 70, 751–756.

SOCHA, J. J., O'DEMPSEY, T. & LABARBERA, M. 2005. A 3-D kinematic analysis of gliding in a flying snake, *Chrysopelea paradisi*. *Journal of Experimental Bioliogy,* 208, 1817–33.